University of Kerbala
College of Science
Department of Physics

Preparation and Characterization of Titanium Dioxide Doped with Gold Nanoparticles as Photocatalysts

A Thesis
Submitted to the College of Science of the University of Kerbala in Partial Fulfillment of the Requirements for the Degree of Master of Science in Physics

By

Rasha Jameel Neama

B.Sc. 2009

Supervised by

Prof. Dr. Khawla J. Tahir   **Prof. Dr. Firas K. Mohamad Alosfur**

April/ 2024 A.D   **Ramadan/ 1445 A.H**

Supervisor Certification

I certify that the preparation of this thesis entitled "**Preparation and Characterization of Titanium Dioxide Doped with Gold Nanoparticles as Photocatalysts**" was made under my supervision by "**Rasha Jameel Neama**" at the Department of Physics, College of Science, University of Kerbala, as a partial fulfillment of the requirements for the degree of Master in Physics Science.

Signature:

Name: **Dr. Khawla J. Tahir**

Title: **Professor**

Address: **Department of Physics, College of Science, University of Kerbala**

Date: 2/ 4/ 2024

Signature:

Name: **Dr. Firas K. Mohamad Alosfur**

Title: **Professor**

Address: **Department of Physics, College of Science, University of Kerbala**

Date: **2 / 4/ 2024**

Certification of the Head of the Department

Given the available recommendations, I forward this thesis for debate by the examining committee.

Signature: M. A. AL-KAAB

Name: **Dr. Mohammed Abdulhussain AL-Kaabi**

Title: **Assistant Professor**

Address: **Head of Physics Department, College of Science, University of Kerbala**

Date: 14 / 4/ 2024

Date: /   / 2024

Examination Committee Certification

We certify that we have read this thesis, entitled "**Preparation and Characterization of Titanium Dioxide Doped with Gold Nanoparticles as Photocatalysts**" and as an examining committee, examined the student "**Rasha Jameel Neama**" on its contents and that in our opinion it is adequate for the partial fulfillment of the requirements for the degree for the degree of Master of Science in Physics.
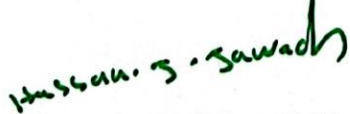
Signature: A. M. Abdu

Name: **Dr. Ahmed M. Abdul-Lettif**
Title: Professor
Address: University of Kerbala, College of Science, Department of Physics.
Date: 2 / 4 / 2024
(Chairman)

Signature R.A

Name: **Dr. Radhyah Mahdi Al-Jarrah**
Title: Professor
Address: University of Kufa, College of Science, Department of Physics.
Date: 2/ 9 / 2024
(Member)

Signature

Name: **Dr. Ammar S. Hameed**
Title: Assist. Professor
Address: University of Kerbala, College of Science, Department of Physics.
Date: 2/ 4 / 2024
(Member)

Signature: KH

Name: **Dr. Khawla J. Tahir**
Title: Professor
Address: University of Kerbala, College of Science, Department of Physics.
Date: 2/ 4/ 2024
(Member & Supervisor)

Signature:

Name: **Dr. Firas K. Mohamad Alosfur**
Title: Professor
Address: University of Kerbala, College of Science, Department of Physics.
Date: 2/ 4 / 2024
(Member & Supervisor)

Signature: Hassau. J. Jawad

Name: **Dr. Hassan Jameel Jawad AL-Fatlawy**
Title: Professor
Address: **Dean of the College of Science, University of Kerbala.**
Date: /   / 2024

بِسْمِ اللهِ الرَّحْمَنِ الرَّحِيمِ

اللهُ نُورُ السَّمَاوَاتِ وَالْأَرْضِ مَثَلُ نُورِهِ كَمِشْكَاةٍ فِيهَا مِصْبَاحٌ الْمِصْبَاحُ فِي زُجَاجَةٍ الزُّجَاجَةُ كَأَنَّهَا كَوْكَبٌ دُرِّيٌّ يُوقَدُ مِنْ شَجَرَةٍ مُبَارَكَةٍ زَيْتُونَةٍ لَا شَرْقِيَّةٍ وَلَا غَرْبِيَّةٍ يَكَادُ زَيْتُهَا يُضِيءُ وَلَوْ لَمْ تَمْسَسْهُ نَارٌ نُورٌ عَلَى نُورٍ يَهْدِي اللهُ لِنُورِهِ مَنْ يَشَاءُ وَيَضْرِبُ اللهُ الْأَمْثَالَ لِلنَّاسِ وَاللهُ بِكُلِّ شَيْءٍ عَلِيمٌ ۢ٢٥

صدق الله العلي العظيم

سورة النور الاية (35)

Dedication

To...

My family (mother, father, husband Lateef, my daughter Saja, my sons Hussain and Zain Al-Abdeen) for their support and motivation to pursue my dreams.

All who stood by my side and supported me.

I dedicated this work with love and gratefulness.

Rasha Jameel Neama

2024

Acknowledgments

Abstract

In this work, titanium dioxide (TiO_2) and X% Au/TiO_2 with different percentages (0.5, 1.0, 1.5, 2.0, and 2.5) were prepared by the sol-gel method and annealed at 450 °C.

The crystal structure, the ratio of rutile phase and anatase, and the crystallite size of the prepared nanoparticles were determined using XRD analysis. XPS analysis was used to determine the elemental composition and percentage in the samples accurately. The morphology of the samples was identified through TEM and FESEM analysis. EDX analysis confirmed the presence of Au NPs in the doped samples and revealed the percentage composition of other elements. Mapping analysis showed a uniform distribution of nanoparticles within all samples. Specific surface area and porosity were evaluated using Brunauer-Emmett-Teller (BET) analysis. UV-Vis and FTIR analytical methods investigated optical absorbance in the ultraviolet and infrared regions, respectively.

The optimal dosage of catalysts in the photocatalytic degradation process was determined. Different quantities of TiO_2 catalysts (05, 10, 15, 20, and 25 mg) were tested, using an initial concentration of 10 ppm of Methylene blue. The degradation efficiency was evaluated under UV light irradiation, ultimately selecting 15 mg as the most effective catalytic dose, resulting in a percentage degradation efficiency of 68.62%. Subsequently, the degradation of MB was assessed for various catalysts, including 0.5% Au/TiO_2, 1% Au/TiO_2, 1.5% Au/TiO_2, 2% Au/TiO_2, and 2.5% Au/TiO_2. Under identical conditions (initial concentration of MB = 10 ppm, catalyst dose = 15 mg, and 120 min UV light irradiation). The 2% Au/TiO_2 catalyst demonstrated the highest degradation percentage of MB, measuring 79.88%.

Contents

Chapter 1   Introduction

Chapter 2   Fundamental Concepts and Literature Review

Chapter 3   Methodology

List of Tables

List of Figures

List of Abbreviations

Abbreviation	Def.
a.u	Arbitrary Unit
BET	Brunauer-Emmett-Teller
BJH	Barrett-Joyner-Halenda
CB	Conduction Band
CVD	Chemical Vapor Deposition
C_2H_5OH	Ethanol
DIW	Deionized Water
EDX	Energy Dispersive of X-Ray Spectroscopy
FESEM	Field Emission Scanning Electron Microscopy
FTIR	Fourier Transform Infrared Spectroscopy
FWHM	Full-Width at Half Maximum
LO	lattice oxygen
MB	Methylene Blue
mL	Milliliter
μm	Micrometer (10^{-6} m)
nm	Nanometer (10^{-9} m)
NPs	Nanoparticles
PDE	Photo Degradation Efficiency
PH	The Acidity of an Aqueous Solution
PVD	Physical Vapor Deposition
P25 TiO_2	Titanium Dioxide with Particle Size around 25 nm
ppm	Parts per Million
rpm	Rotation Rounds per Minute
SEM	Scanning Electron Microscopy
SPR	Surface Plasmon Resonance
SO	surface-adsorbed oxygenated species
TEM	Transmission Electron Microscope
TTIP	Titanium (IV) Isopropoxide or Tetra-Isopropoxide
UV	Ultraviolet
VB	Valence Band
Vis	Visible Light
XPS	X-ray Photoelectron Spectroscopy
XRD	X-ray Diffraction

List of Symbols

Symbols	Def.
a, b, c	Lattice Constants
A	Absorption
Å	Angstrom (10^{-10} m)
A_o	Initial Absorbance
A_t	Absorbance after Some Time
C_o	Initial Concentration (mg/L or ppm)
C_t	Concentration after Some Time (mg/L or ppm)
$^\circ C$	Degree Celsius
d	Inter Planer Space
D	Average Crystal Size
D%	Degradation Rate
e^-	Electron
Eg	The Energy Band Gap (eV)
g	Gram
h^+	Hole
$\square$	Planck's Constant
h	Hour
hkl	Crystal Plane Indices
$\square v$	Incident Photon Energy
$HO_2^{\bullet}$	Hydroperoxyl Radical
K	Kelvin
k	Pseudo-First-order Kinetics Constant
n	Reflection order
N_2	Nitrogen
OH^-	Hydroxide Ion
$^{\bullet}OH$	Hydroxyl Radical
O_2	Oxygen
$O_2^{\bullet -}$	Superoxide Radical
P	Pressure
P/P_o	Relative Pressure
T	Temperature ($^\circ C$ or K)
t	Time (s or min)
W	Watt

θ	Bragg Angle (degree)
λ	Wavelength of Light
ν	Frequency of Photon
β	Full-Width at Half Maximum in Radian

Chapter 1
Introduction

1.1 Introduction

Industrial improvements have increased the pace of water use during the last several decades. Due to a scarcity of clean water resources, water recycling through the removal of highly colored wastewater has become critical. Organic components on the one hand, such as phenols generate an unpleasant taste and odor in water and can also hurt natural biological processes. Organic pollutants such as methylene blue (MB), benzene, carbon tetrachloride, vinyl chloride, and trichloroethylene, on the other hand, might pose health risks in significant concentrations. If dirty water to be used for human consumption in the house, these toxins must be eliminated [1]. Different methods in this field, such as oxidation, adsorption, anaerobic, and reduction treatments, have been developed for the elimination of contaminated dyes from the effluents. Unfortunately, these processes have many disadvantages, such as expensive operating conditions, the creation of sludge, and inefficiency in situations where complex aromatic compounds are produced [2]

Therefore, scientists and researchers are trying to discover and develop new methods for the water treatment of organic compounds, such as dyes, via photocatalytic procedure using a semiconductor degradation process. This process is cheaper, simpler, and cleaner. Hence, the process of photocatalytic is confessed as being a "greener" technology for toxic inorganic and organic pollutants elimination from wastewater at normal pressure and ambient temperature. The main feature of the photocatalytic process is that it breaks complex organic molecules into simple molecules such as carbon dioxide and water, this process has been used for a variety of applications such as the decomposition of organic pollutants [3,4]. Photocatalysis based on titanium dioxide (TiO_2) nanoparticles (NPs) as a perpetual photocatalyst has received much attention in water purification technologies during the past years, due to its wide band energy, low cost, stable material, high activity, and nontoxic [5].

TiO$_2$ applicability is restricted due to its poor photoactivity under visible light. As a result, attempts have been made to expand its photoactivity to the visible range by substituting Ti^{4+} on the crystalline structure by metallic ions such as Fe, Ni, Co, Ag, Au, Pt, and so on [6–13].

Modification of the photocatalyst's electronic structure is required to design and create TiO$_2$-based photocatalysts that can work under visible-light irradiation. To control the electronic structure of TiO$_2$, two approaches are being considered: (1) modification of the electronic structure of TiO$_2$ via metal doping and (2) formation of a new valence band via nonmetal doping or the formation of new binary oxides [14].

Many researchers have reported the preparation of TiO$_2$ NPs using several ways such as sol-gel, hydrothermal, microwave-assisted methods, etc. However, most of these preparation processes require multiple steps, long synthesis times, and expensive thermal equipment. Thus, there is a request to find a faster and easier method for preparation [15].

In recent years, the sol-gel preparation process has been widely employed in the production of catalysts such as TiO$_2$ nanopowders. The sol-gel process, in general, includes the transformation of a system from a liquid sol to a solid gel phase. Precursors are often organometallic compounds that result in materials with varying physicochemical characteristics [16]. It has several advantages over traditional approaches. In supported metals catalysis, for example, the active metal and support can be produced in a single process. This enables cost savings in catalyst preparation [17].

1.2   Problem Statement

One of the main classes of organic chemicals that pose an increasing environmental risk is textile dyes and other industrial dyestuffs. As a result, the degradation of dyes in industrial wastewater has drawn more attention, and various remediation strategies have been suggested. Unfortunately, with the growth of the dyeing industry, synthetic textile dyes have taken over as the primary dying substance. Because of the chemical stability of synthetic dye effluent, conventional wastewater treatment methods are notably ineffective [18]. The removal of dyes from wastewater using photocatalysis has been the subject of numerous investigations that have been published in the literature [19, 20]. The majority of researchers in these studies have only been interested in the photocatalytic degradation of the model dyes, which has limited the usefulness of the provided data in practical situations. Each study used a different set of operation conditions and photocatalysts, therefore a systematic investigation that concentrated on dyes with industrial applications would be very significant and pertinent to the subject.

Despite the benefits of the TiO_2 photocatalytic system modification techniques, their applicability in actual wastewater technology is currently limited and required development. This is due to TiO_2's poor absorption profile and high excitation recombination rate, two of its many flaws. Numerous literary attempts have been made to address these issues. Sol-gel is one of the simplest ways to produce TiO_2 and ultimately enhance TiO_2 photocatalytic activity because used low-temperature processing. According to the literature, noble metal cluster impregnation or deposition on TiO_2 can increase the photocatalytic activity of the material by changing the band gap. Due to their surface plasmon resonance effects, gold nanoparticles in particular have been found to exhibit remarkable visible-light absorption. Therefore, it is crucial to

create TiO$_2$ that has enhanced photocatalytic activity compared to what is already available.

1.3   Thesis Objectives

As previously stated, significant research efforts are being made to produce effective photocatalysts for the breakdown of MB dye in water. The purpose of this thesis is to fabricate and optimize X% Au/TiO$_2$ photocatalysts using ethanol and water mixtures. This study was undertaken to reach the following goals:

1. Preparation of titanium dioxide (TiO$_2$) and TiO$_2$ doped with gold nanoparticles (Au NPs) in various ratios (0.5, 1, 1.5, 2, and 2.5) % Au were prepared using the sol-gel method.

2. Studying the effects of doping TiO$_2$ with different ratios of Au NPs on the structural, morphological, and optical properties using various techniques (including XRD, XPS, FTIR, FESEM, TEM, BET, and UV-Vis).

3. Studying the photocatalyst performance of the prepared samples. Under the irradiation of ultraviolet light, the rate has been calculated MB dye degradation the of TiO$_2$ photocatalysts of varied doses (5, 10, 15, 20, and 25) mg and (0.5, 1, 1.5, 2, and 2.5) % Au/TiO$_2$.

1.4   Thesis Layout

This thesis consists of four chapters. **Chapter 1** is a general introduction, the problem statement, and the objectives. **Chapter 2** covers the basic ideas and literature review that provide an overview of nanotechnology and nanostructured materials. Additionally, the preparation of nanostructured materials is covered, along with a brief history of TiO$_2$ and Au, its crystal structure, and the process for producing TiO$_2$ NPs. An explanation of the fundamentals of photocatalysis is provided in this chapter. The photocatalytic

mechanism of the TiO_2 semiconductor with Au is demonstrated at the chapter's conclusion. **Chapter 3** is the methodology that describes in details the selected precursor materials and the process to produce TiO_2 and X% Au/TiO_2 nanoparticles. The fundamental principles of techniques, that were utilized to characterize the preparation samples, are briefly clarified. Finally, the experimental setup for the pure TiO_2 and X% Au/TiO_2 photocatalytic activity test will be elaborated on at the termination of this chapter. **Chapter 4** describes the findings on characterizations of pure TiO_2 and X% Au/TiO_2. In addition, the photocatalytic activity of the prepared TiO_2 and X% Au/TiO_2 NPs was estimated using the organic MB degradation experienced under UV irradiation. Finally, the chapter gives the conclusions and recommendations for future works.

Chapter 2
Fundamental Concepts and Literature Review

2.1 Introduction

This chapter presents a comprehensive introduction to nanostructured materials and methods for preparation and classifying them. In particular, the study of titanium dioxide, including its preparation techniques and various applications. And also, the metal of gold (Au) and the process by which it was doped with titanium. At the end of this chapter, there is an overview of pertinent literature.

2.2 Nanotechnology and Nanomaterials

"Nano" is a Greek word which means "dwarf." It is one billionth of a meter long. It has something to do with nanotechnology and nanoscience. This branch of science and technology is concerned with materials with at least one dimension ranging from 1 to 100 nm. The word "nanotechnology" was invented in 1974 by Norio Taniguchi. This was the name of an ion sputtering machine, and it referred to its extremely high accuracy and ultrafine structure in nanometers [21].

Nanotechnology is described as the design, configuration, characterization, and manufacture of materials as well as equipment and systems in a nanoscale. Nanotechnology has the potential to create new compounds with diverse chemical, physical, and biological characteristics, such as nanomaterials. As a result, nanotechnology has been applied in a variety of disciplines, including microprocessor technology and medical and scientific research. The science of nanotechnology and nanomaterials has shown obvious exponential growth in recent years. Scientists and researchers are attempting to enhance approaches for fabricating structures and devices with nanoscale compositions in a wide range of sizes and at a reasonable cost [22].

It may be employed in a variety of applications, including cosmetics, electrical devices, medical devices, automotive, food, and certain other consumer goods [23–26]. Despite recent advances in the synthesis and characterization of novel nanostructured materials, numerous hurdles remain, such as controlling size and shape [27]. Nanomaterials feature size and shape-dependent characteristics that result in unrivaled behavior as compared to bulk materials. Furthermore, as materials reach the nanoscale (about 100 nm), their physicochemical and chemical characteristics can change dramatically. Many unrivaled qualities have been attained at the nanoscale, including improved hardness [28], catalytic improvement [29], selective absorption [30], magnetic conjugation [31], and nonlinear optical attitude [32]. Improved characteristics are frequently the result of their small size, the vast surface area of atoms, interfacial constraints, and shape effects. Surface atoms are more energetic than inside atoms due to their profuse unsaturated bonds and high surface energy [33]. As particle size reduces, the ratio of (surface/volume) of a material increases and then it increases the percentage of total atoms visible as surface atoms. Nano-crystals come in a variety of forms, including rods, spheres, tubes, threads, and an assortment of irregular shapes. The physical properties of the materials are altered by the particle shapes.

2.3 Synthesis of Nanoparticles

Two methods for creating nanoparticles are shown in Fig. 2.1: top-down and bottom-up [34].

1- **Top-down approach:** The basic idea behind this method is to shrink the bulk material into the appropriate nanostructure size. Cutting, grinding, and etching are examples of nanoscale fabrication procedures. Top-down approaches may build nanostructures ranging in size from 1 to 100 nm [35].

2- **Bottom-up approach:** Bottom-up self-assembly refers to the building of a structure atom by atom, molecule by molecule, or cluster by cluster. Colloidal dispersion, which is utilized in the production of nanoparticles, is an excellent example of a bottom-up technique. The bottom-up technique has the benefit of producing nanostructures with fewer flaws and more homogenous chemical compositions [36].

These two procedures include sub-methods for creating nanoparticles.
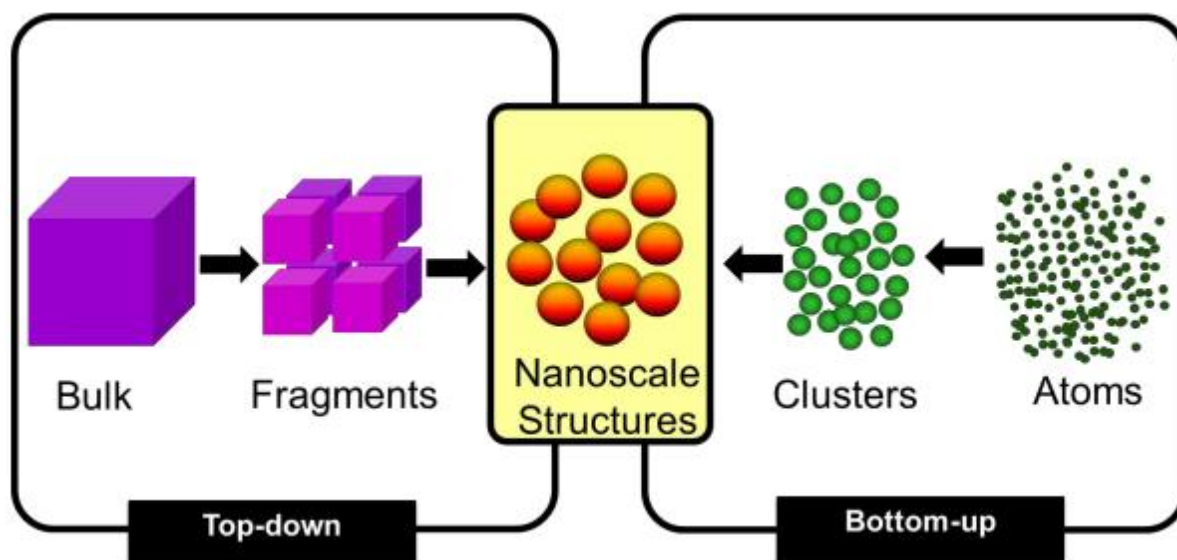
Figure 2.1**:** Schematic representation of the top-down and bottom-up techniques for metal nanoparticle production [36].

2.4 Classification of Nanomaterials

Nanostructures are classified into four types based on their degree of freedom as shown in Fig. 2.2. Zero-dimensional (nanostructures, such as nanoparticles, quantum dots, and nanospheres, imply that all three dimensions are on the nanoscale). One-dimensional (two-dimensional nanoscale structures such as nanorods, nanotubes, and nanofibers) [37]. Two-dimensional (the crystalline structure that is restricted to one-dimension nanometer scales such as nanosheets, nanoplatelets, and nanofilms) and three-dimensional (the dimensions surpass the nanometer scale (more than 100 nm such as bulk materials) structures are separated. These particle morphologies alter the physical properties of the materials [38].
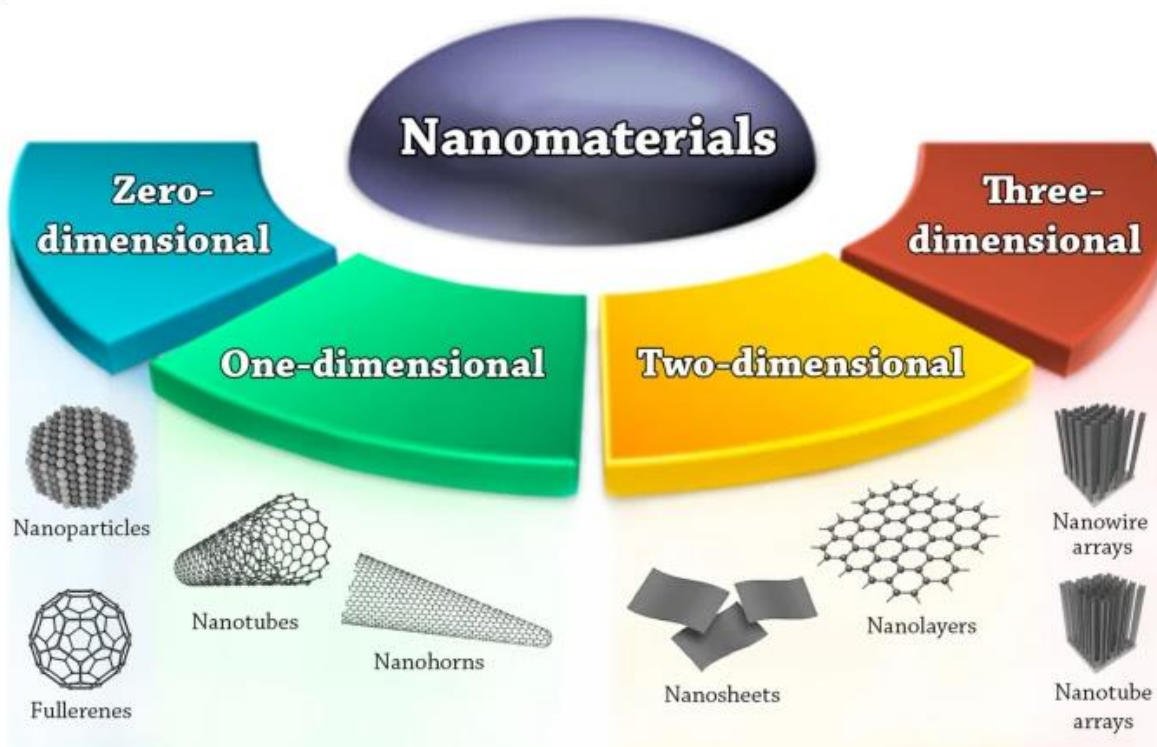
Figure 2.2: Dimensional classification of nanomaterials [38].

2.5 Titanium Dioxide (TiO$_2$)

TiO$_2$ is a chemical compound which belongs to the transition metal oxide family. TiO$_2$ crystal formations include rutile, anatase, and brookite. The three crystal shapes formed as a result of varying pressures and heat exerted by rock formations on Earth. The anatase and brookite phases are more stable at lower temperatures, but both will return to the rutile phase at high temperatures (450-850) °C. The energy gap for the three crystalline: rutile, anatase, and brookite phases are approximately equal to 3 eV, 3.2 eV, and ~3.2 eV, respectively, as a result, UV light ($\lambda = 387$ nm) is necessary [39], and the refractive index of TiO$_2$ is n = 2.488 for anatase, n = 2.609 for rutile, and n = 2.583 for brookite [40].

The general properties and the crystal structure of the three TiO_2 phases are summarized in Table 2.1.

Table (**2.1**): General properties of the TiO_2 phases.

Properties	Anatase	Rutile	Brookite
Crystal system	Tetragonal	Tetragonal	Orthorhombic
Molecule cell	4	2	8
Ti-O bond length (Å)	1.934	1.934	1.87- 2.04
Molecular weight (g/mol)	79.865	79.865	79.865
Energy gap (eV)	3.2	3.0	~3.2
Melting point (ºC)	Transformation to rutile phase at high temperature	1843	Transformation to rutile phase at high temperature

In Fig. 2.3, the tetragonal symmetry is present in all three phases, with each Ti atom octahedrally coordinated with six oxygen atoms. The majority of anatase is made up of point-sharing octahedra. On the other hand, rutile's edge-sharing of octahedra results in the formation of lengthy chains, making it the most thermodynamically stable of the three polymorphs; brookite, on the other hand, combines edge- and point-sharing. The phases that have been researched the most for photocatalytic applications are rutile and anatase. The characteristics of brookite are seldom discussed because it is generally photo-catalytically inactive and can be challenging to synthesize [41].
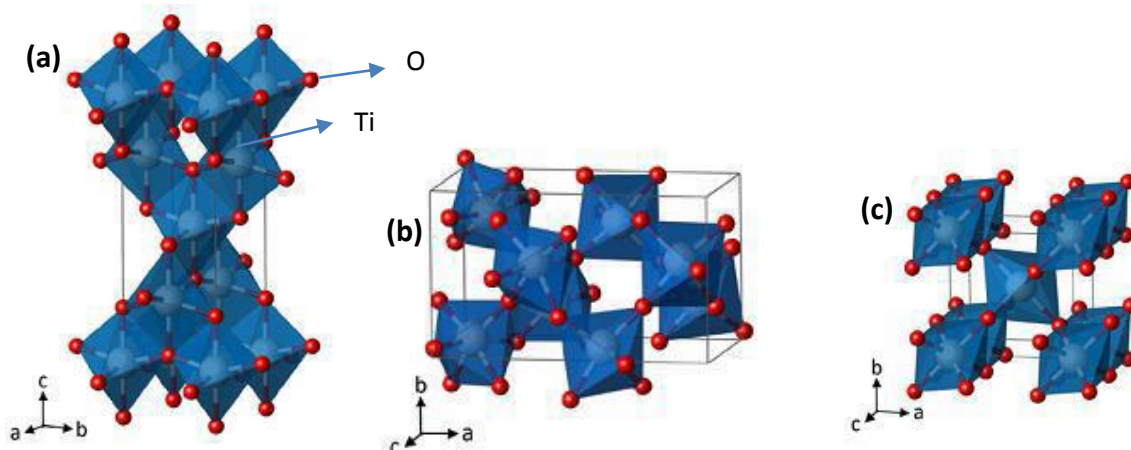
Figure 2.3: Crystal structures of TiO$_2$ (a) Anatase, (b) Rutile, and (c) Brookite [42].

2.6 Preparation Methods of TiO$_2$

There are several methods for producing TiO$_2$ nanoparticles, as shown here: the Solvothermal method, the Direct Oxidation method, the Hydrothermal method, the Microwave method, the Chemical Vapor Deposition (CVD), the Physical Vapor Deposition (PVD), the Electro-deposition, the Sonochemical method, and the Sol-Gel method [43–46]. The latter approach was chosen because of its unique advantages, such as considerably lower cost, precise composition control, excellent homogeneity, obtaining multiple phases from a metal oxide, ease of handling, low temperature, readily obtained, and wide-scale area.

The preferred technique for preparing titanium dioxide in laboratories is the sol-gel process. Tetra Isopropoxide (TTIP), one of the main precursors of titanium, is used to prepare TiO$_2$ by interacting with ethanol, as given by the following equation:

$$\text{Ti}\,[\text{OCH}\,(\text{CH}_3)_2]_4 \;+\; C_2H_6O \rightarrow \text{TiO}_2 \;+\; (\text{CH}_3)_2\text{CHOH} \tag{2.1}$$
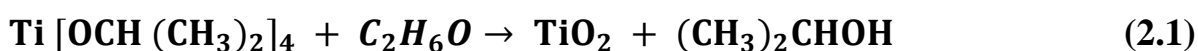
Water is often added to an alkoxide solution in alcohol. The presence of additives (e.g., acetic acid), the amount of water, and the pace of mixing all influence the type of inorganic results. Fig. 2.4 depicts the chemical structure of TTIP:
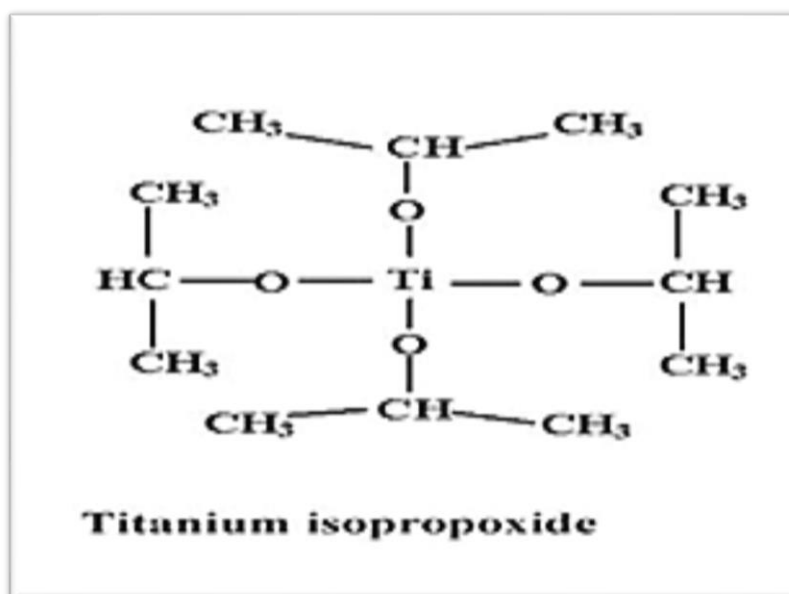
Figure 2.4**: TTIP's chemical structure [47].

2.7 Sol-Gel Method

Sol-gel processing is well recognized as a wet chemical approach for the synthesis and processing of inorganic and organic hybrid materials. The Sol is described as a colloidal suspension in liquid or solid particles with diameters in the range of 1-100 nm, tiny enough to disregard gravitational pull. The Gel word may be described as a continuous solid structure containing a continuous liquid phase [48].

The sol-gel approach may be used to build solid hosts and has numerous advantages, including low-temperature processing, excellent product homogeneity, and the ability to mold materials into complicated shapes in a gel

state. The ability to combine diverse chemicals at the molecular level allows sol-gel to build a wide range of host materials; for example, multiple studies used the sol-gel technique to synthesize a wide range of optical materials [49–51].

Metal alkoxide is a well-known sol-gel precursor; its basic equation is: M (OR)n (where n is the number of alkoxide groups (OR)), M is a central atom, and R is an alkyl group). The alkyl group is a ligand generated by removing one hydrogen from an alkane molecule, yielding the standard equations of alkyl and alkane C_xH_{2x+2} and C_xH_{2x+1} are some instances of alkyl groups [52]:

- Ethyl (C_2H_5), Methyl (CH_3), Butyl (C_4H_9), and Propyl (C_3H_7).

The sol-gel process has various advantages, including the fact that the temperatures required for all phases are near room temperature. Because grinding and pressing are not used, the goods produced by this process are of great purity. It is simple to produce high uniform-controlled doping. Highly porous and nanocrystalline materials are simple to create. On the other hand, the most significant drawbacks are the significant shrinkage in the final product and the lengthy processing time [53,54]. The sol-gel process chemistry includes the creation of a sol (a colloidal suspension) following a succession of hydrolysis and condensation reactions of the precursors. Metal alkoxides react quickly but are insoluble in water, thus a solvent such as ethanol (C_2H_5OH) is typically employed to create the precursor solution [55]. The alkoxysilanes, such as Titanium Tetra Isopropoxide (TTIP), are the most often utilized metal alkoxides. The first stage of the sol-gel process is the hydrolysis of precursors; the hydrolysis reaction includes the substitution of alkoxide groups (*OR*) with hydroxyl groups (*OH*). The general formula for the hydrolysis process [56] :

$$M\,(OR)_n + H_2O \rightarrow HO-M(OR)_{n-1} + R-OH \qquad (2.2)$$
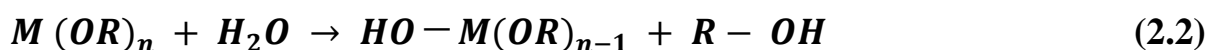
Where (*n*) denotes the number of alkoxide groups that vary with the central atom (*M*) [57]. In the case of (*Ti*) metal, the hydrolysis process is carried out using the equation [58].

$$Ti - (OR) + H_2O \rightarrow Ti - OH + R - OH \tag{2.3}$$
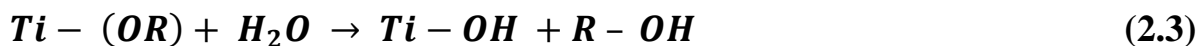
Because of the weak reaction rate of the hydrolysis process, a catalyst is sometimes required.

Depending on the amount of water and catalyst present in the solution, condensation occurs in response to the presence of any hydrolyzed precursor molecules in the solution at the same time as hydrolysis and follows a similar chemical pathway. Alcohol (alcohol condensation) and water (water condensation) are the two possible byproducts of the condensation process, which creates a Metal-Oxygen-Metal Bridge.

Eqs. (2.4) and (2.5), illustrate that the condensation reaction forms a titanium link (Ti-O-Ti) with a byproduct of water or alcohol [58].

$$Ti - OH + OR - Ti \rightarrow Ti - O - Ti + ROH \tag{2.4}$$

$$Ti - OH + OH - Ti \rightarrow Ti - O - Ti + H_2O \tag{2.5}$$
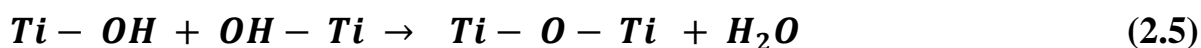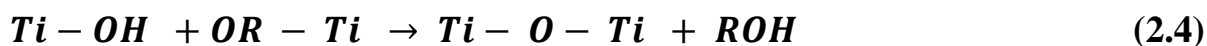
The reaction conditions control the size and properties of the oligomers and later macromolecules produced by this process [59]. Gel aging is an extension of the gelation process that entails a steady change in the properties and composition of a fully immersed gel in a liquid after the gel point. The major way of removing the liquid from the microscopic pores is drying since the gel comprises a substantial proportion of liquid and three-dimensionally linked holes inside the structure [60].

The liquid inside the pores experiences pressure gradients as a result of evaporation, which causes the network to be squeezed more tightly towards the surface than it is underneath, further decreasing the gel network. Additionally, the liquid flows from the bulk of the gel to cover a tiny area of the surface because the evaporation of the liquid cannot cover the entire surface without the creation of a meniscus on the pore surface [61].

Densification is the Gel's last treatment phase. Heat treatment of the porous gel at high temperatures is required to obtain powder from the gel. The pores are removed after the high-temperature treatment, and the densification temperature is highly dependent on the degree of connection of the pores, the dimension of the pores, and the surface area in the stature [62]. The steps of the sol-gel synthesis process are depicted in Fig. 2.5 [63].

Figure 2.5**:** Summary of the Sol-Gel method [63].

The conversion of a liquid (colloidal or solution) into a solid (or multiphase gel) is known as the sol-gel process. The structural and textural characteristics of the produced materials are influenced by different sol-gel process settings.

The initial reaction parameters of precursor material, molar ratio (R) of reactants, pH, solvent composition, temperature, aging, and drying conditions are primarily influenced by the sol-gel process [64].

2.8 Applications of TiO_2

TiO_2 NPs have sparked widespread interest due to their numerous advantages, including optical and electrical characteristics, strong photocatalytic activity, low cost, non-toxicity, and chemical stability [65]. Fig. 2.6 depicts the application of TiO_2. These applications include self-cleaning, water treatment, air cleansing, anti-fogging, and anti-bacterial effects [66].
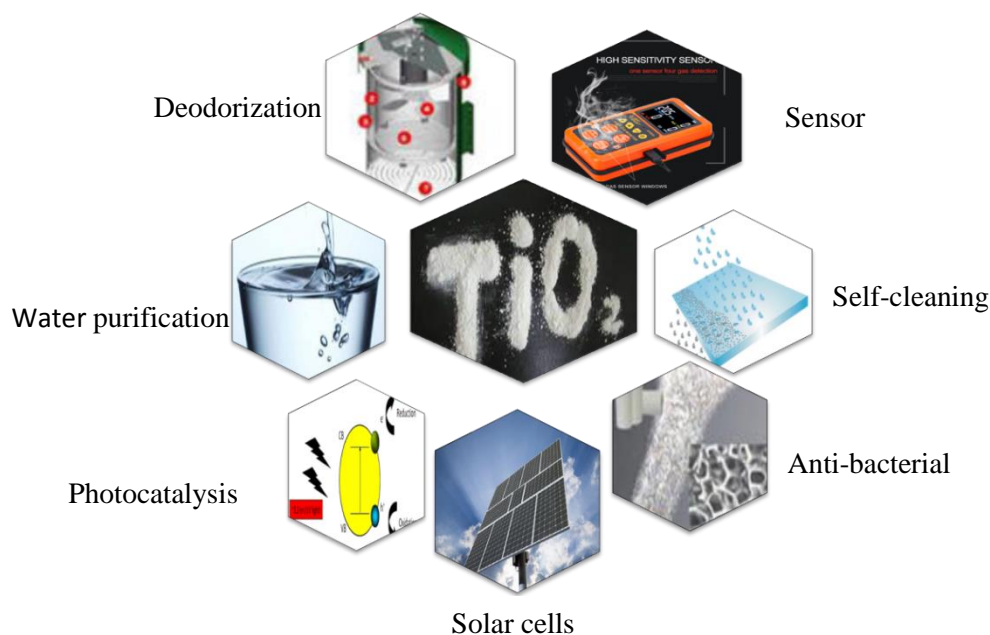
Figure 2.6**:** Application of TiO_2 NPs.

2.9 Gold (Au) Nanoparticles

The epitome of a noble element is gold. Gold nanoparticles can display characteristics that are very different from those of bulk gold [67]. Contrary to

bulk gold, nanoscale gold, for instance, displays a variety of vibrant colors that depend on particle size and shape [68].

The absorption of visible light at wavelengths of around 550 nm (or greater) is due to surface plasmon resonance, which is caused by the coupled oscillations of electrons at the surface of the nanoparticles [68–71]. In 1857, Michael Faraday found that stabilizing the tiny particles created by the aqueous reduction of gold chloride by phosphorus by adding carbon disulfide resulted in the production of a "beautiful ruby fluid" [72]. Noble metal nanoparticles, in particular gold nanoparticles, have been the subject of extensive investigation over the past few decades because of their unique electrical, optical, and catalytic characteristics [73–75]. Careful control of the size, shape, interparticle distance, and surface nature of gold nanoparticles increases these intriguing properties, which leads to intriguing applications in the fields of controlled drug release, thermal therapy, surface-enhanced spectroscopy, and catalysis, among others [76–79]. By changing the metal nanostructures' composition, size, shape, and structure (hollow versus solid), it is possible to tailor their properties.

Noble metal nanoparticles, such as Au, are appealing due to their optical characteristics. Au is an appropriate candidate since it is more stable and does not oxidize [80]. Another key technique is to tailor the TiO_2 band gap to improve photocatalytic activity [81]. Several methods for attaching metal NPs to nanostructured semiconductors have been used, including deposition precipitation, photo deposition, chemical deposition, and impregnation. Au NPs can be produced in a variety of shapes, such as nanospheres, nanorods, nanoshells, and nano prisms. Some of the morphologies displayed by Au NPs are depicted in Fig. 2.7 [82].

Figure 2.7**:** Shows the most common Au NPs shapes and assemblages [82].

TiO$_2$'s broadband gap (3.2 eV) severely limits its performance solely in the UV area (approximately 3% of solar light). Several attempts have been made to expand the photo responsibility of TiO$_2$ from UV to visible areas. Using noble metal nanoparticles to decorate TiO$_2$ nanostructures [83, 84]. Noble metal nanoparticles were used as active sites to collect photogenerated electrons and lower the rate of recombination. Furthermore, due to their surface plasmon resonance (SPR) capabilities in the visible region, metal nanoparticles can improve light usage [85, 86].

2.10 Principles of Photocatalysis

Photocatalysis is a mix of photochemistry and catalysis, which implies that both light and catalyst are required to promote a chemical process [87]. The photocatalytic reaction differs from standard catalyst reactions in that the catalyst material is activated by light rather than heat. Photocatalyst is a substance that increases the rate (time and speed) of a chemical process. Under

visible light and UV irradiation, it does not alter or is consumed in the process [88].

Photocatalysts can be divided into two groups: homogeneous photocatalysts and heterogeneous photocatalysts, depending on the photocatalyst phase with the reaction components. Homogeneous photocatalysts commonly dissolve in the reaction mixture when they are in the same phase as the chemical reaction's constituents. Metal salts, bases or acids, solvents, radical initiators, and enzymes are a few examples. Heterogeneous photocatalysts, on the other hand, frequently disintegrate in solvents and change in phase with the reactants. Examples of this class include supported metals, sulfides, solid acids and bases, and immobilized enzymes. Heterogeneous photocatalysts are hence opaque substances unless they have a porous structure [89].

A strong ultraviolet (UV) light is employed in the homogeneous photocatalyst to illuminate the contaminated water in the presence of O_3, Fe^{+3}, or H_2O_2. The presence of these components acts as a catalyst, and the reaction takes place in the bulk solution. The heterogeneous photocatalysis, on the other hand, involves one or more interaction processes that result in the formation of electron-hole pairs on the surface of semiconductor solid materials using an appropriate light. Because of the presence of solid catalyst material in a gaseous or liquid combination, the distribution and use of incoming light energy is substantially more difficult than in homogeneous operations [90].

Shape, specific surface area, crystalline structure, hydroxyl group surface density, and particle aggregate size are physical characteristics that have a significant impact on semiconductor photocatalyst efficiency [91]. Recent decades have seen concerns regarding the oxidation process, in particular the

removal of organic and inorganic impurities using semiconductor metal oxides [92].

The heterogeneous photocatalytic oxidation method utilizing TiO_2 has received increased interest as an alternative technique for both water and air cleaning [93]. The key characteristic of the heterogeneous photocatalyst is that no original material remains. That is, no sludge residue is required for disposal since the process converts contaminants into innocuous byproducts such as CO_2 and H_2O [94]. In heterogeneous photocatalyst materials, the initial step is the creation of electron-hole pairs. An electron (e^-) is raised from the valence band to the conduction band when a semiconductor material is exposed to a photon with energy (hv) equal to or greater than the bandgap value, leaving a positive hole (h^+) in the valence band.

2.11 Photodegradation Mechanism

This mechanism proposes a realistic reaction mechanism for the photodegradation of dyes on Au/TiO_2 NPs under UV irradiation. Because TiO_2's band gap is in the UV region, electrons in the valance band (VB) are promoted to the conduction band (CB) when exposed to UV light [95]. The electrons in the CB can then be transported to the adsorbed O_2 on the surface of TiO_2 to generate superoxide radical anions ($O_2^{\cdot -}$) [96]. Furthermore, in the case of metal nanoparticle doped TiO_2, the metal nanoparticles may be thought of as an electron sink, where electrons in the conduction band can migrate to the noble metal surface, avoiding electron-hole (e^- - h^+) pair recombination [97– 99]. Thus, the transfer of electrons from the photocatalyst's core to the metal surface leads to improved photo quantum efficiency, which might explain the current nanogold-doped systems' high photoactivity even when exposed to low-

intensity UV from sunshine. The transferred electrons at the metal surface aid in the production of the oxygen superoxide radical anion. The holes in the VB interact with the water molecules, causing the creation of hydroxyl radical ($^\bullet$OH) and proton. Protonation of the superoxide anion ($O_2^{\bullet-}$), generates $^\bullet$OOH radicals, which then react with H_2O to form the $^\bullet$OH radical [100].

These $^\bullet$OH radicals are what break down the color molecules. Previous research has demonstrated that photoactivity requires the presence of $^\bullet$OH radicals [100–103]. Therefore, the insertion of Au NPs and an increase in the quantity of nanogold particles can significantly increase TiO_2's photoactivity. If there are more Au NPs on the support, the TiO_2 CB's electron migration to the Au surfaces will move more quickly, facilitating the transmission of electrons to the adsorbed O_2 molecules [104, 105]. This encourages the synthesis of more $O_2^{\bullet-}$, which in turn encourages the formation of more $^\bullet$OH, which is in charge of fading the color. This explains why dye degradation has been seen to increase in comparison to existing photocatalysts when Au doping increases. Fig. 2.8 shows a schematic representation of the photodegradation route [106].
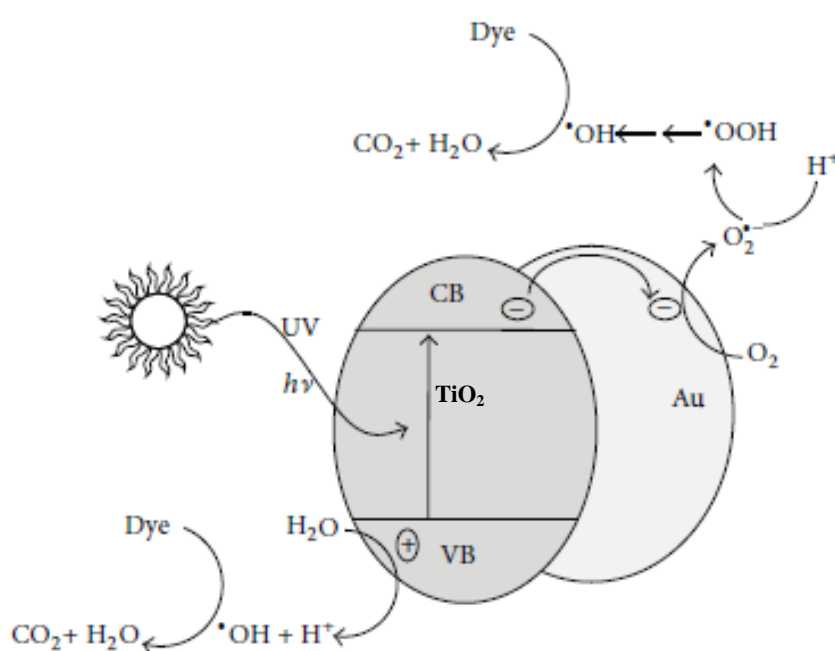
Figure 2.8: Possible dye photodegradation process over Au NPs doped TiO_2 [106].

2.12 Literature Review

Wen *et al.* [107] in 2013 synthesized and investigated Au/TiO_2 nanotubes with Au NPs precipitated by deposition-precipitation method (DP) on visible photocatalysis properties. The optimal visible photocatalytic activity was observed in the sample Au/TiO_2 with 3 wt. % loading of Au NPs and calcining after 350 °C. Transmission electron microscopy revealed Au NPs with a diameter of 4.16 nm at the interface between the anatase and rutile phases in the optimal sample. The presence of these joint active sites at the interface facilitated charge separation, leading to enhanced photocatalytic efficiency. This enhancement was attributed to the combined effect of enhanced visible absorption and the anatase/rutile mixed-phase composition.

In the work of Chen *et al.* [108] in 2015 two-dimensional TiO_2 nanosheet films with visible light trapping nanostructures were fabricated using an alkali hydrothermal reaction. Metallic Au nanoparticles (NPs) were deposited on the TiO_2 film surface through a microwave-assisted reduction process. The localized surface plasmon resonance (LSPR) of Au NPs is enhanced by the overlapped light harvesting nanostructures, resulting in LSPR absorption with peaks at 389 nm and 540 nm. The photocatalytic performance of TiO_2 is promoted by the synergetic effect between the overlapped light harvesting nanostructures and improved charge carrier separation processes. The optimal sample (0.6 Au/TiO_2 film) shows faster MB degradation compared to pure TiO_2 film under UV and UV-visible light irradiation. This study presents a simple strategy for developing efficient film-shaped plasmonic photocatalysts.

Salgado *et al.* [109] in 2016 synthesized Au nanoparticles deposited onto commercial TiO_2 (P25, nonporous, 70% anatase, and 30% rutile) by deposition-precipitation using urea. In brief, urea and $HAuCl_4.3H_2O$ were dissolved in distilled water. Titania was, then, added to this solution, which was held at 80 °C with steady stirring for 16 hours. Following deposition, the sample was recovered by centrifugation, cleaned four times in water at 50 °C, dried for two hours at 80 °C, and then thermally treated under air using a heating ramp at 300 °C. The resulting Au/TiO_2 photocatalyst displayed non-porous morphology, a bandgap energy of 2.68 eV, a BET surface area of 56 m^2 g^{-1}, and an actual Au content of 0.5 wt.%.

Campos *et al.* [110] in 2017 synthesized $Au–TiO_2$ photocatalysts using a microwave-assisted sol-gel method. They used X-ray diffraction (XRD) and UV-Vis diffuse reflectance spectroscopy (DRS) to determine characterization. The particle sizes were determined using the Scherrer equation. Changes in the band gap energy were observed based on the weight percentage of the dopant. X-ray diffraction patterns indicated the presence of the crystalline anatase phase and no rutile phase in both samples. UV-Vis DRS revealed that the band gap decreased with increased metal load, indicating a band gap energy variation from 3.2 eV (pure TiO_2) to 2.98 eV for the sample loaded with gold. Which can be related to the metal load in the photocatalyst.

Mehta *et al.* [111] in 2017 described the synthesis of gold-titania (Au/TiO_2), which increased photocatalytic performance for the destruction of alizarin dye, and is generated by the homogeneous deposition–precipitation (HDP) method through mesoporous nanostructure. The optical properties of Au/TiO_2 exhibit a distinctive surface plasmonic absorption band at 520 nm, while the X-ray diffraction (XRD) pattern displays the tetragonal geometry and FCC unit cell structure of the anatase phase of TiO_2. Gold's elemental state

(Au^0) is shown via X-ray photon spectroscopy (Au $4f_{7/2}$ at 84.0 and Au $4f_{5/2}$ at 87.7 eV). With a rise in Au content, it was observed that specific surface area decreased (169, 141, 130, and 119 m^2/g for 1, 2, 3, and 4 wt. %, respectively). Better charge delocalization is the reason why the mesoporous Au/TiO_2 nanocomposite outperformed the commercial nano-TiO_2 (P25) in terms of catalytic activity.

Weng and Yu [112] in 2018 fabricated anatase TiO_2 NPs attached to larger anisotropic Au morphologies by a two-step microwave-assisted method. Polyvinylpyrrolidone (PVP) is used as a reducing, capping, and stabilizing agent throughout the polyol method to create the TiO_2/Au NPs. The PVP was eliminated by calcination at low temperatures to maximize the contact between the titania and the gold and enhance electron transmission. The system operates at 450 °C, which is the ideal calcination temperature. The outcome showed high photocatalytic activity for TiO_2-based photocatalysts with big Au NPs (particle size 50 nm) and high Au loading.

Aswathy *et al.* [113] in 2019 successfully manufactured pure and Au-doped TiO_2 nanofibers (Au wt. % = 0.5, 1, 2, and 3) by electrospinning followed by annealing at 550 °C. The photocatalytic activity of pure and Au-doped TiO_2 nanofibers in water was investigated using ultraviolet (UV) and visible light irradiation independently. The photocatalytic activity of pure TiO_2 nanofibers is found to be greater when exposed to visible light than when exposed to UV light. However, the rate of MB breakdown in Au-doped TiO_2 nanofibers is faster under UV light than under visible light. Under UV irradiation, the efficiency of photodegradation is found to be somewhat higher for 1 wt. % Au doped TiO_2 nanofibers than pure TiO_2 nanofibers.

The study of Truppi *et al.* [114] in 2019 investigates the photocatalytic degradation of water pollutants using TiO_2/Au NPs nanocomposites prepared using a co-precipitation method. The material was calcined at varying temperatures, obtaining up to 20 g of catalysts. The photocatalytic performance was tested under UV and UV-Vis irradiation, with TiO_2/Au NPs, calcined at 450 °C showing faster degradation rates for Methylene Blue and Nalidixic Acid under UV and visible light. The results suggest that the high photoactivity of TiO_2/Au NPs in the visible range can be profitably exploited in photocatalytic applications, offering potential environmental remediation solutions.

Kholikov *et al.* [115] in 2021 reported that the gold nanoparticles (Au NPs) had been loaded on the surface of TiO_2 nanoparticles by a deposition-precipitation (DP) method. Using $HAuCl_4.4H_2O$ as preparation material, different mass percentages of Au (1.0, 2.0, 3.0, and 4.0%) were deposited on the surface of TiO_2 nanoparticles. The outcomes demonstrated that the produced Au/TiO_2 nanocomposite exhibited outstanding visible light photo-activity employed for the breakdown of hazardous contaminants and showed a 36-fold increase in photoactivity over pure TiO_2.

Liu and He [116] in 2022 investigated the efficacy of nanoparticles with an Au@TiO_2 core-shell for the photolysis of MB under solar light radiation. They successfully produced nanoparticles using a hydrothermal approach. They note that the optical bandgap value of Au@TiO_2 is reduced due to Au integration and defects. In Au@TiO_2 as well as reducing the charge transfer resistance and recombination kinetics. Au@TiO_2 removed 90% of MB solution in 60 minutes under solar light radiation. The rapid decomposition rate of Au nanoparticles was related to their SPR absorption properties. The proposed photocatalyst was effective in degrading methyl bromide in an actual sample of industrial effluents for paint and dye.

Yu *et al.* [117] in 2023 prepared rutile/anatase TiO_2 homojunction using sol-gel synthesis with nitric acid as a peptizing agent. The photocatalytic performance of 1% Au/TiO_2- HNO_3 was evaluated, showing good results in hydrogen evolution rate and methylene blue degradation under visible light irradiation. The composition ratio of rutile and anatase phases in TiO_2- HNO_3 was contributed to the enhanced charge transfer and decreased electron-hole recombination, favorable for photocatalytic performance. Additionally, the strong metal-support interaction and localized surface plasmon resonance of Au species accounted for the better performance of Au/TiO_2- HNO_3.

Chapter 3

Methodology

3.1 Introduction

This chapter presents the methodology employed in producing nanoparticles comprising pure TiO_2 and X% Au/TiO_2, employing the sol-gel approach. The methods used in this study to characterize the results will be elucidated. The photocatalytic activity of the materials for degrading methylene blue's (MB) aqueous solution will also be described. A schematic diagram of the distinct stages undertaken in this investigation is presented in Fig. 3.1 to provide a comprehensive understanding of the experimental process.
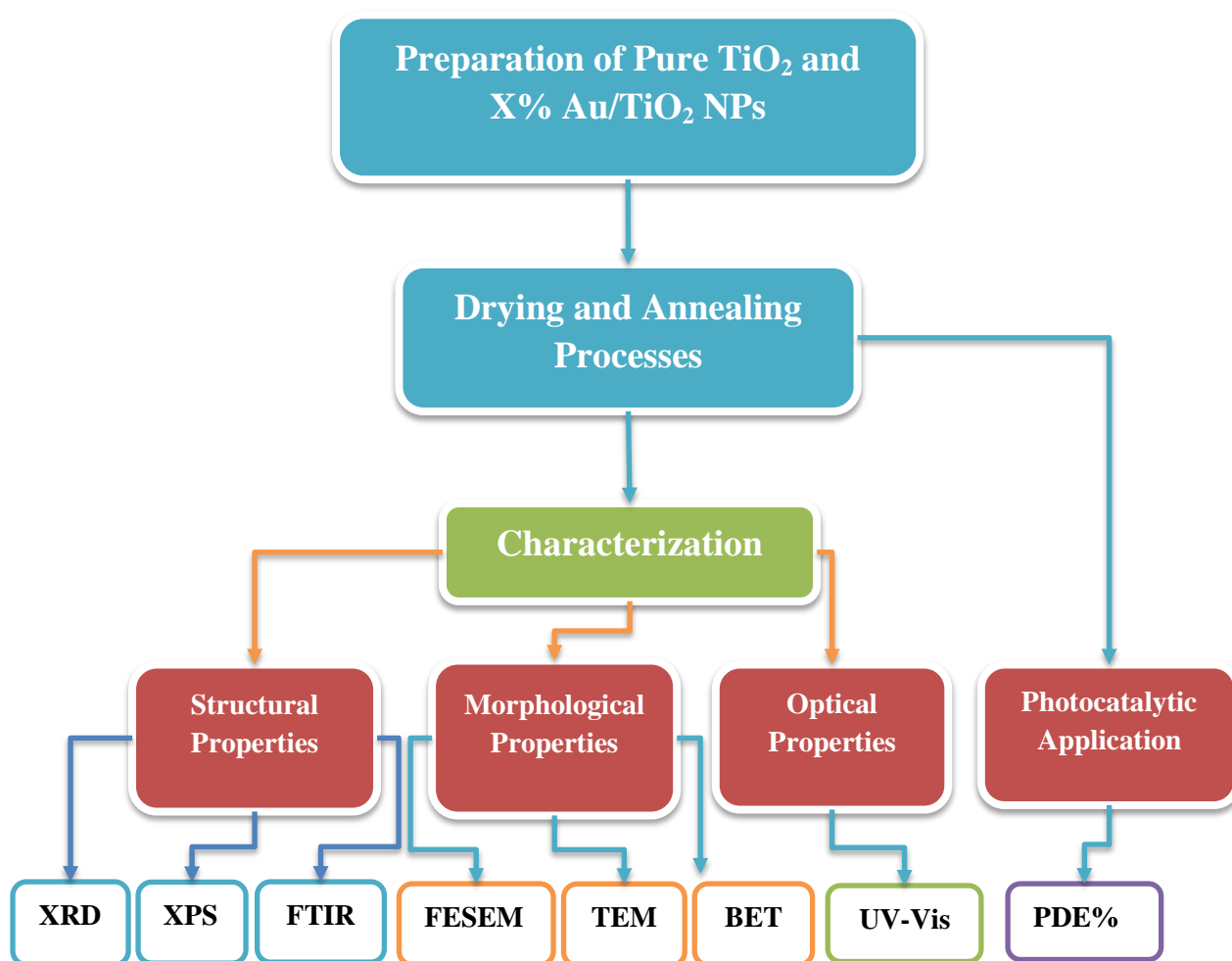
Figure 3.1**:** A schematic diagram of the practical steps in the present work.

3.2 Samples Preparation

3.2.1 Chemical materials

The precursor, solvent, and other chemical materials that were used in this work are summarized in Table (3.1).

Table **(3.1):** Specification of chemical materials utilized in this work.

Chemical material	Molecular formula	Molecular weight (g/mol)	Purity	Company
Titanium Tetra Isopropoxide (TTIP)	$C_{12}H_{28}O_4Ti$, or Ti $[OCH(CH_3)_2]_4$	284.26	97%	Sigma-Aldrich company
Hydrogen Tetrachloroaurate Trihydrate	$HAuCl_4.3H_2O$,	393.83	99.9%	Glentham
Deionized Water	H_2O	18	The high degree of purity/ free of additional ions	Chemical lab.
Ethanol (EtOH)	C_2H_6O or C_2H_5OH	46.07	99.9%	J. T. Baker
Hydrochloric Acid (HCl)	HCI	36.46	36.5- 38.0%	J. T. Baker
Methylene Blue (MB)	$C_{16}H_{18}ClN_3S$,	319.85	99%	Merck Organics

3.2.2 Preparation of TiO₂ nanoparticles

First, 10 ml of TTIP was added dropwise to the beaker containing 50 ml of ethanol (EtOH) under vigorously stirred at 600 rpm for 10 min. After the titration process was completed, the solution's color changed from clear to milky white, suggesting the production of TiO_2 NPs, which was marked as solution A. Next, a mixture of 50 ml ethanol, 10 ml water, and 1 ml concentrated hydrochloric acid (HCl), which is marked as solution B, was added dropwise to solution A under continued stirring for 30 min. The final solution (A+B) will keep immobile for two nights until the formation of the gel as shown in Fig. 3.2.
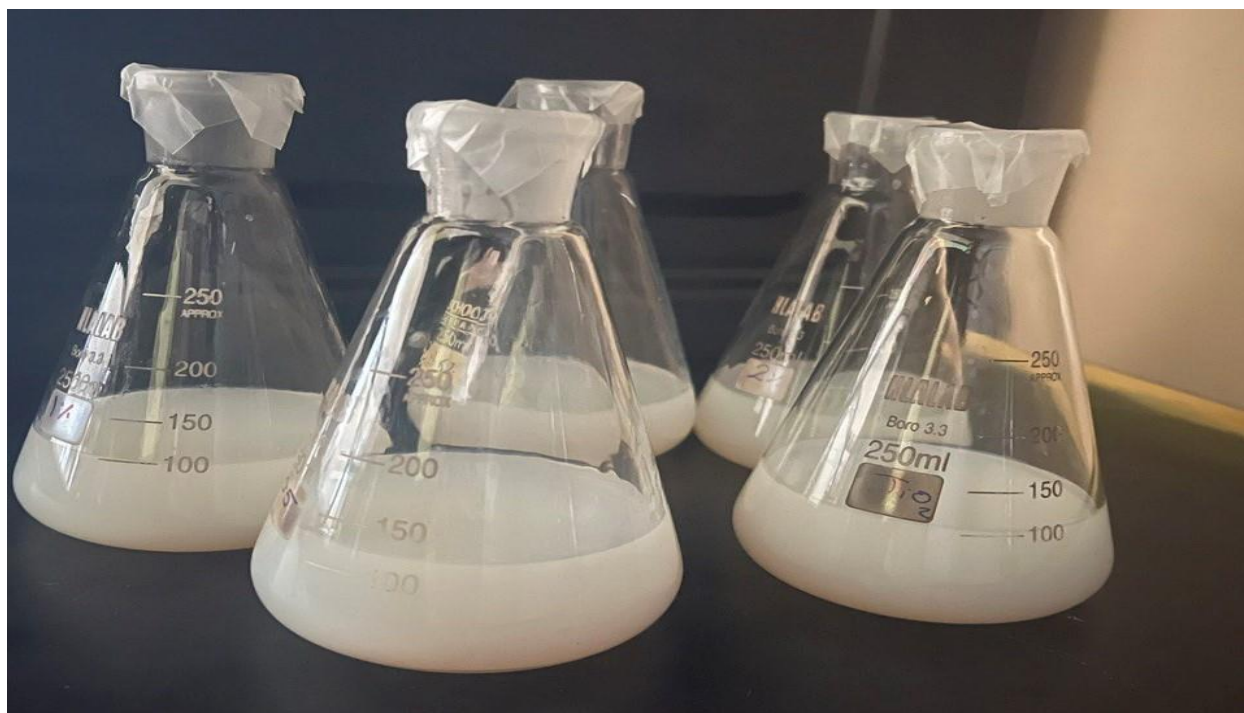
Figure 3.2**:** Images of gel composition before drying.

Then, the drying process takes place, where the samples are placed in the oven for about 60 hours (h) at a temperature of 75 °C to get rid of unwanted materials. After this step, the powder was obtained by manually grinding the sample in a mortar and pestle. Then the sample was annealed using an oven under an ambient atmosphere at 450 °C for 2 h to improve the crystallinity, as shown in Fig. 3.3.
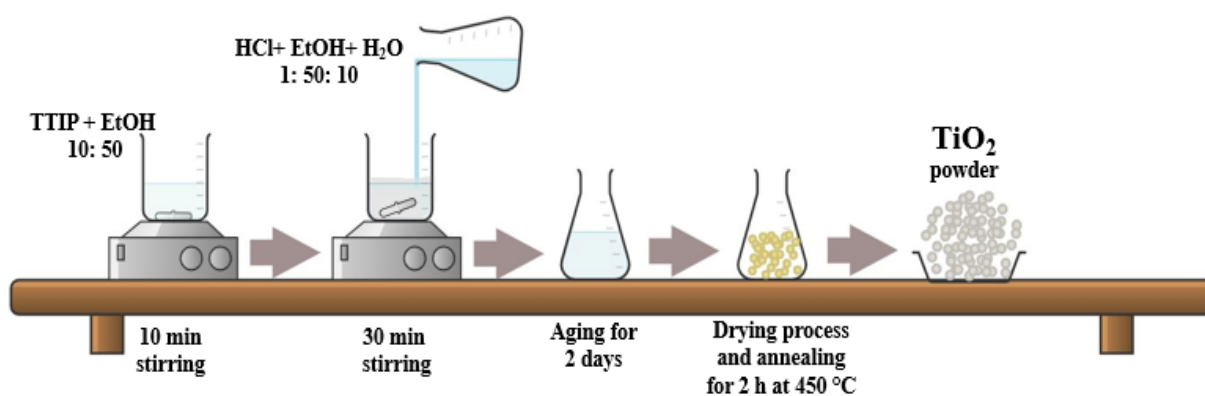
Figure 3.3**:** Stapes of preparing pure TiO_2 NPs.

3.2.3   Doped TiO_2 samples preparation

3.2.3.1 Preparation of the gold solution: Hydrogen tetrachloroaurate trihydrate ($HAuCl_4.3H_2O$, 1 g) was dissolved in dilute hydrochloric acid (HCl, 1 M) under vigorous stirring at room temperature, and kept in the dark which remark as solution A1.

3.2.3.2 Preparation of the Au/TiO_2 NPs: For the preparation of X% Au/TiO_2 NPs, two solutions were prepared. Solution A2 which consisted of 10 mL of TTIP dissolved in 50 mL of absolute ethanol and stirred for 10 min until the solution turned from transparent to milky color. Then, solution A1 was added dropwise in different ratios (0.5%, 1%, 1.5%, 2%, and 2.5%) Au under stirring

at 600 rpm to solution A2. The value of 0.5% Au is approximately equivalent to 50 μm of the TTIP percentage used, and so on for other percentages.

Solution B: consisted of 50 ml ethanol, 10 ml water, and 1 ml concentrated HCl, respectively. After 30 minutes of continuous stirring of solution A1, solution A2 was added. Afterward, the mixture was transferred to a glass flask and left undisturbed for 48 h to allow the gel to form.

Next, the samples were dried to evaporate unwanted materials. This involved placing the samples in an oven set at 75 °C for approximately 60 h. Finally, the obtained powder was manually ground using a mortar and pestle, as shown in Fig. 3.4 (a, b, and c). Subsequently, the powder was annealed in an ambient atmosphere at 450 °C for 2 h. The calcination process improved the crystallinity of the nanoparticles, leading to enhanced photocatalytic activity and optical properties. All the processes are summarized in Fig. 3.5.
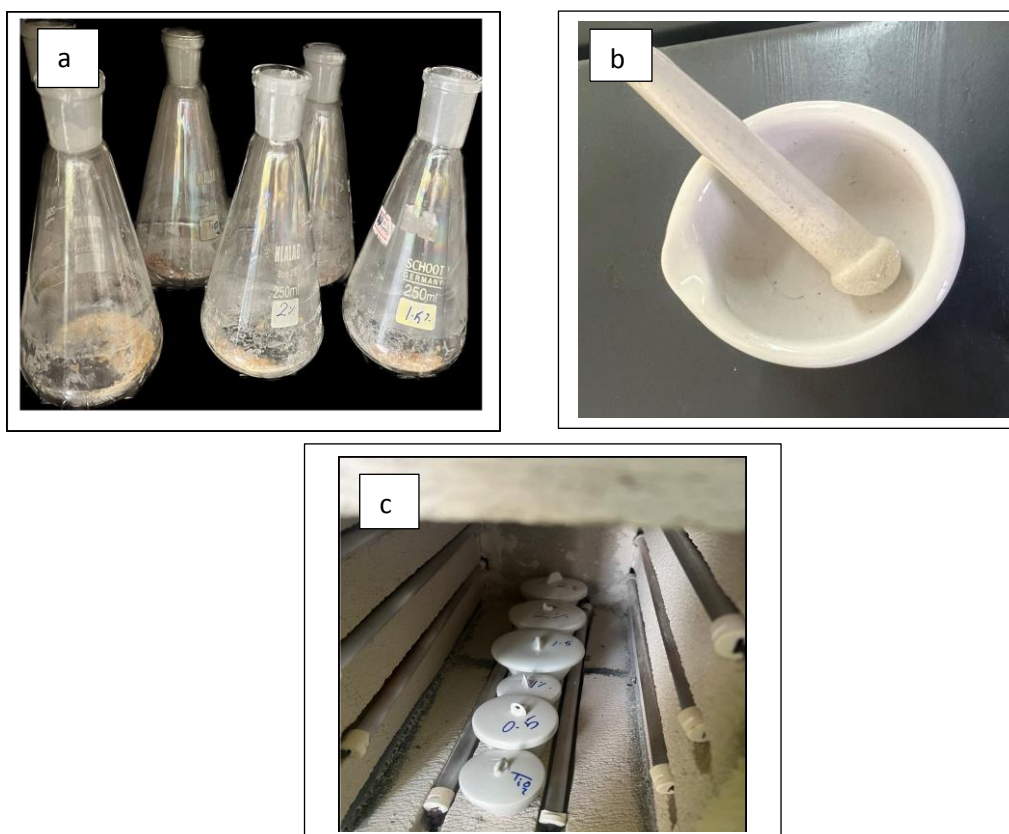
Figure 3.4: Image of the samples at drying and calcination process a) samples after drying, b) grinding tool, and c) annealing stage.
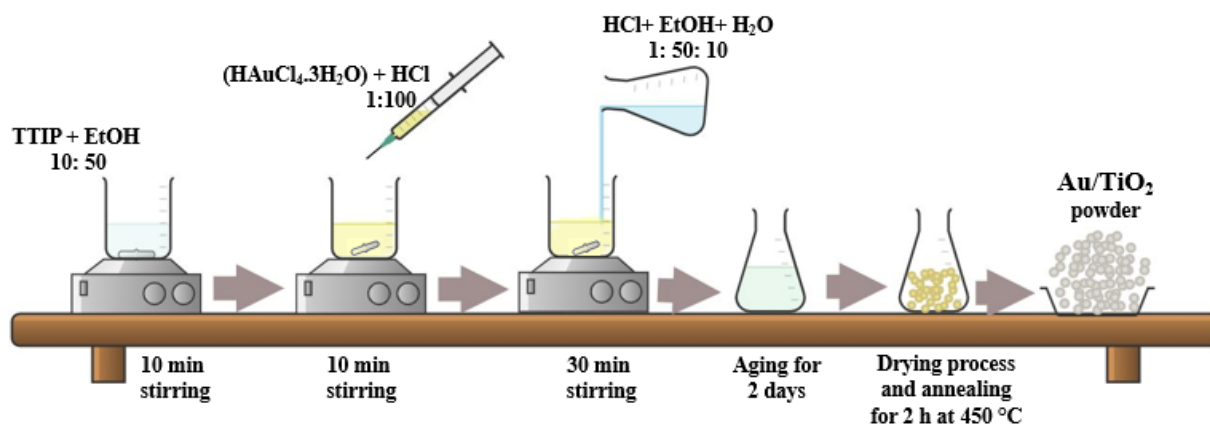
Figure 3.5: Stapes of preparing X% Au/TiO$_2$ NPs.

3.3 Techniques of Characterization

Many types of equipment have been used to examine the physicochemical and photocatalytic characteristics of pure TiO$_2$ and X% Au/TiO$_2$ NPs. The section summarizes the characterizations and analytic approaches used in this work.

3.3.1 X-ray diffraction (XRD) analysis

The technique XRD is used to determine the crystal structure and crystallite size of nanomaterials. XRD is based on the diffraction of X-ray beams as a function of incident beam angle. These X-rays are created by bombarding a specific metal with high-energy electrons (typically Cu or Mo), which are then filtered and focused into monochromatic radiation that is aimed at the sample. When the criteria of Bragg's law are met, the interaction of the X-ray beam with

the surface of the sample produces reflected photons from constructive interference:

$$2d \sin \theta = n\lambda \qquad (3.1)$$

Where d denotes the planar spacing, θ is the angle between the incidences and normal to the lattice plane, n denotes the order of reflection, and λ corresponds to the X-ray wavelength.

Furthermore, the crystallite size (D) of the material can be calculated from the diffraction data using Scherrer's equation:

$$D = \frac{K\lambda}{B \cos \theta} \qquad (3.2)$$

Where k is a dimensionless shape factor, λ is the X-ray wavelength, B is full width at half maximum, and θ is the angle.

Analysis-related data: XRD Philips type PW1730 with Cu Kα radiation source at a wavelength of 1.54056 Å with current (30 mA) and voltage (40 kV) was used. Diffraction data were characterized at 2θ in the scanning range of 10°-80° and step width of 0.02° and step time of 0.01 seconds. The X'pert High score software was used to analyze the atomic structure. The prepared samples were analyzed at the University of Tehran's School of Chemical Engineering - Iran.

3.3.2 X-ray photoelectron spectroscopy (XPS) analysis

The elemental makeup of a material's surface (between depths of 1 and 10 nm) can be ascertained using XPS, also known as electron spectroscopy for chemical analysis (ESCA). Further applications include determining these elements' chemical or electrical states.

The incident X-rays from the monochromatic X-ray source cause the core-level electrons in the sample atoms to be ejected. A photoemitted core electron's energy depends on its binding energy and is unique to the element it was released from. An outer electron fills the core hole after the incident X-ray expels the core electron. The emission of an Auger electron or a distinctive X-ray balances the energy of this transition. The spectrum of the surface composition is produced by measuring the quantity of photoelectrons and Auger electrons as a function of their energy. The relative amount of the element that that peak represents is expressed as the area under the peak in the spectrum. The element's chemical state is indicated by the peak's precise location and form.

Analysis-related data: XPS BESTEC EA10 spectrometer with a monochromatized Al-Kα radiation, a concentric hemispherical electron energy analyzer under vacuum ($2*10^{-10}$ mbar), and a pass energy of 23.5 eV was used to characterize the chemical species at the Interfaces of the materials. C 1s (285 eV) was used as a reference peak to correct for charging effects during acquisition. After accounting for the removal of a non-linear (Shirley) background, the core level spectra were used in calculating the quantitative surface chemical composition. The prepared samples were analyzed at the University of Tehran's School of Chemical Engineering - Iran.

3.3.3 Fourier transform infrared (FTIR) analysis

Infrared radiation (IR radiation) is an electromagnetic radiation that is invisible and has a wavelength range of 0.74 μm to 100 μm. It was first discovered by Sir William Herschel in 1800. Based on its various sections, such as near-infrared (12820 to 4000 cm^{-1}), mid-infrared (4000 to 400 cm^{-1}), and far infrared (400 to 33 cm^{-1}), IR spectroscopy is a technique that is employed in

numerous experiments. Studying overtones, combinations, or harmonic vibrations uses the near-infrared area. Far infrared is used to analyze inorganic substances, while mid-infrared is utilized to determine the structure of organic molecules[118]. In this thesis, the mid-infrared band (4000 to 400 cm^{-1}) of IR spectroscopy is employed to identify the functional group of X% Au /TiO$_2$ samples.

Analysis-related data: The samples were examined by combining KBr, TiO$_2$, and Au/TiO$_2$ NPs in the form of a pellet. The prepared samples were examined (FTIR-8400S, SHIMADZU) device at the University of Kerbala, College of Science, Department of Chemistry.

3.3.4 Field emission scanning electron microscopy (FESEM) and energy dispersive x-ray spectroscopy (EDX) analysis

FESEM, a type of electron microscopy capable of providing higher-resolution and less electrostatically distorted pictures, is mostly useful for assessing the surface structure of the subject. FESEM can provide information on the elemental composition of materials photographed with EDX and sample images. As a form of spectroscopy, EDX investigates a sample through interactions between light and matter, examining X-rays in this example. The fundamental idea that each periodic table element has a unique electronic structure and consequently a unique reaction to electromagnetic waves underpins its characterization capabilities [119,120].

Analysis-related data: FESEM model TESCAN - (MIRA3, LMU) was used to characterize the surface morphology of pure TiO$_2$ and X% Au/TiO$_2$ NPs samples. The prepared samples were analyzed at the University of Tehran's School of Chemical Engineering- Iran.

3.3.5   Transmission electron microscopy (TEM) analysis

TEM is an imaging technology that works in the same way as a light microscope but uses electrons instead of light. High-energy electrons, similar to SEM, flow through a series of lenses under a vacuum to produce the appropriately focused beam of electrons that hit the surface of the sample [121]. The interaction of electrons with the sample produces X-rays, which are recorded on a high-resolution fluorescence screen to learn about the morphology, crystallization, and composition of the examined substance. A TEM sample should be thin enough to allow enough electrons to flow through to provide an image with little loss of energy. As a result, sample preparation is critical for TEM analysis.

Analysis-related data: TEM model Philips EM 208S. The size of the metal particle can be measured using the Image J program. The prepared samples were analyzed at the University of Tehran's School of Chemical Engineering - Iran.

3.3.6 Specific surface area (BET) analysis

Brunauer Emmett Teller (BET) is a critical approach for determining the specific surface area and pore size distribution of various nanomaterials. The defined surface area of nanostructured materials is typically assigned by the BET process's physical absorption of inert gas molecules on the surface of the solid substance. The specific surface area of the produced materials in this work was examined by micropolitics (Tristar II series). The average pore diameter and pore volume of the sample were determined using the Barrett-Joyner-

Halenda (BJH) formula from the N_2 adsorption-desorption isotherm (purity 99.999%).

Analysis-related data: BET BELSORP Mini II, the porous properties were examined by N_2 adsorption and desorption isotherms at 77 K. The prepared samples were analyzed at the University of Tehran's School of Chemical Engineering- Iran.

3.3.7 Ultraviolet-visible spectroscopy (UV-Vis) analysis

UV-Vis spectroscopy can be used to analyze the optical features of nanostructures such as absorption coefficient, absorption and reflectance spectra, and energy bandgap [122]. Absorption is a type of spectroscopy that is utilized in the ultraviolet-visible region. UV-Vis absorption spectroscopy provides information on light absorption as a function of wavelength, characterizing the electronic transitions in the samples under investigation. The UV-Vis spectrophotometer compares the intensity of light passing through a sample and the intensity of light before passing through the sample [123]. Beer's law can be used to calculate absorbance (A):

$$A = -log\frac{I}{I_o} \tag{3.3}$$

Where (I) is the intensity of light passing through the sample and (I_o) is the intensity of light before passing through the sample.

The UV-Vis spectrophotometer was used in this investigation to monitor the degradation of MB concentration during photocatalytic activity evaluation using the generated pure TiO_2 and X% Au/TiO_2 NPs samples. The ultraviolet spectrum was captured between 200 and 800 nm. To determine the rate of

deterioration as a function of irradiation time, the maximum absorption wavelength of MB (664 nm) was used.

Analysis-related data: All measurements were performed using a Shimadzu-UV-VIS Spectrophotometer (UV-1900i) at the University of Kerbala, College of Science, Department of Physics.

3.3.7.1 Band gap energy and Tauc plot

Direct band gap energy (Eg) was calculated in (eV) by utilizing from UV-visible spectrophotometer by using the Tauc equation [124]as mentioned in equation (3.4):

$$(\alpha h\upsilon)^m = A(h\upsilon - Eg) \tag{3.4}$$

Where α is the absorbance coefficient for all samples, h is Plank constant ($6.63*10^{-34}$ J s), υ is the frequency of light equal to (C/λ), here C is light speed, A is optical constant, and m is 2 for direct transition.

3.4 Photocatalytic Activity of TiO$_2$
3.4.1 Preparation of methylene blue solution and its calibration curve

To construct the calibration curve, solutions with varying concentrations of MB (5 ppm, 10 ppm, 15 ppm, 20 ppm, and 25 ppm) were prepared. These solutions were exposed to UV light within the wavelength range of 450-800 nm and their absorption values were recorded. The concentration of MB was determined using a UV-visible Spectrophotometer. Highest absorbance of MB at λ max = 664 nm was observed across all solutions. The calibration curve for

MB dye was used at a wavelength of 664 nm to ascertain the concentration of the dye. As shown in Fig. 3.6.
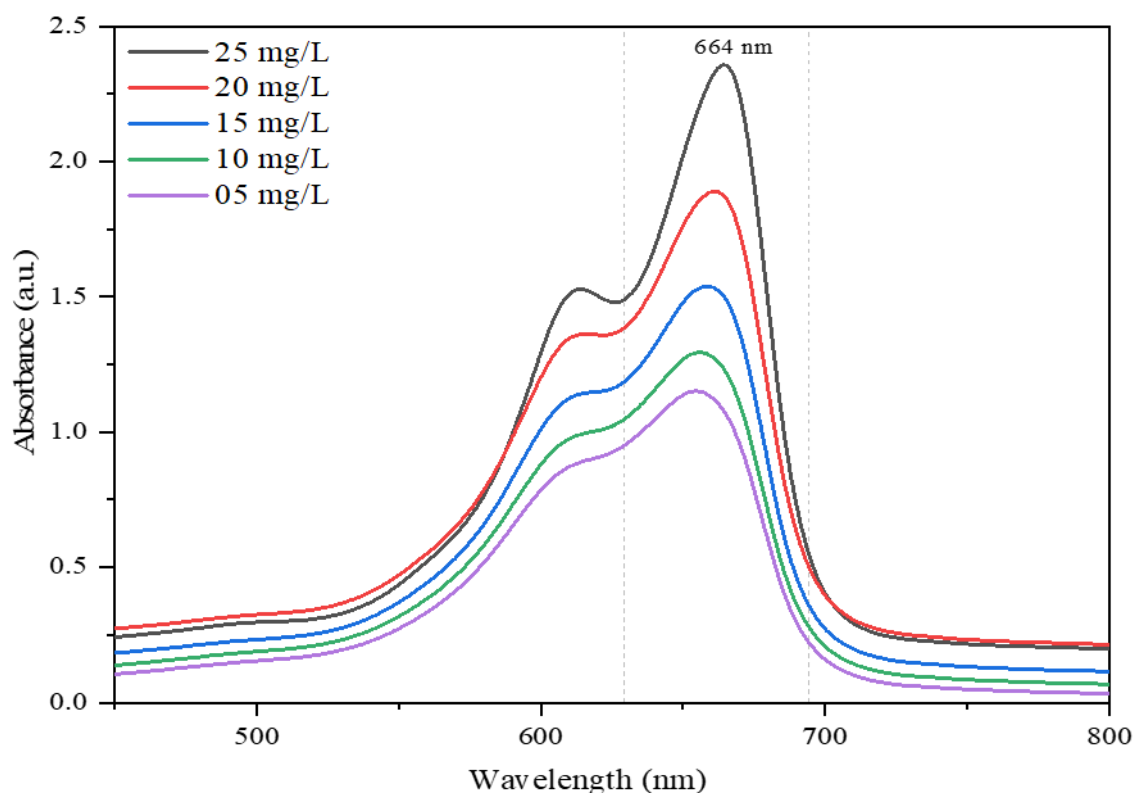
Figure 3.6**:** Absorption spectra of MB at different concentrations, 5, 10, 15, 20, and 25 ppm.

3.4.2 Photodegradation setup

The photoreaction was carried out using a handmade photoreactor as shown in Fig. 3.7. This photoreactor includes UV light (Xenon lamp, 250 W, 365 nm wavelength). The reactor's body is constructed from a wooden box to prevent hazardous light, which contains a magnetic stirrer, a Pyrex glass beaker (250 mL), and a fan. The University of Karbala has a College of Science, Department of Physics.
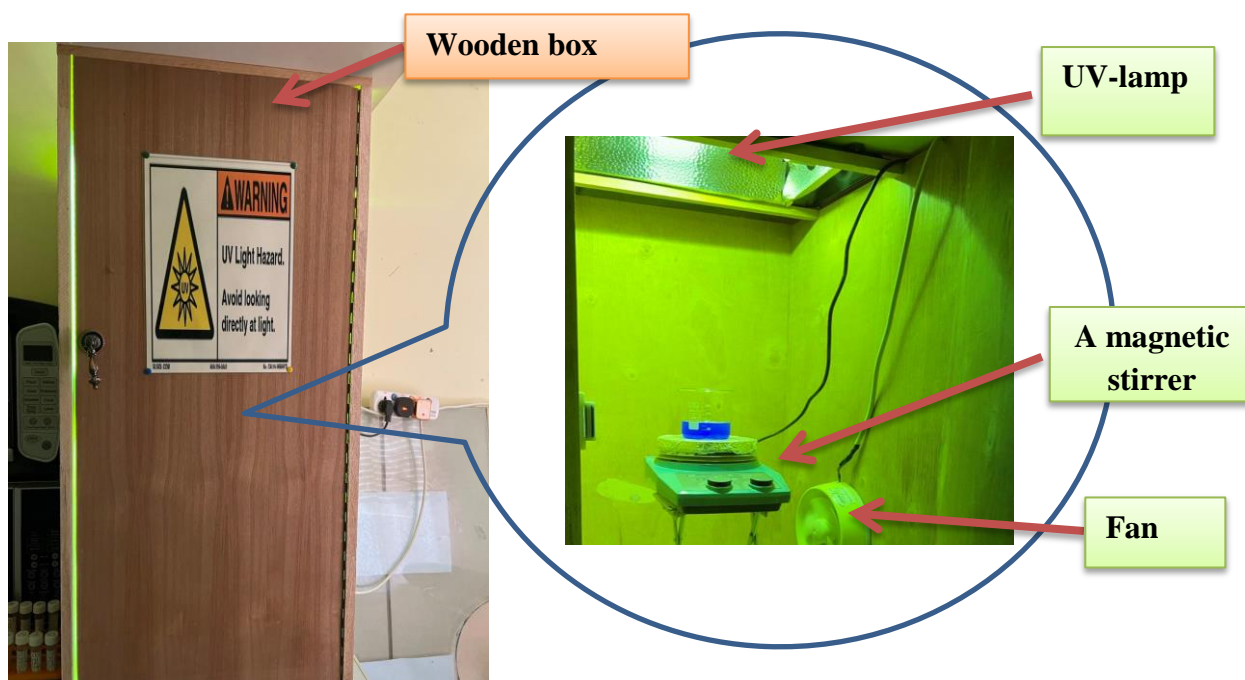
Figure 3.7: A photograph of the photocatalytic setup.

3.4.3   Photocatalytic studies

The influence of six different catalysts (TiO$_2$, X% Au /TiO$_2$) on the photocatalytic degradation of MB was investigated and studied. The examinations were carried out under similar conditions to compare the obtained results. The photodegradation properties of the prepared samples were evaluated in the presence of UV-Vis light to assess their ability to degrade MB dye. The degradation of MB dye was tracked by observing the gradual decline in the absorption peak at 664 nm in the UV-Vis absorption spectra as the reaction time increased. This particular absorption peak corresponds to MB and is indicative of its presence in the solution.

Initially, the addition of 15 mg of TiO$_2$ or X% Au /TiO$_2$ NPs as catalysts to a 100 mL MB with a concentration of 10 ppm and disperse the solid catalyst particles, the suspension was subjected to sonication for 10 min before using

UV light. To achieve adsorption-desorption equilibrium of the dye MB on the TiO$_2$ or X% Au /TiO$_2$ catalysts surface, and to minimize any errors arising from elementary adsorption, the solution was, then, placed in a dark room for at least 30 min. A preliminary sample, consisting of approximately 4 mL, was extracted from the solution after the dark adsorption phase to determine the concentration of the MB dye remaining in the solution, denoted as the primary concentration (C$_o$). The illumination process was then started and the samples were collected every 20 min for a total of 120 min. Finally, the solution was subjected to centrifugation at (4500 rpm for 10 min) to eliminate any suspended particulates, and the absorbance was determined using a Shimadzu-UV-Vis Spectrophotometer (UV-1900i).

Each sample's photodegradation efficiency (PDE) rate was determined using the equation [125]:

$$\boldsymbol{PDE}\ (\%) = \frac{(C_o - C_t)}{C_o} \times \boldsymbol{100}\%　\hspace{2cm} \textbf{(3.5)}$$

Where C_o and C_t are the MB concentrations before and after UV irradiation exposure respectively. C_t was calculated by drawing the calibration curve.

Chapter 4
Results and Discussion

4.1 Introduction

The results and discussion of the characteristics of pure TiO_2 and X% Au/TiO_2 NPs prepared using the Sol-Gel process are included in this chapter. Characterization investigations including XRD, XPS, FTIR, FESEM, EDX, TEM, BET, and UV-Vis spectroscopy are used to display and discuss the results. In addition, UV-Vis irradiation was used to investigate the photocatalytic activity of TiO_2 and X% Au/TiO_2 NPs.

4.2 XRD Results

XRD pattern exhibits distinct diffraction peaks corresponding to the crystallographic planes of polycrystalline Au and TiO_2 in both anatase and rutile phases. The XRD spectrum of the prepared samples is shown in Fig. 4.1. Peaks at $2\theta = 25.5°, 48.2°, 54.5°, 63.2°$ and $69.2°$ which assigned to (101), (200), (105), (204) and (116) crystal lattice planes correspond to TiO_2 in anatase phase, (JCPDS Card no. 002–0406), while the peaks at $2\theta = 27.8°$, $36.3°, 39.4°, 41.4°, 44.4°, 56.9°, 64.3°$, and $70.0°$ which were assigned to (110), (101), (200), (111), (210), (220), (310) and (112) revealed the rutile phase of TiO_2 (JCPDS Card no. 01-088–1173).

A peak at 2θ value of around $38.2°$ was observed revealing the existence of metallic Au which is assigned to (111) and this peak matches well with the face-centered cubic (FCC) Au NPs (JCPDS Card no. 004–0784). According to the standard, the Au metal has other peaks in the higher range of 2θ that may overlap with the peaks of TiO_2 or they may not have an obvious intensity due to its small amount [126].
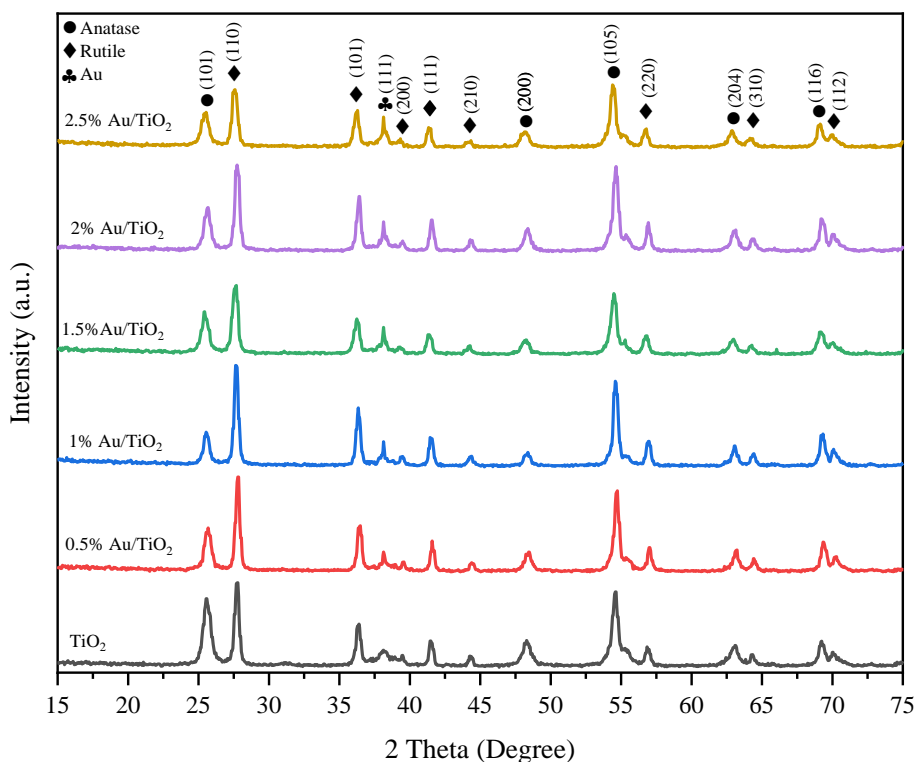
Figure 4.1**:** XRD patterns of TiO$_2$ NPs and X% Au/TiO$_2$ NPs.

Only this peak was observed for gold at $2\theta = 38.14°$, and the rest of the peaks may be overlapped with titanium peaks in other areas. Therefore, it was observed that the average crystal dimensions of the gold-plated samples were relatively reduced compared to the pure sample. It is worth noting that this phenomenon may be ascribed to the imposition of lattice strain, thereby offering a plausible explanation for the observed reduction in crystallite size among the Au-doped specimens [127].

The stronger peak resulting in the XRD test agrees with the (110) plane appearing at 27.76° of the diffraction patterns, indicating the formation of the TiO$_2$ tetragonal Rutile phase. The Debye-Scherrer formula was used to determine the samples' average crystallite size [128,129].

The determination of the ratio of the anatase to rutile phases can be achieved through the application of Spur's-Myers equation [130]. The equation (4.1), derived from analyzing areas under the highest normalized peak intensities of a diffraction pattern, enables the calculation of the anatase and rutile phases.

$$\% \ \boldsymbol{Rutile} = \frac{1}{1 + 0.8[\frac{I_A}{I_R}]} \qquad \textbf{(4.1)}$$

Where I_R areas are under the highest normalized peak intensities of the rutile phase, and I_A is areas under the highest normalized peak intensities of the anatase phase. The results of the ratio of anatase to rutile as well as the crystallite size for all samples are presented in Table (4.1). The highest anatase to rutile phase transformation occurred when 2.5% Au/TiO_2 was used as the dopant (ca. 39.36% anatase and 60.63% rutile). Thus, it can be concluded that doping Au into the TiO_2 structure promotes the transition from the anatase to the rutile phase.

Table **(4.1):** The ratio of rutile phase and anatase and crystallite size of the pure TiO_2 and X% Au/TiO_2 NPs samples

Sample	Phase ratio (%)		Crystallite size of TiO_2 (nm)	
	Anatase	Rutile	Anatase	Rutile
TiO_2	46.34	53.66	32.38	37.37
0.5% Au/TiO_2	44.85	55.15	32.39	35.5
1% Au/TiO_2	44.30	55.70	33.24	35.49
1.5% Au/TiO_2	41.49	58.51	28.96	28.65
2% Au/TiO_2	40.66	59.34	31.63	31.38
2.5% Au/TiO_2	39.36	60.64	33.97	26.37

Kim et al. [131] have indicated that factors such as synthesis method, calcination temperature, and metal-doped can influence the crystal phase formation of TiO_2. It has been recently reported that the mixed phases of TiO_2 are useful for reducing the recombination of photogeneration electrons and holes that would raise the photocatalytic activity [132]. However, the rutile phase is also preferred for a synthesized TiO_2 structure because it could be used to improve the photocatalysis activity of TiO_2 [133].

4.3 XPS Results

The XPS characterizations of representative pure TiO_2 and X% Au/TiO_2 NPs were performed. Usually, since carbon is typically present as adsorbed material on any sample, it serves as a convenient reference. Carbon element with a binding energy of C 1s = 284.8 eV is used as an internal standard. Shifted the binding energies of samples based on this value [134]. In Table (4.2), the peak position deviations from the standards for all samples of C 1s are listed.

Table **(4.2):** Peak position deviation from the standard for the samples.

Sample	Peak C1s BE (eV)	Energy shift (eV)
TiO_2	284.50	-0.30
0.5% Au/TiO_2	284.90	+0.10
1% Au/TiO_2	284.85	+0.05
1.5% Au/TiO_2	284.30	-0.50
2% Au/TiO_2	284.55	-0.25
2.5% Au/TiO_2	284.40	-0.40

Charge correction involves adjusting the binding energies along the axis by referencing the C1s peak at 284.8 eV, which, when corrected, also rectifies all other peaks within the same spectrum. In a separate spectrum, one simply needs to recall the C1s shift and apply it to other peaks [134].

Fig. 4.2 shows the surface survey XPS spectra of pure TiO_2 and X% Au/TiO_2 NPs. The C 1s binding energy is caused by a thin coating of carbonaceous material produced on the surface of most samples exposed to air. The survey spectra reveal two further peaks for Au/TiO_2 NPs in the region of 80- 90 eV.
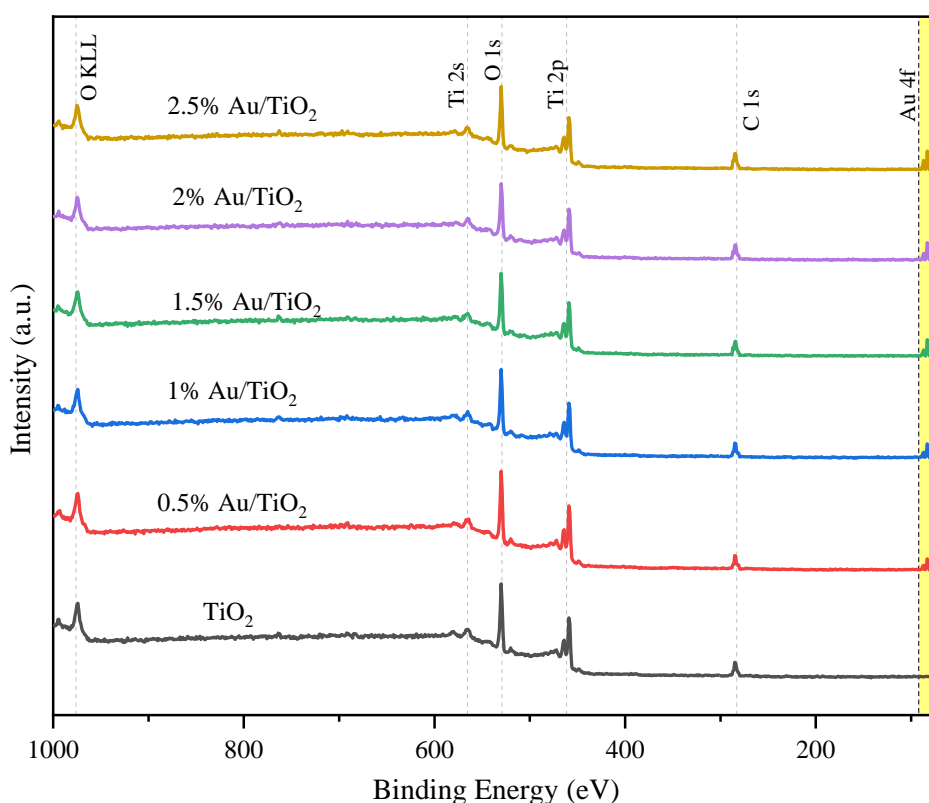
Figure 4.2**:** The surface survey XPS spectra of pure TiO_2 and X% Au /TiO_2 NPs.

Fig. 4.3 displays the Ti 2p region spectra of pure TiO_2 and X% Au/TiO_2 NPs. The two major photoelectron peaks of pure TiO_2 NPs at binding energies of 458.0 and 463.8 eV correspond to Ti $2p_{3/2}$ and $2p_{1/2}$, respectively. The Ti $2p_{3/2}$ and $2p_{1/2}$ peaks are found to be shifted to lower binding energy for X% Au/TiO_2 NPs in compassion with pure TiO_2.
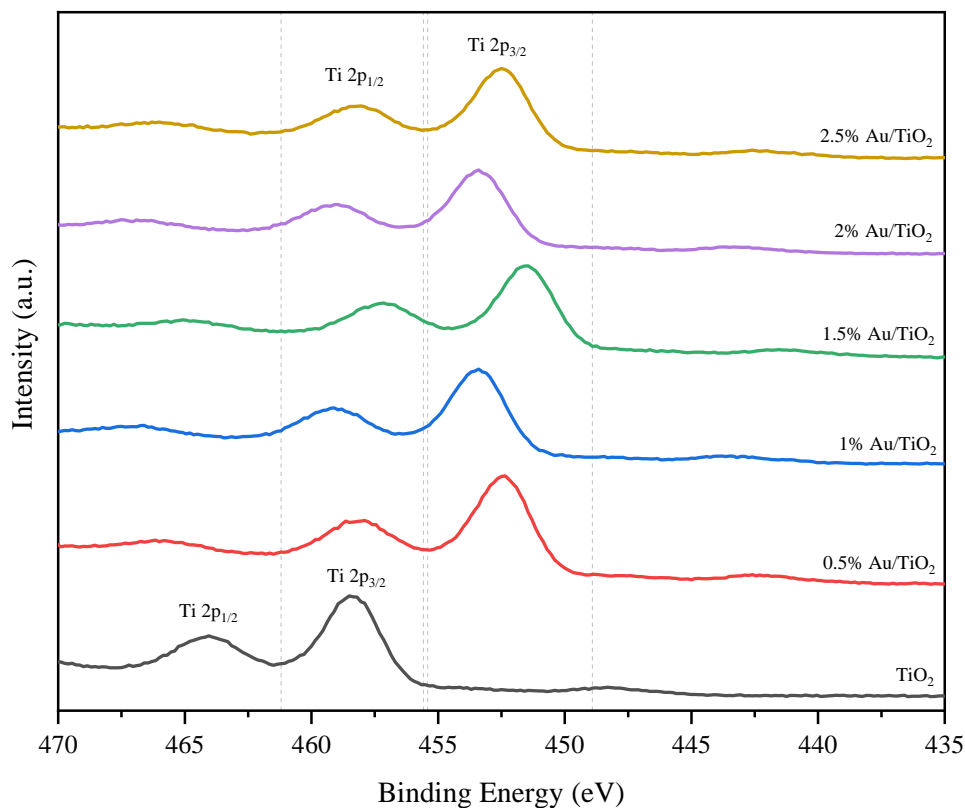
Figure 4.3: Ti 2p, XPS region spectra of pure TiO_2 and X% Au/TiO_2 NPs.

The shift in binding energies can be attributed to the change in the surface chemistry of TiO_2 in the X% Au/TiO_2 NPs. This is because the Fermi Energy (E_F) of Au is known to be lower (-5.5 eV) than that of TiO_2 (-4.4 eV) [135, 136]. The change in electronic properties is due to the intimate contact between TiO_2 and Au NPs [137]. Therefore, electrons drift from TiO_2 to Au in the case of X% Au/TiO_2, and this makes TiO_2 slightly positively charged, and thus Ti 2p peaks are at lower binding energy values for the X% Au/TiO_2 NPs. A marked shift in the binding energy is also observed for the O 1s of Au/TiO_2 NPs as compared with that of pure TiO_2 NPs, as shown in Fig. 4.4.
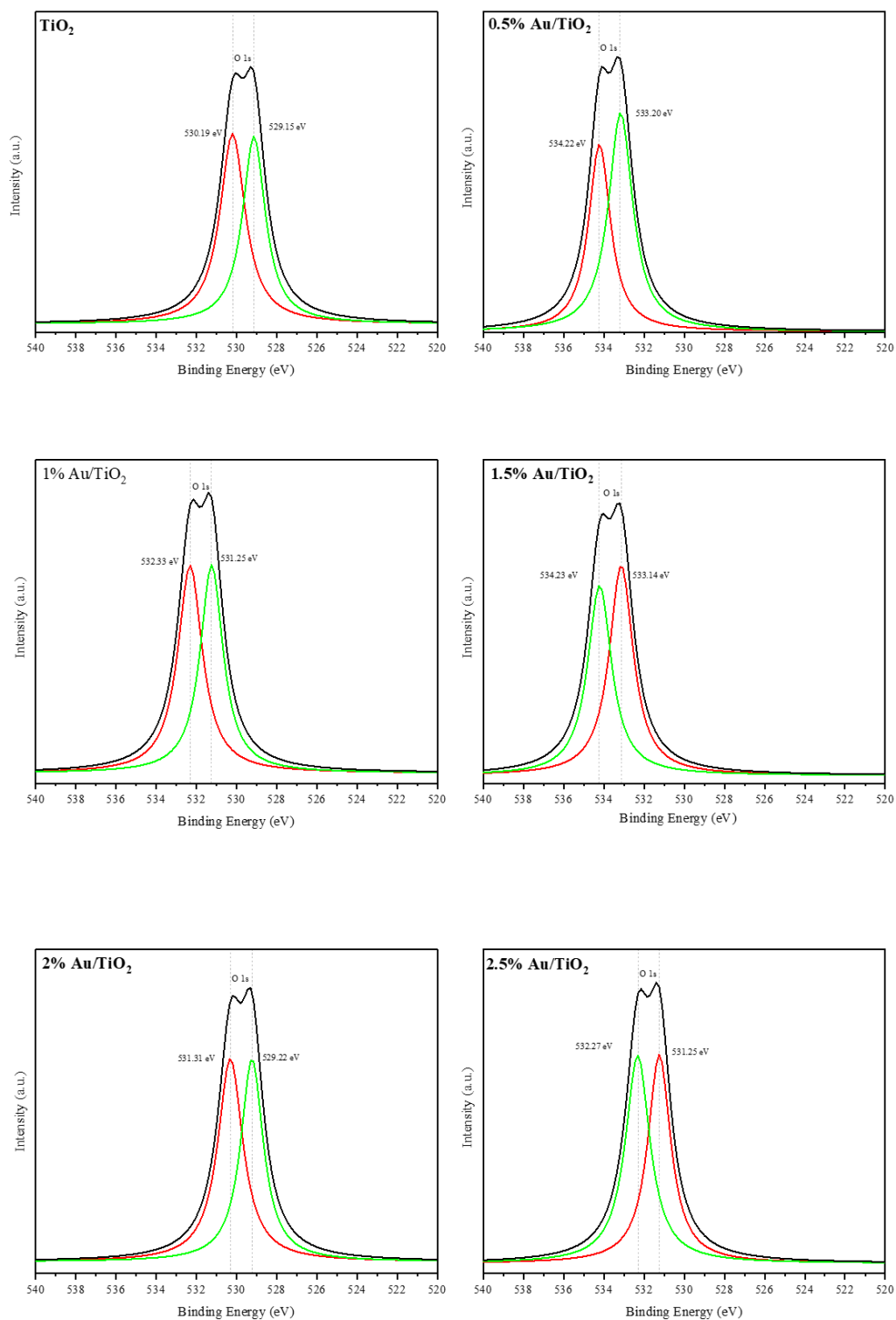
Figure 4.4: O 1s, XPS region spectra of TiO$_2$ and X% Au/TiO$_2$ NPs.

The O 1s feature of pure TiO$_2$ (Fig. 4.4 TiO$_2$) can be deconvoluted into two peaks, a peak at 529.15 eV and a peak at 530.19 eV, which are due to the lattice oxygen (LO) and surface-adsorbed oxygenated species (SO) respectively. These two O 1s peaks are found to be shifted to higher binding energy as shown in Fig. 4.4 for X% Au/TiO$_2$ [138]. The presence of LO and SO suggests the possibility of oxygen vacancies in the TiO$_2$ NPs. Oxygen vacancies can result in charge redistribution within the material, leading to a shift in the binding energy of the O 1s peaks towards higher energy.

The photoelectron peaks corresponding to the Au 4f$_{7/2}$ and 4f$_{5/2}$ orbitals were observed within the energy range of 82.02 to 89.35 eV for X% Au/TiO$_2$ NPs samples. This observation suggests the presence of metallic Au NPs in the X% Au/TiO$_2$ samples, as depicted in Fig. 4.5.
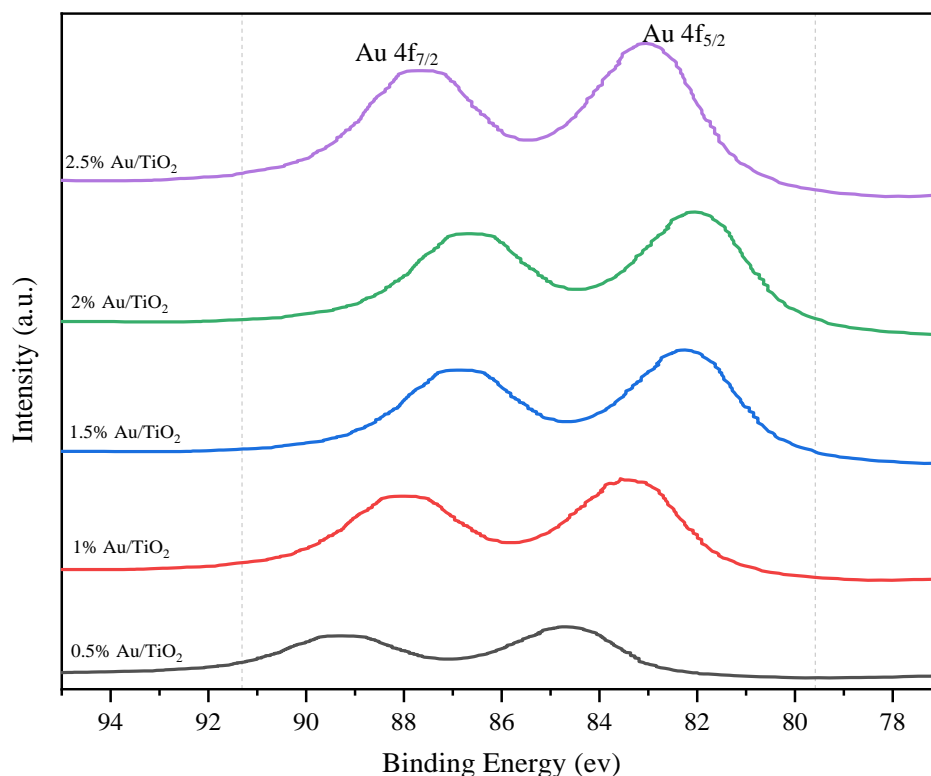
Figure 4.5**:** Au 4f, XPS regions spectra of X% Au/TiO$_2$ NPs.

The binding energy was slightly lower than that of the pure TiO_2 caused by an electron transfer from TiO_2 to Au NPs. The Au 4f signal showed a negative shift in binding energy for X% Au/TiO_2 and a continuous shift to lower binding energy with increasing Au content up to 2% Au/TiO_2, because Au NPs are dispersed on the TiO_2 surface, the electrons from the TiO_2 can transfer to the Au NPs, resulting in a change in the electronic structure of the around the Au NPs, leading to a negatively shifted binding energy in the Au 4f signal.

The shift of the Au $4f_{7/2}$ peak toward lower binding energy can be better explained by an initial state effect associated with electron transfer from Ti^{3+} surface defect sites to Au [139]. Table (4.3) summarizes the atomic percentage of the NPs samples as determined by XPS spectra.

Table **(4.3):** Atomic percentage of the nanoparticles.

Sample	C 1s (%)	Ti $2p_{3/2}$ (%)	O 1s (%)	Au $4f_{7/2}$ (%)
TiO_2	9.3	24.64	66.06	--
0.5% Au/TiO_2	9.0	26.6	64.1	0.3
1% Au/TiO_2	8.2	29.84	61.16	0.8
1.5% Au/TiO_2	7.24	25.70	65.81	1.25
2% Au/TiO_2	7.71	24.42	65.52	1.45
2.5% Au/TiO_2	6.72	24.20	67.07	2.01

4.4 FTIR Results

The FTIR spectrum recorded for the TiO_2 and X% Au/TiO_2 samples, is shown in Fig. 4.6. The absorption band observed at (3600 - 3750) cm^{-1} corresponds to the stretching vibration of the hydroxyl O-H group at (3735.21- 3420.10 cm^{-1}). This result indicates the physical absorption of water, suggesting the presence of moisture in the samples [140].

The band at 2355.12 cm^{-1} indicates the stretching vibration of bonded and non-bonded -O-H groups, resulting from the interaction of hydroxyl groups, and modes of the water molecules [141].

The enhanced intensity of the band at 2108.89 cm^{-1} suggests that most of the Au sites are covered by adsorbed oxygen. This could be attributed to the presence of very small-sized Au NPs in the X% Au/TiO$_2$ samples, as previous research has shown that Au particles smaller than 2 nm remain oxidized [142,143], The existence of this peak was not detected in the pure TiO$_2$ sample.
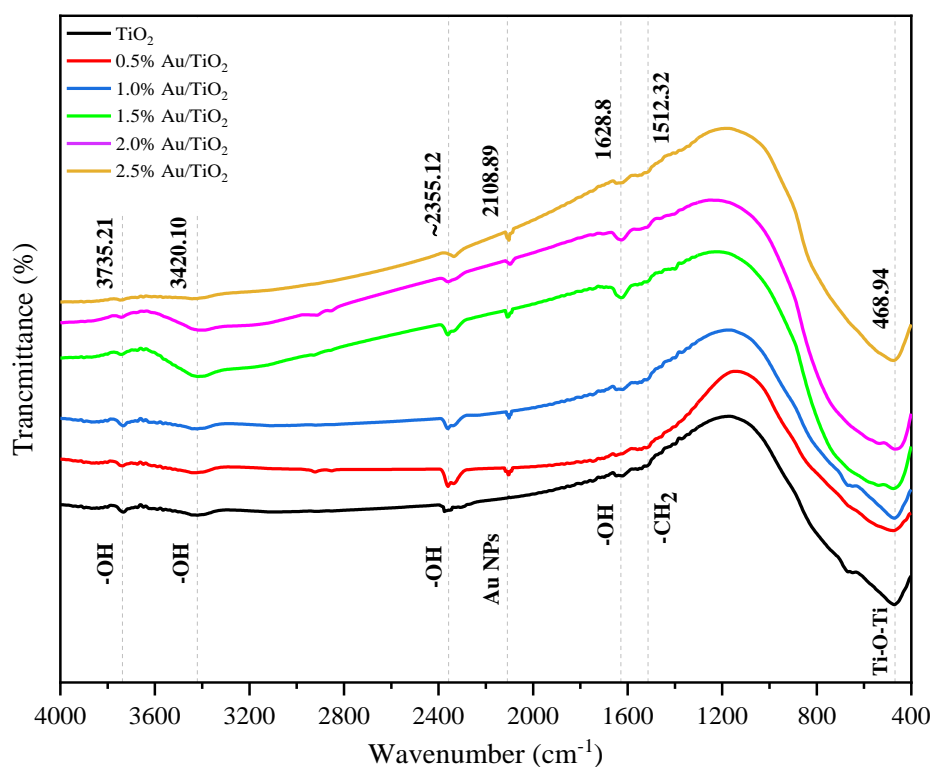
Figure 4.6: FTIR spectrum of the pure TiO$_2$ and X% Au/TiO$_2$ NPs.

Furthermore, a weak band is observed at 1628.80 cm^{-1}, corresponding to O-H bending groups resulting from chemically absorbed water in the solution

[144]. Another peak is detected at around 1512.32 cm^{-1}, characterized as the bending of CH$_2$ groups [145].

The peak at 468.94 cm^{-1} is observed which is attributed to Ti-O-Ti stretching vibrations in the anatase and rutile phase. This indicates the broad absorbance of TiO$_2$ due to the bending vibration of Ti-O stretching, resulting in the formation of Ti-O-Ti bridge stretching [146].

4.5 FESEM Results

Morphology of pure TiO$_2$ and X% Au/TiO$_2$ NPs was investigated using FESEM, EDX, and mapping techniques. The FESEM analysis results are shown in Fig. 4.7, with a scale of 200 nm.
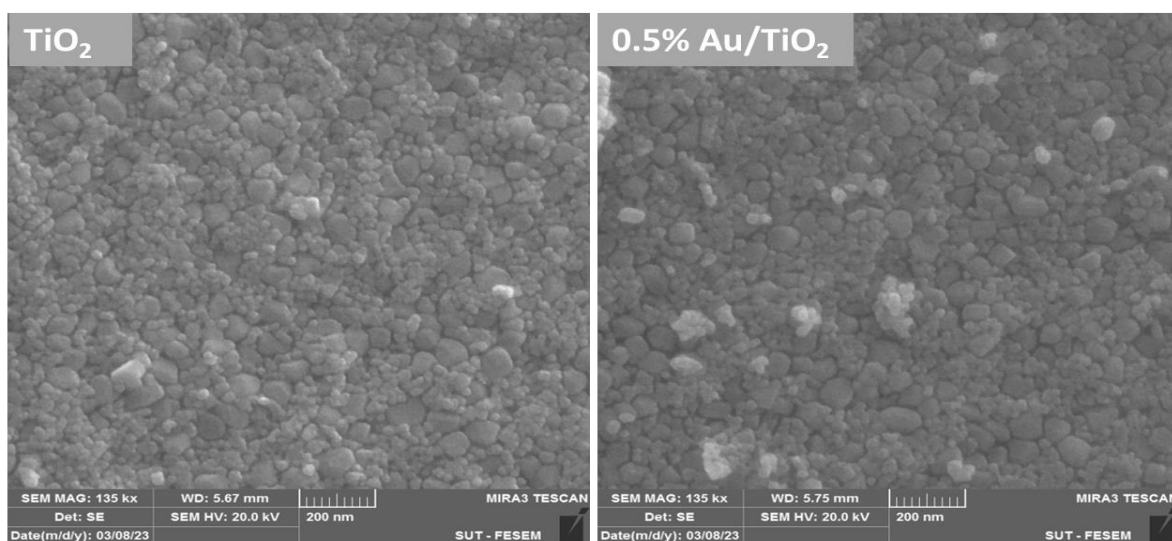
…Continued
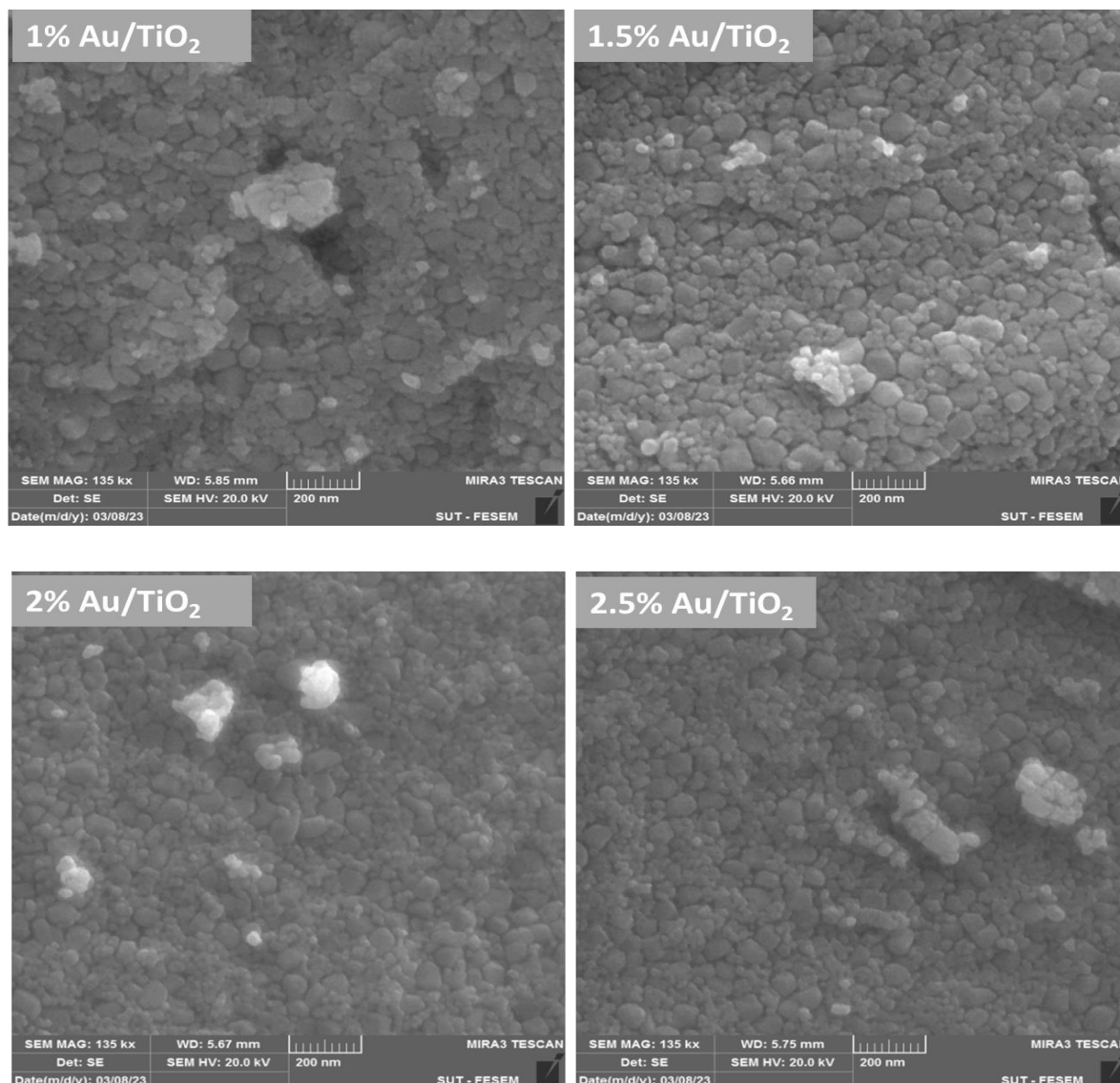
Figure 4.7**:** The FESEM images of TiO_2 and X% Au/TiO_2 NPs.

FESEM was used to examine the morphology of the prepared samples, as Fig. 4.7 illustrates. The structure of the prepared TiO_2 had agglomerated non-uniform spherical NPs, according to the results. The reason for the agglomeration was that TiO_2 was unstable in nanoparticle form and would tend to clump together until it reached a more stable state. The findings were in Au agreement with previously published research [147]. Nevertheless, it was not evident that Au NPs were of separate entities on the surface of X% Au/TiO_2

[148]. There were no discernible changes in the morphology of the TiO_2 and X% Au/TiO_2 samples.

The EDX mapping technique provided a comprehensive visualization of the elemental composition and spatial distribution of both TiO_2 and X% Au/TiO_2 NPs, as shown in Fig. 4.8. Notably, the Au NPs exhibit a significantly uniform dispersion across the surface of the TiO_2 material as shown in Fig. 4.8 (X% Au/TiO_2).
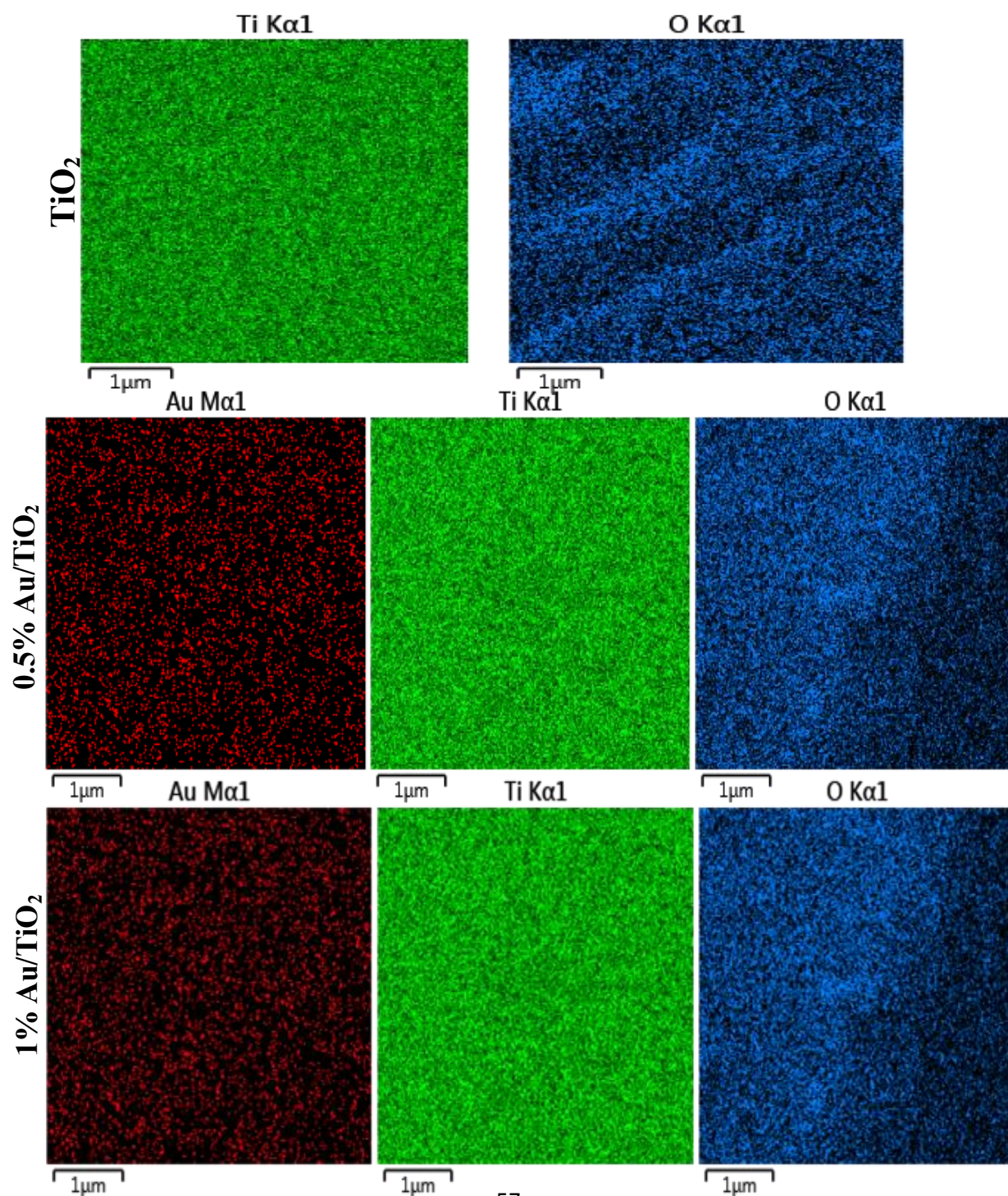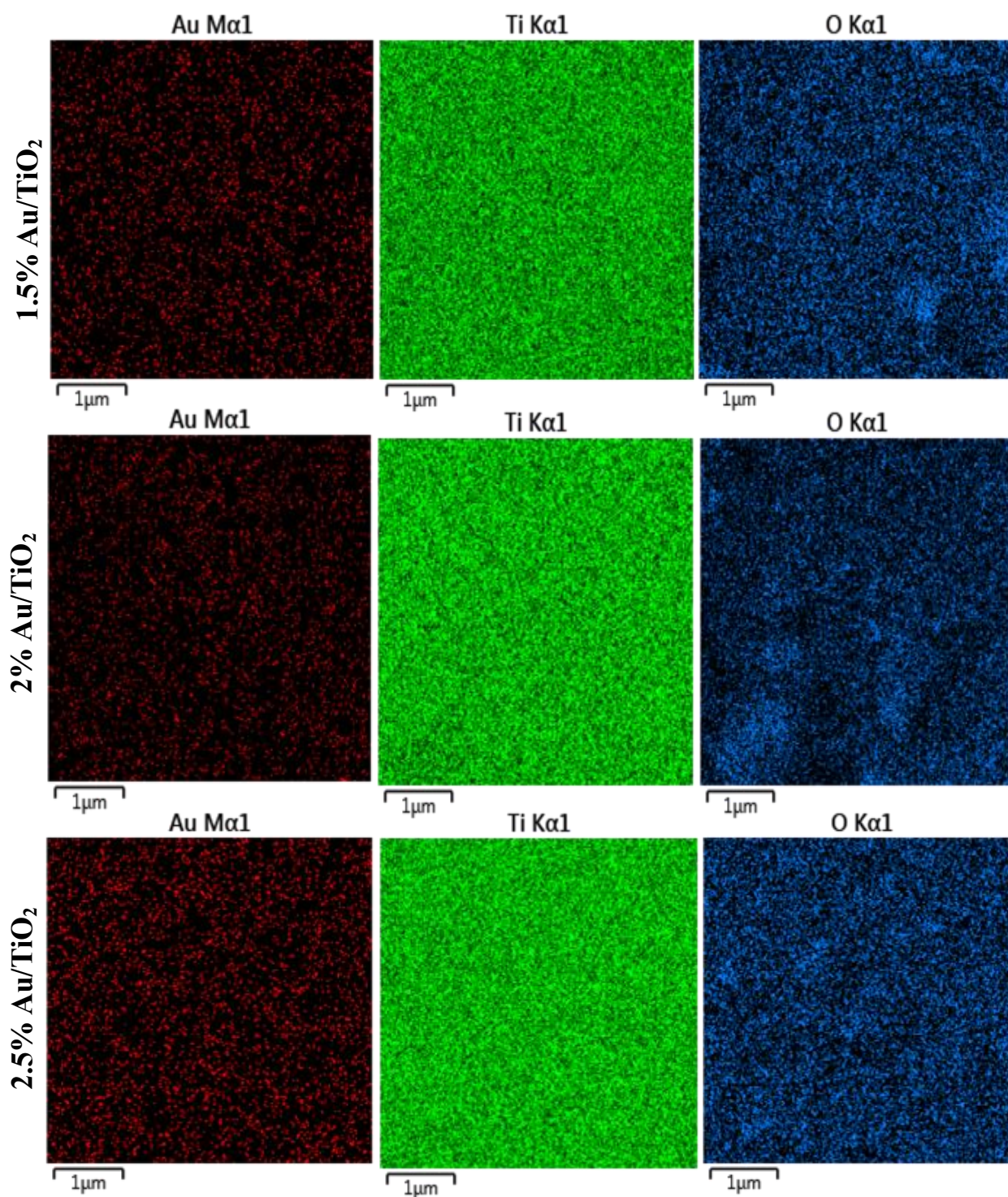
Figure 4.8**:** The EDX mapping of TiO_2 and X% Au/TiO_2 NPs.

The obtained data from the analysis confirmed the existence of Au metal on the surface of the catalyst as determined in Table 4.4. Weight percent (wt.

%) and Atomic (or molar) ratios (at. %) were determined and recorded for all six samples. Notably, the remaining samples exhibited slight contradictions between the observed percentage of Au within the sample structure and the expected value, as mentioned in Table (4.4).

Table **(4.4):** EDX analysis of the TiO_2 and X% Au/TiO_2 NPs.

Samples	wt. %			at. %		
	Au	Ti	O	Au	Ti	O
TiO₂	0	66.31	33.69	0	39.63	60.37
0.5% Au/TiO₂	0.32	59.66	40.02	0.21	33.37	66.42
1% Au/TiO₂	0.73	54.12	45.15	0.46	28.31	71.23
1.5% Au/TiO₂	1.11	60.02	38.87	0.9	34.04	65.06
2% Au/TiO₂	1.46	58.37	40.17	1.02	31.89	67.09
2.5% Au/TiO₂	2.01	63.17	34.82	1.12	36.42	62.46

4.6 TEM Results

TEM images were utilized to demonstrate the shape, particle size, and particle size distribution of pure TiO_2 and X% Au/TiO_2 NPs. Fig. 4.9 depicts the agglomerate of particles consisting of either single particles or clusters of particles, the TiO_2 and X% Au/TiO_2 NPs had an uneven form of produced NPs in a TEM image.

The morphology of TiO_2 remained same-like with the addition of Au, as illustrated in Fig. 4.9 where the Au NPs are evenly distributed over the surface of TiO_2.
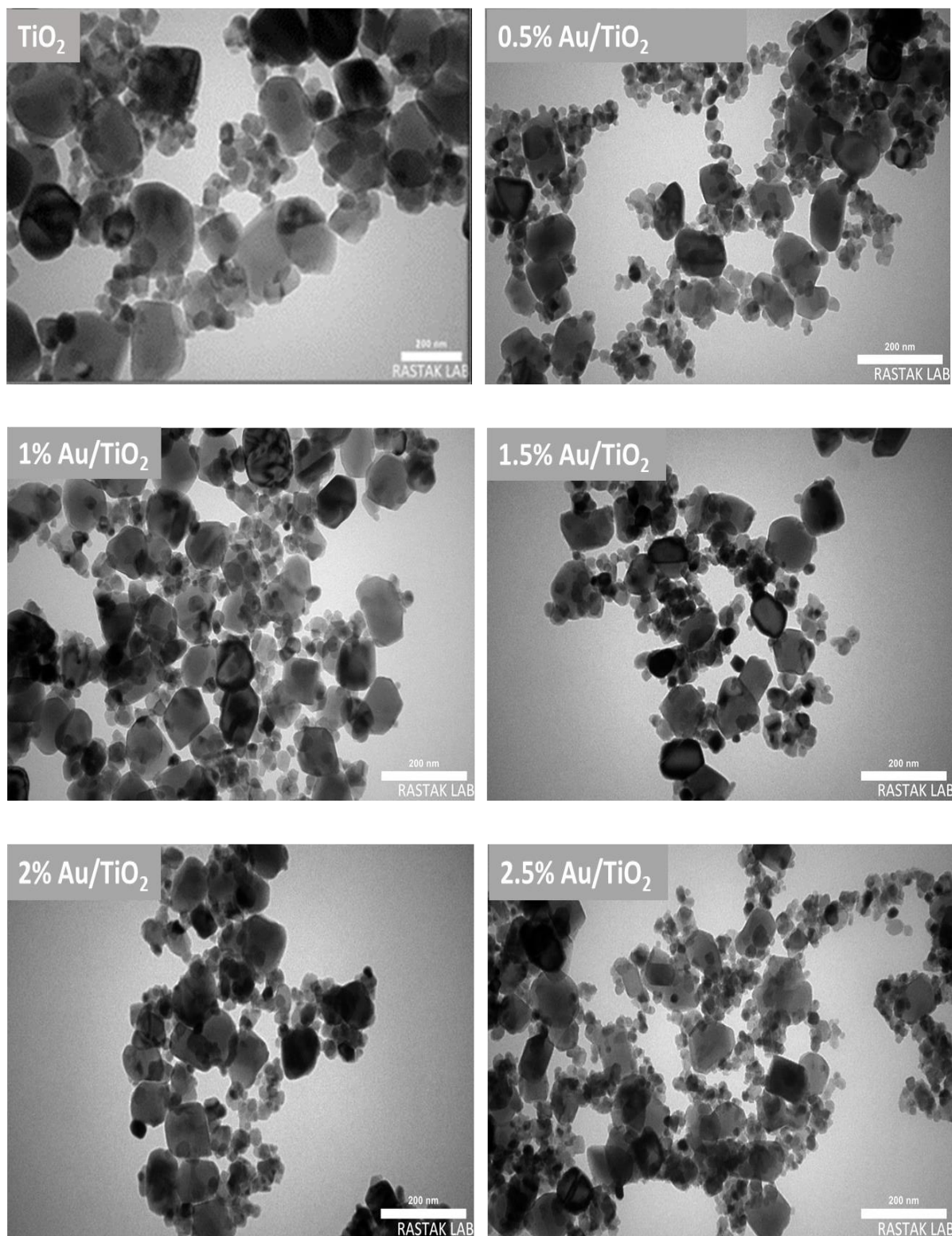
Figure 4.9: The TEM images of TiO_2 and X% Au/TiO_2 NPs.

Through the images TEM has been calculated the particle size and the distribution of TiO_2 and X% Au/TiO_2 samples are shown in the size

distribution histogram (Fig. 4.10). The particle sizes observed were 31 nm for TiO$_2$, 29 nm for 0.5% Au/TiO$_2$, 28 nm for 1% Au/TiO$_2$, 30 nm for 1.5% Au/TiO$_2$, 28 nm for 2% Au/TiO$_2$, and 29 nm for 2.5% Au/TiO$_2$, which is somewhat convergent with the anticipated crystallite size determined by the Scherrer equation.
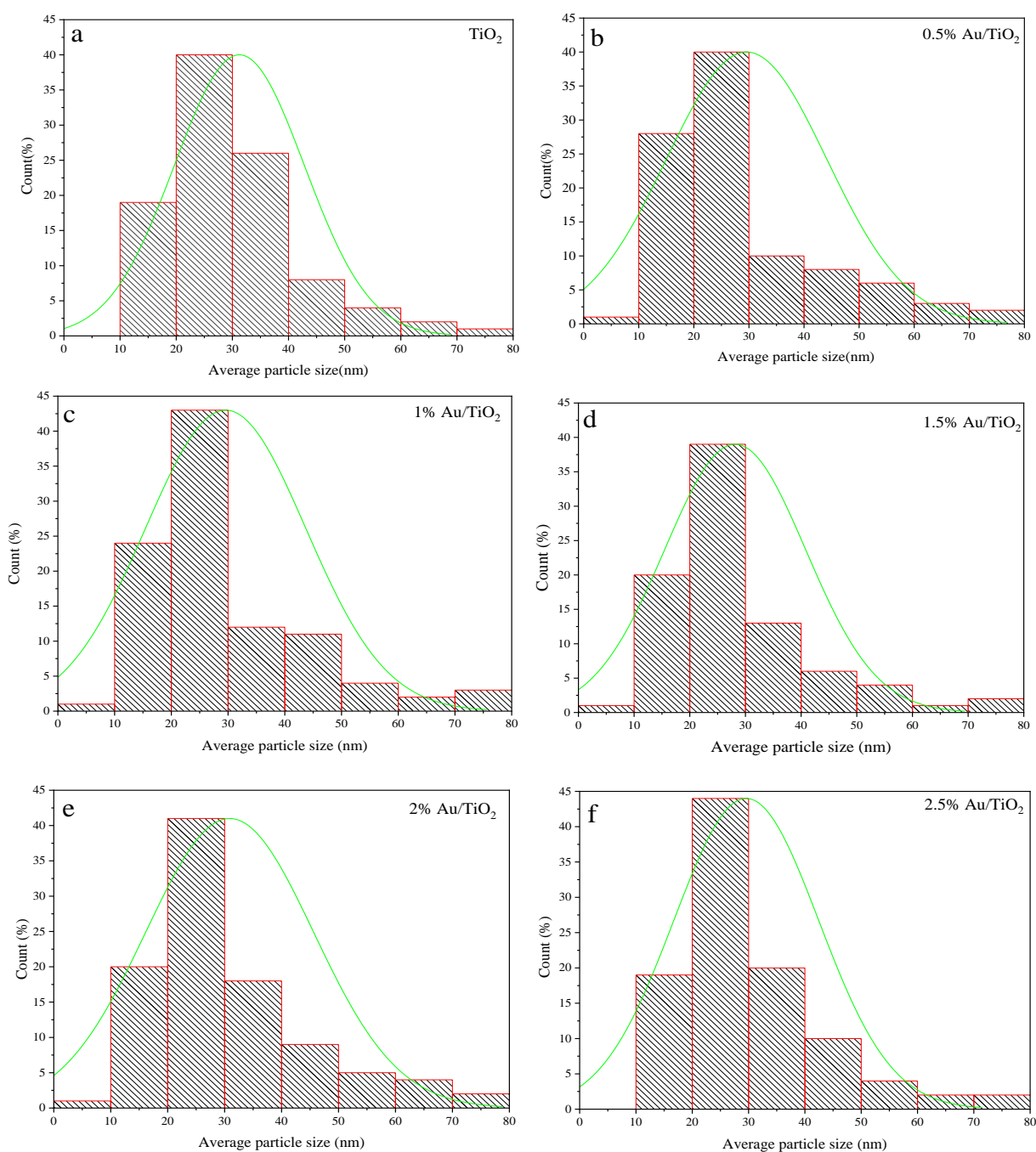
Figure 4.10: The size distribution histogram of TiO$_2$, and X% Au/TiO$_2$ NPs.

4.7 BET Results

The BET surface area and pours structure of TiO_2 and X% Au/TiO_2 NPs are investigated based on the N_2 adsorption-desorption isotherms measurement as shown in Fig. 4.11. TiO_2 and X% Au/TiO_2 give sorption isotherm with an H1 type Mesoporous materials composed of aggregated spheroidal particles commonly exhibit a type IV isotherm [149]. A type H1 hysteresis loop is often linked to uniform spheres arranged in a regular pattern, indicating a narrow pore size distribution [150].

The occurrence of monolayer adsorption on the inner surface becomes evident during the initial section of the isotherms at low relative pressure (low P/P_o). This is attributed to the transition from a fluid to a crystalline phase of the adsorbed N_2 [151].
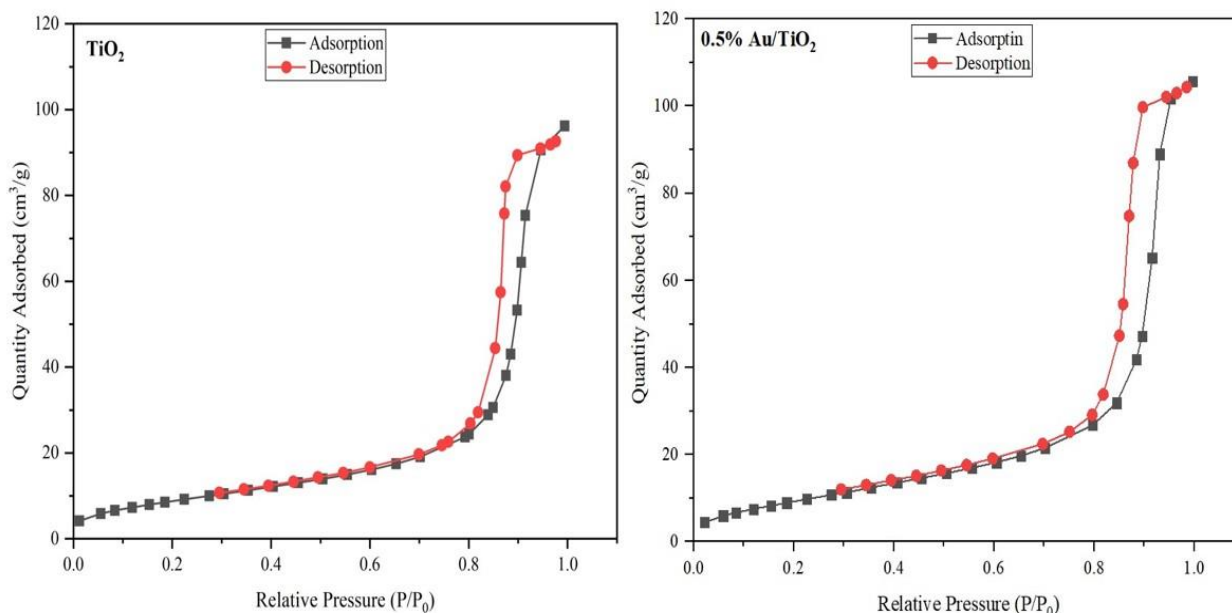
...Continued
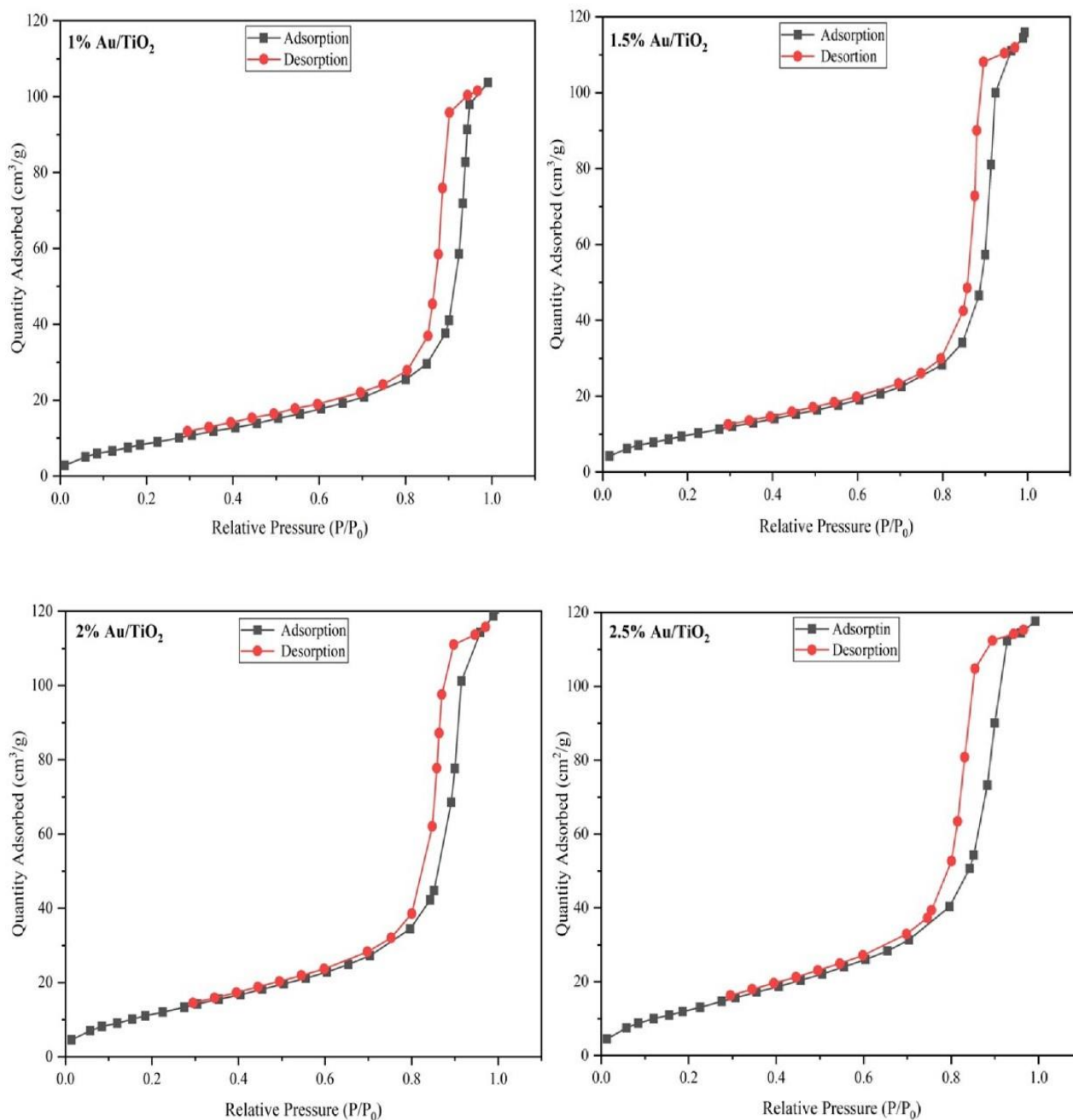
Figure 4.11: N_2 adsorption-desorption isotherm of TiO_2, and X% Au/TiO_2 NPs.

Capillary condensation becomes noticeable at elevated relative pressure (P/P_o), as indicated by the pronounced increase in adsorption volume observed

in the upper segment of isotherms once the pores have become saturated with N_2-liquid [152].

Table 4.5 provides a summary of the surface area, pore volume, and mean pore diameter of the samples examined. The BET surface area of TiO_2 (33.36 m^2/g) was found to be close to that of X% Au/TiO_2 NPs at lower Au concentrations but it showed a slight increase with higher Au percentage. This suggests that the addition of Au had a limited impact on the BET surface area of TiO_2, which is fairly acceptable when compared to other publications [153]. In contrast, the introduction of Au into TiO_2 NPs resulted in a greater mesoporous surface area and mesoporous volume compared to pure TiO_2. This increase can be attributed to the enhanced mesoporous caused by the Au doping which prevents TiO_2 NPs from clumping together [154]. Additionally, the BJH pore diameter gradually decreased with the addition of Au, indicating controlled crystal growth in the X% Au/TiO_2 NPs samples, this has been confirmed by the results of Tahir et al. [153].

Table **(4.5):** Summary of physiochemical characteristics of samples.

Sample	Surface area (S_{BET}) (m^2/g)	Total Pore Volume (cm^3/g)	Mean Pore Diameter (nm)
TiO_2	33.36	0.1481	17.75
0.5% Au/TiO_2	37.08	0.1625	17.52
1% Au/TiO_2	37.13	0.1602	17.25
1.5% Au/TiO_2	38.74	0.1772	16.29
2% Au/TiO_2	47.21	0.1846	15.63
2.5% Au/TiO_2	51.62	0.1816	14.07

4.8 UV-Vis Results

The UV–Vis absorption spectra of the TiO_2 and X% Au/TiO_2 NPs were recorded and are shown in Fig. 4.12. The TiO_2 shows trivial absorbance in the visible region because of the wide band gap (~3.2 eV).

TiO$_2$ effectively absorbs light in the range of 275 to 405 nm and efficiently reflects light due to its high refractive index [155]. These dual effects, absorption, and reflection, significantly enhance TiO$_2$ protective capabilities against ultraviolet rays [156].
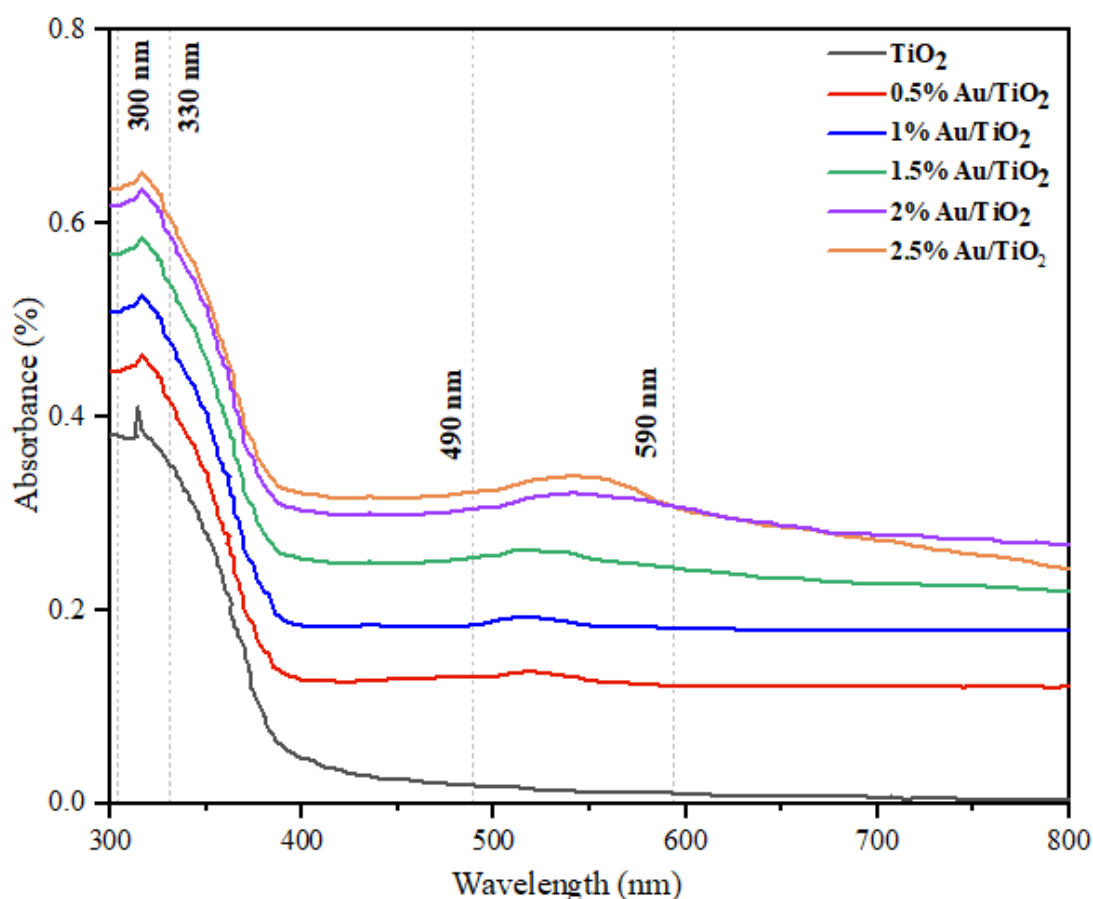
Figure 4.12: UV-Vis absorption spectrum of TiO$_2$ and X% Au/TiO$_2$ NPs.

Conspicuous absorption within the wavelength range of 300- 330 nm was discernible in all examined samples. Previous studies have substantiated the existence of a distinct peak at approximately 325 nm in pure TiO$_2$ [157]. Consequently, by introducing varying quantities of Au into the TiO$_2$ catalyst, the predictable modulation of the absorption has been demonstrated.

Following the doping of Au NPs, an increase in absorption for X% Au/TiO$_2$ NPs was observed (as seen in Fig. 4.12). As a result, it can be

concluded that Au loading can effectively extend TiO_2 absorption edge from UV to visible range via surface plasmon resonance and band gap reduction. Additionally, a distinct absorption wide peak emerged within the 490 nm to 590 nm range, aligning with the inherent absorption peak of Au the light-capturing effect created by the surface plasmon resonance of the Au NPs [95]. Increasing the Au content in the catalyst led to a proportional increase in light absorption,

4.8.1 Band gap energy and Tauc plot

The Tauc plot analysis used to calculate the band gap energy (Eg), is shown in Fig. 4.13, specifically for a direct band gap semiconductor. By closely examining the Tauc plot, one can observe the change in the band-gap energy from the ultraviolet (UV) region for pure TiO_2 to the visible region for X% Au/TiO_2.
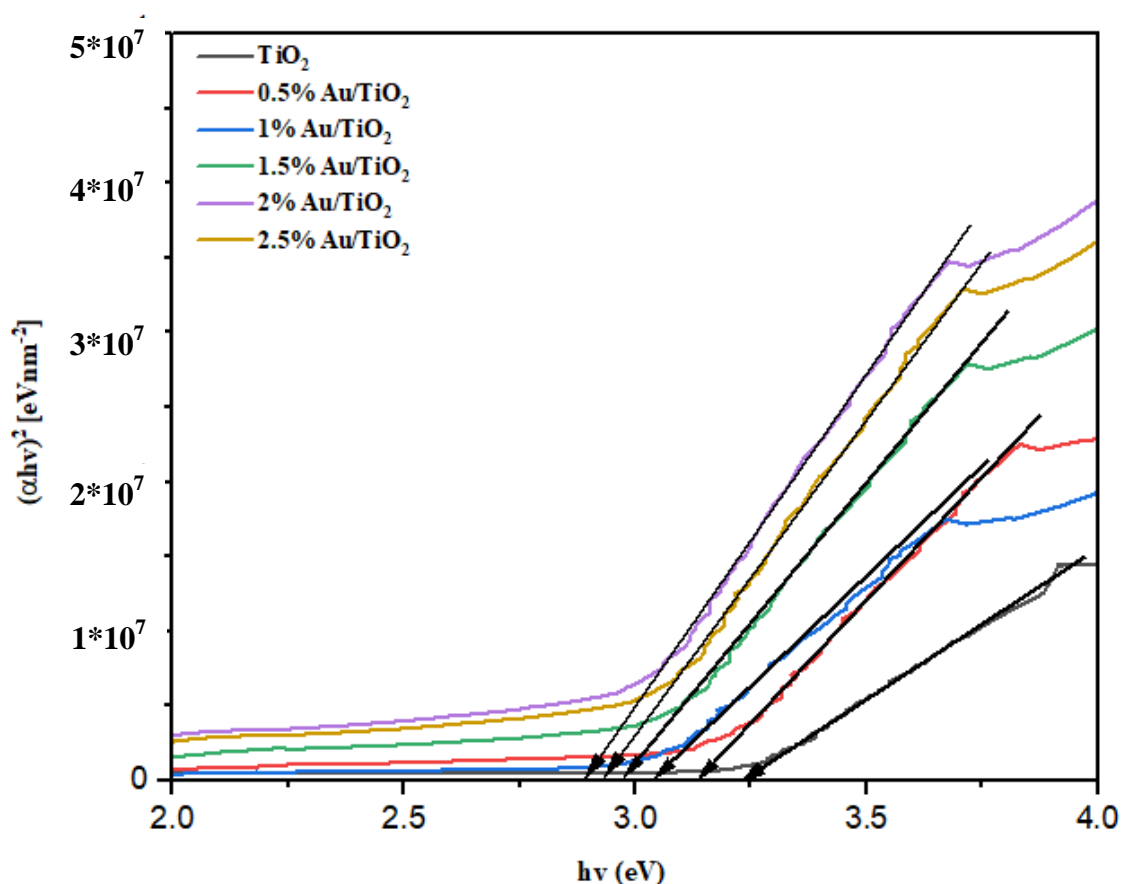
Figure 4.13: Tauc plots of the pure TiO_2 and X% Au/TiO_2 NPs.

The calculated band gap energy of pure TiO_2 is 3.24 eV, which aligns well with the theoretical value. However, as the amount of Au doping increases, there appears a decreasing trend in the band gap energy, as shows in Table (4.6).

The decrease in Eg value is a result of the properties of free electrons in the conduction band (CB), indicating structural changes in the TiO_2 matrix upon loading of Au NPs onto TiO_2. This leads to the creation of a metal-semiconductor Schottky junction between Au and TiO_2 [158].

Previous reports have shown that when metal contacts a semiconductor, there is a shift in the fermi level of the metal to higher energy. This shift in fermi level, closer to the CB of the semiconductor, increases the lifetime of

photo-generated electrons and reduces the recombination of charge carriers, thereby enhancing the photocatalysis process on the surface [159].

Table **(4.6):** Band gaps of pure TiO_2 and X% Au/TiO_2 NPs.

Samples	Band gaps (eV)
TiO_2	3.24
0.5% Au/TiO_2	3.14
1% Au/TiO_2	3.02
1.5% Au/TiO_2	2.98
2% Au/TiO_2	2.90
2.5% Au/TiO_2	2.94

4.9 Photocatalytic Performance

4.9.1 Photocatalytic degradation of methylene blue

This section focuses on the investigation and study conducted to examine the impact of six distinct catalysts (TiO_2, 0.5% Au/TiO_2, 1% Au/TiO_2, 1.5% Au/TiO_2, 2% Au/TiO_2, and 2.5% Au/TiO_2) on the photocatalytic degradation of MB. The experiments were conducted under identical conditions to compare their respective performances.

4.9.2 Effect of catalyst dose of TiO_2 NPs on the MB dye removal efficiency

This study aimed to examine the impact of varying adsorbent quantities on the photocatalytic degradation of MB dye, utilizing a TiO_2 catalyst. The dosage of the catalyst exhibited a significant impact on the degradation rate. However, the quantity of catalyst demonstrated both positive and negative effects on the photodecomposition rate. The initial reaction rates were observed to be directly proportional to the concentration of the catalyst, thus implying a heterogeneous regime [160].

To determine the optimal dosage of the catalyst, various quantities of the TiO_2 catalyst were measured and subsequently evaluated for their

photocatalytic efficacy under the same experimental conditions. Thus, varying amounts of 5, 10, 15, 20, and 25 mg of adsorbent were employed as shown in Figs. 4.14- 4.18. Subsequently, each of these catalyst doses underwent photocatalytic testing using identical operating conditions, including a concentration of MB dye at 10 ppm, a solution volume of 100 mL, and exposure to UV light irradiation for 120 min. The remaining concentration of MB dye in the supernatant was quantified by measuring its absorbance using UV-visible spectroscopy.

Figure 4.14**:** UV–Vis spectra of MB degradation, catalysts dose = 5 mg of TiO_2, versus irradiation time for MB degradation.

Figure 4.15: UV–Vis spectra of MB degradation, catalysts dose = 10 mg of TiO$_2$, versus irradiation time for MB degradation.

Figure 4.16: UV–Vis spectra of MB degradation, catalysts dose = 15 mg of TiO$_2$, versus irradiation time for MB degradation.

Figure 4.17: UV–Vis spectra of MB degradation, catalysts dose = 20 mg of TiO$_2$, versus irradiation time for MB degradation.

Figure 4.18: UV–Vis spectra of MB degradation, catalysts dose = 25 mg of TiO$_2$, versus irradiation time for MB degradation.

The degradation efficiency using eq. (3.5) of MB exhibits a gradual increase as the concentration of the catalyst is raised from 5 to 10 mg, with corresponding values of 36.22% and 57.41%, for 120 min of irradiation respectively [161], as shown in Fig 4.19. This trend can be attributed to the completed adsorption of organic molecules and the greater availability of active sites for photon absorption resulting from a higher catalyst dose. Furthermore, the degradation efficiency of MB is further enhanced from 57.41% to 68.62% with an increase in catalyst dose from 10 mg to 15 mg, respectively. However, it is important to note that employing a catalyst dose exceeding 15 mg does not lead to an improvement in photo-degradation efficiency. This may be attributed to the occurrence of elevated solution turbidity as a consequence of the higher catalyst dosage, subsequently reducing light penetration due to the scattering effect [162]. Additionally, the aggregation of particles at higher catalyst doses [163] can result in a reduction in the available active surface for MB adsorption and light radiation.
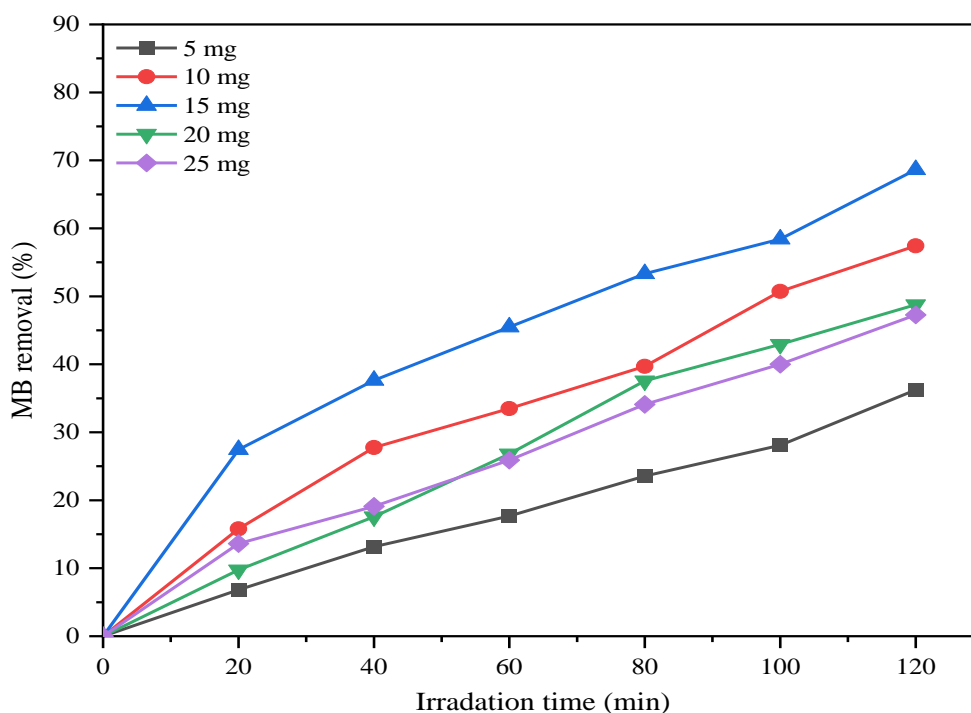
Figure 4.19: Effect of dose of TiO_2 on the degradation of MB dye, as a function of UV light irradiation time.

Thus, the catalytic dose of 15 mg is considered as the best catalytic dose and other catalysts were investigated with different doses. Table (4.7) shows the percent of degradation obtained after the photocatalytic reaction with different TiO_2 NPs dosages used in this study.

Table **(4.6):** Degradation percent of MB dye solutions with different TiO_2 dosages after 120 min under UV irradiation.

TiO_2 dose (mg)	PDE (%)
5	36.22

10	57.41
15	68.62
20	48.78
25	47.27

4.9.3 Effect of catalyst dose of 15 mg of (TiO$_2$ and X% Au/TiO$_2$) NPs on the MB dye removal efficiency

The time-dependent UV–Vis spectra of MB in the presence of the synthesized pure TiO$_2$, 0.5% Au/TiO$_2$, 1% Au/TiO$_2$, 1.5% Au/TiO$_2$, 2% Au/TiO$_2$, and 2.5% Au/TiO$_2$ nanocomposites under UV-light irradiation were shown in Figs. 4.20- 4.25, respectively. The results showed that as the time increased, the absorption decreased for all samples. The nanoparticle with 2% Au/TiO$_2$ had the highest reduction in absorption, while pure TiO$_2$ had the lowest reduction after 120 min of UV light exposure. Because the interaction of the dye molecule increased with the surface of the photocatalyst. Therefore, the photodegradation efficiency of the photocatalyst was increased.
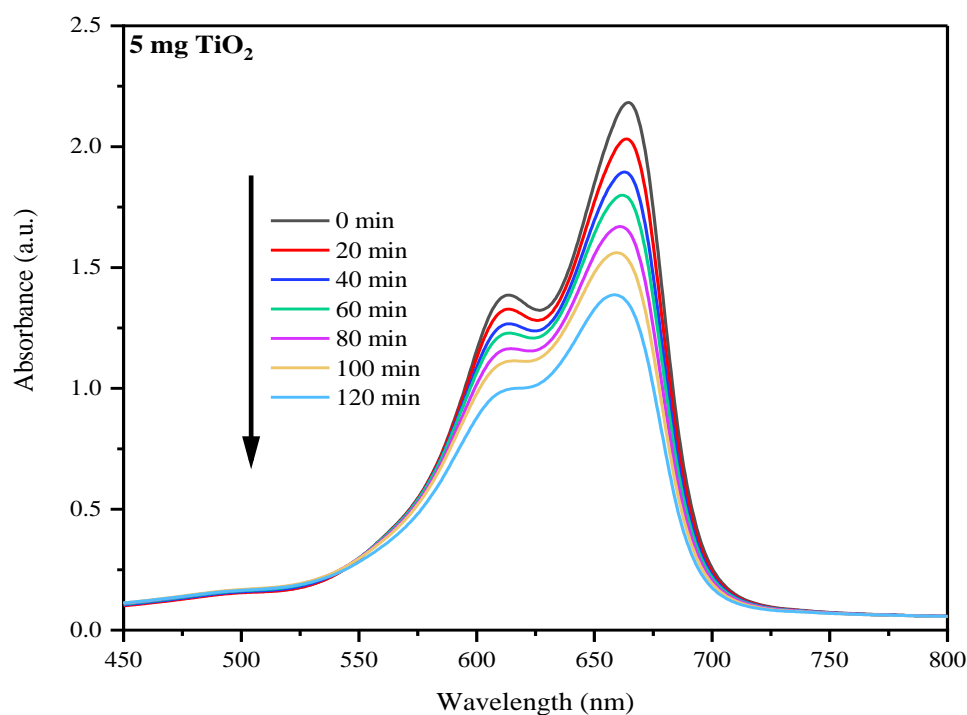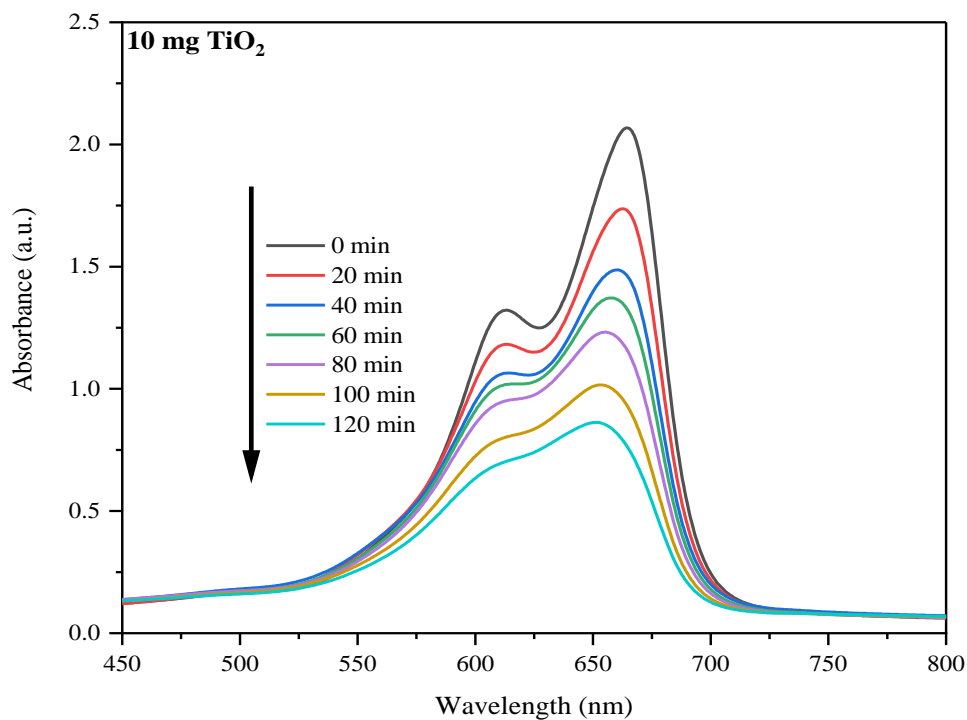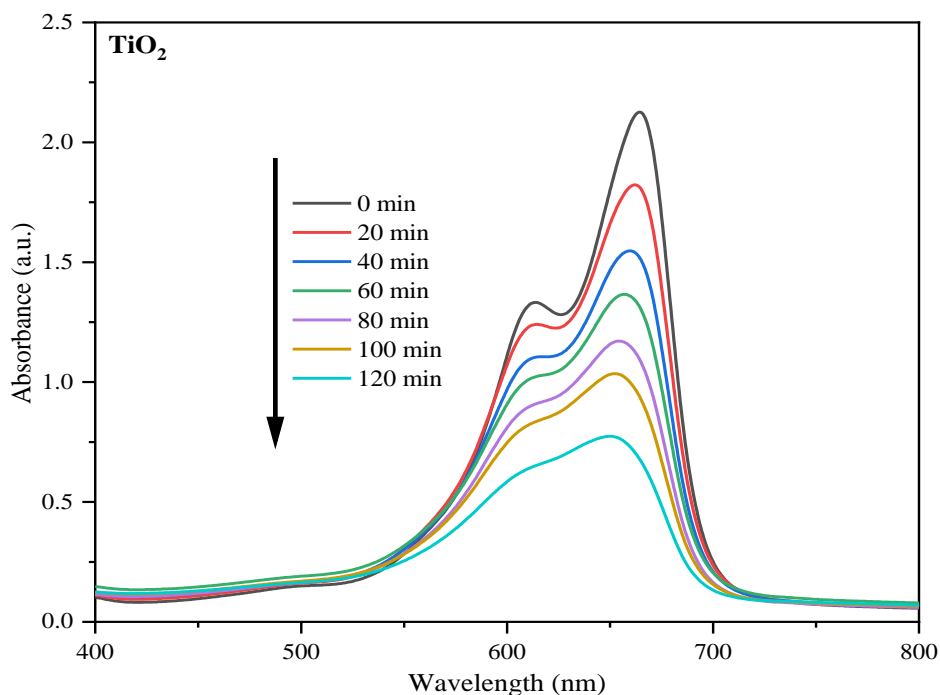
Figure 4.20: UV–Vis spectra of MB degradation, catalysts dose = 15 mg of pure TiO$_2$, versus irradiation time for MB degradation.
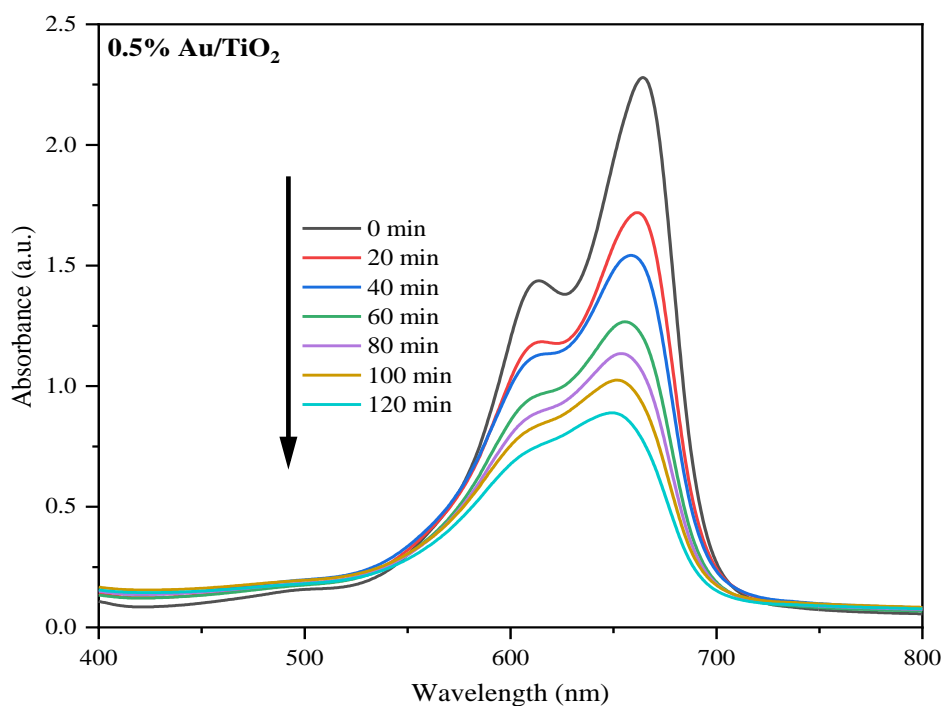
Figure 4.21: UV–Vis spectra of MB degradation, catalysts dose = 15 mg of 0.5% Au/TiO$_2$, versus irradiation time for MB degradation.
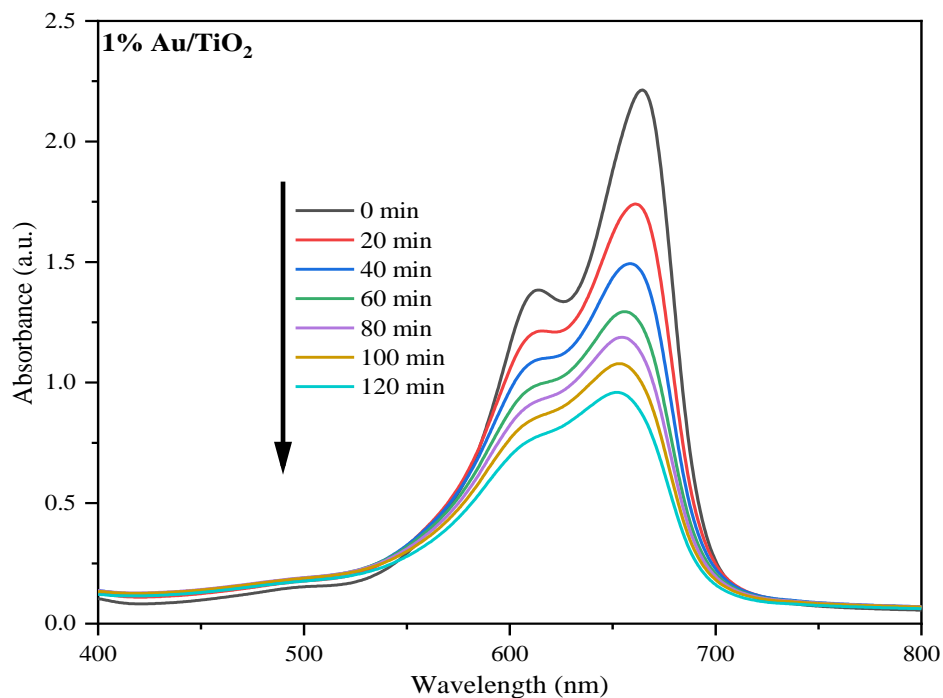
Figure 4.22: UV−Vis spectra of MB degradation, catalysts dose = 15 mg of 1% Au/TiO$_2$, versus irradiation time for MB degradation.
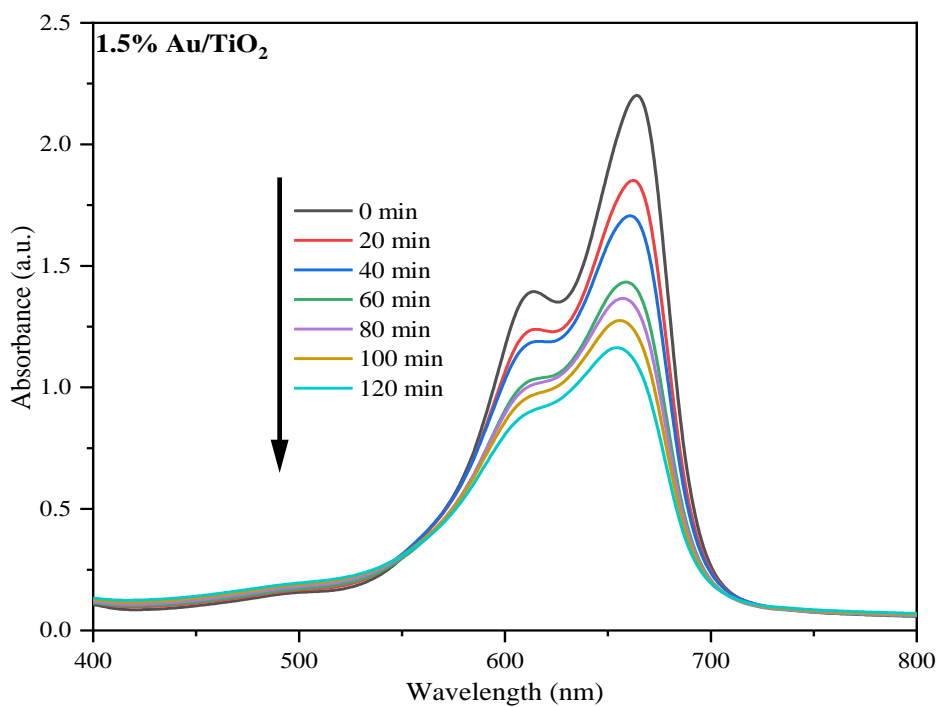
Figure 4.23: UV−Vis spectra of MB degradation, catalysts dose = 15 mg of 1.5% Au/TiO$_2$, versus irradiation time for MB degradation.
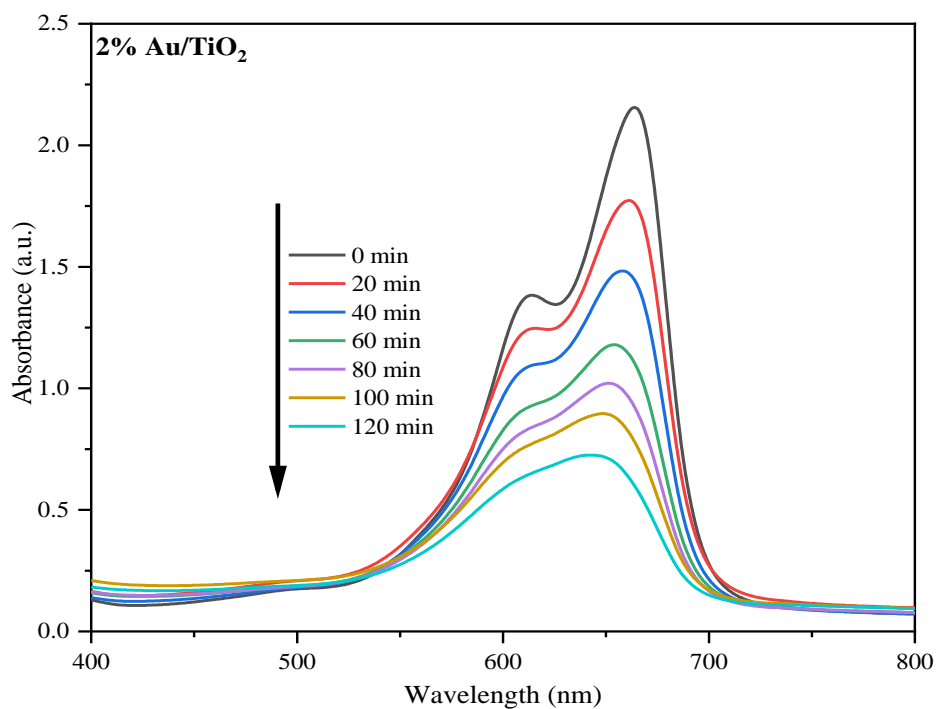
Figure 4.24: UV–Vis spectra of MB degradation, catalysts dose = 15 mg of 2% Au/TiO₂, versus irradiation time for MB degradation.
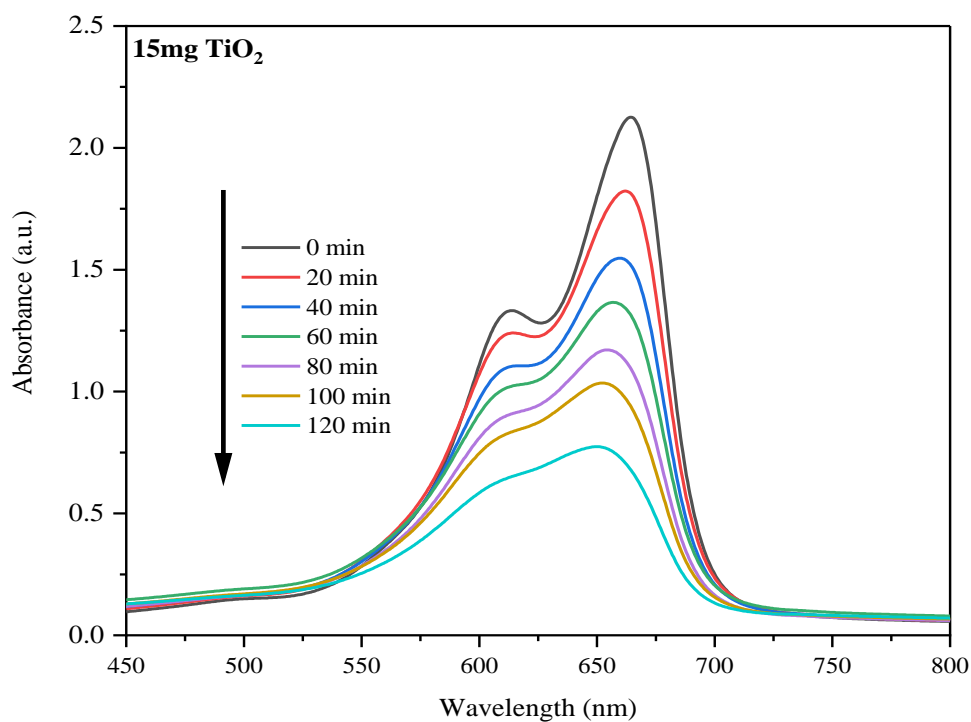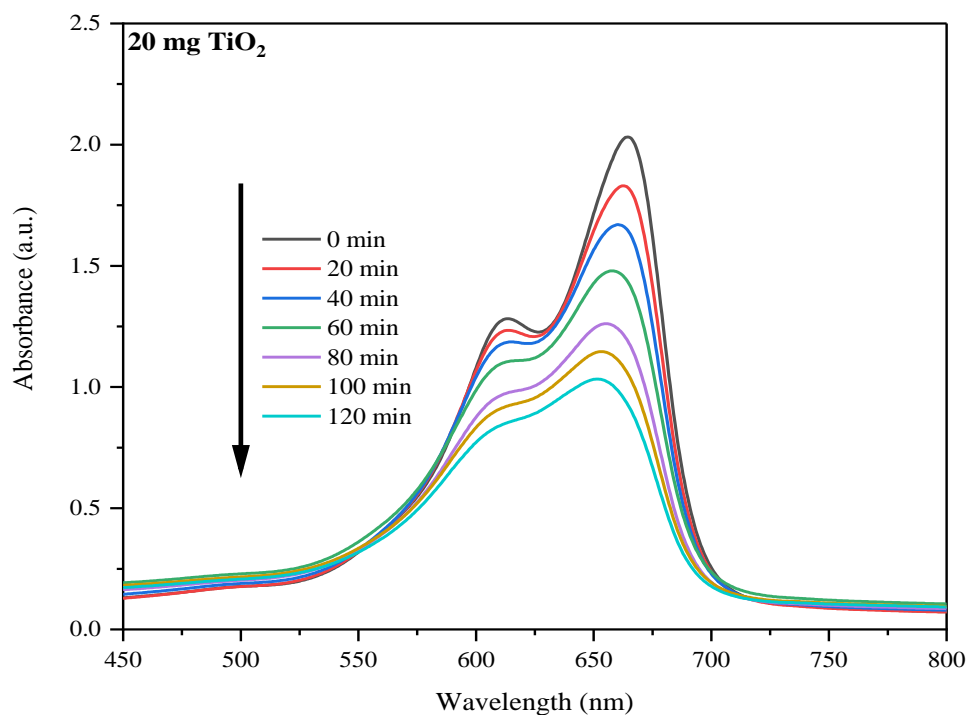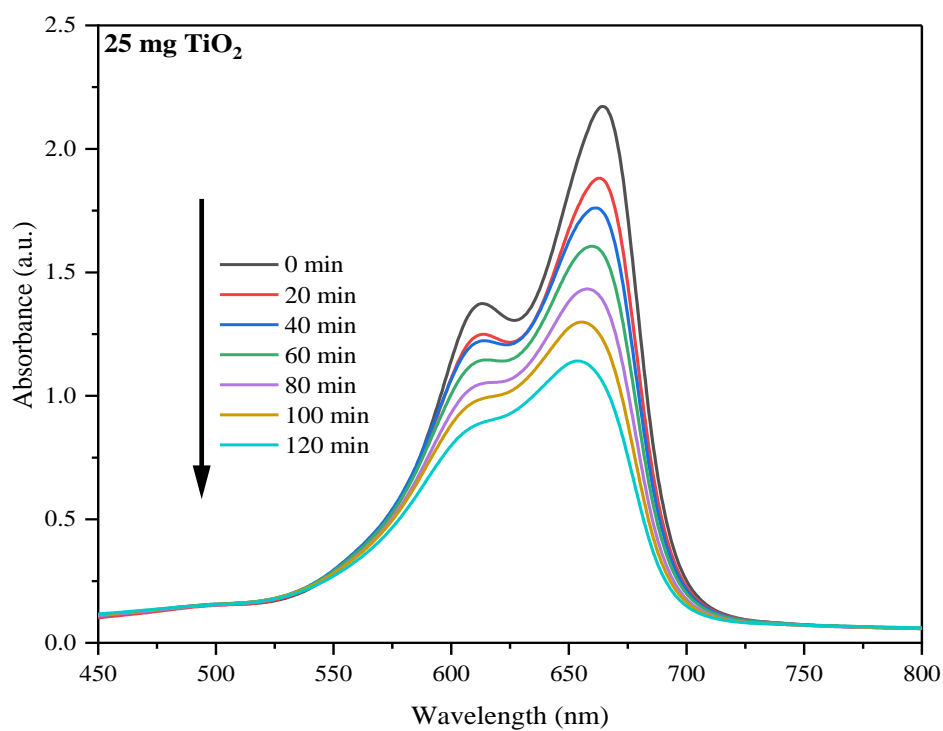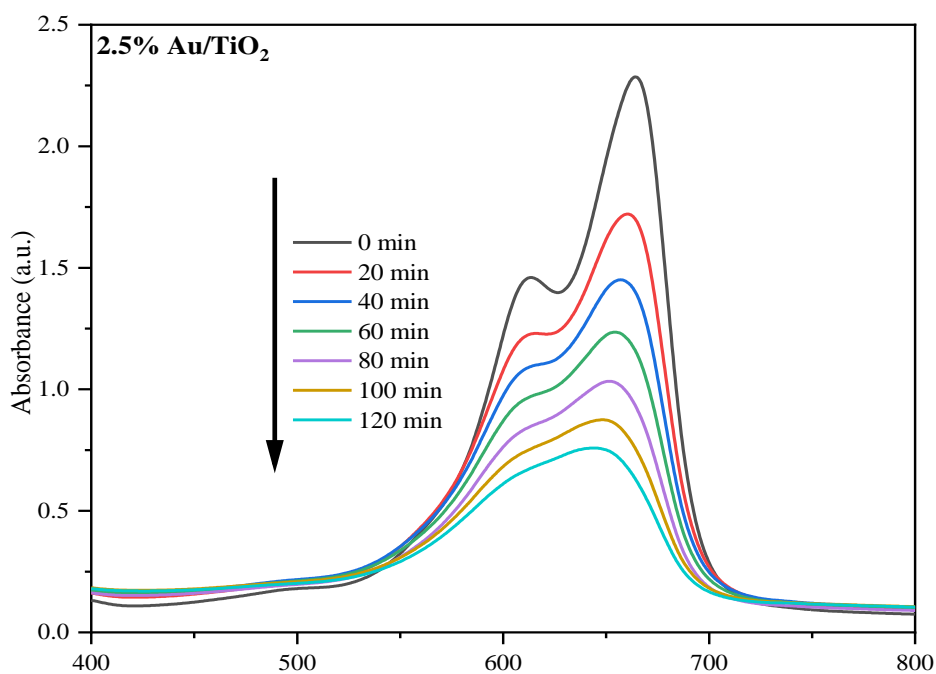

Figure 4.25: UV–Vis spectra of MB degradation, catalysts dose = 15 mg of 2.5% Au/TiO₂, versus irradiation time for MB degradation.

Fig. 4.26 illustrates the calculated degradation rates of MB under various concentrations of X% Au/TiO_2 catalysts. Among the tested catalysts, the 2% Au/TiO_2 exhibited the highest degradation rate, reaching 79.88% after 120 minutes under UV-light irradiation. The photocatalytic degradation efficiency of TiO_2, 0.5% Au/TiO_2, 1% Au/TiO_2, 1.5% Au/TiO_2, 2% Au/TiO_2, and 2.5% Au/TiO_2 catalysts is shown in Table (4.8).
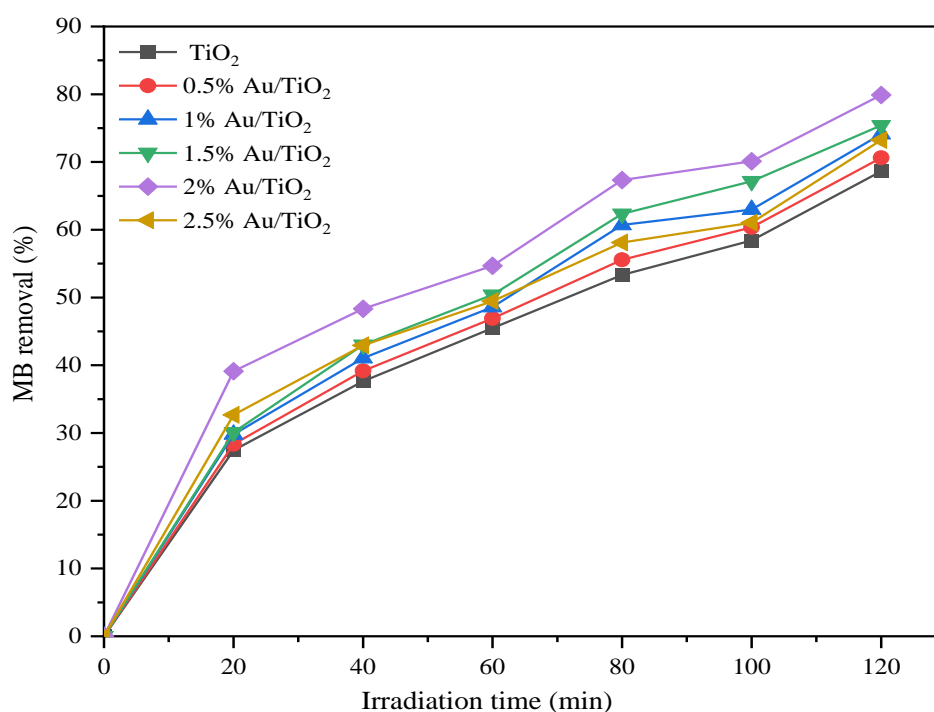
Figure 4.26**:** The degradation of MB dye, catalysts dose = 15 mg of (TiO_2 and X% Au/TiO_2) NPs, as a function of UV light irradiation time.

Table **(4.8):** Degradation percent of MB dye solutions with catalyst at a dose of 15 mg after 120 min under UV irradiation.

Type of Catalyst	PDE (%)
TiO$_2$	68.62
0.5% Au/TiO$_2$	70.60
1.0% Au/TiO$_2$	74.23
1.5% Au/TiO$_2$	75.40
2.0% Au/TiO$_2$	79.88
2.5% Au/TiO$_2$	73.23

The enhanced activity observed in all X% Au/TiO$_2$ catalysts in comparison to pure TiO$_2$ can be attributed to several factors:

1: The samples of X% Au/TiO$_2$ exhibit a wide range of absorption owing to the localized plasmon resonance (SPR) of Au [164,165]. The amplitude of the SPR signals of Au demonstrates a growth with higher Au loading, the location and magnitude of the Au SPR are influenced by factors like Au particle size, shape, and dielectric constant of the support materials [164,166].

2: The Au content in the TiO$_2$ plays a vital role in the photocatalytic performance. The incorporation of Au NPs within the TiO$_2$ structure led to a decrease in the energy gap within the semiconductor structure. The enhanced UV-Vis light-driven activity could be attributed to the presence of Au NPs, effectively serving as electron sinks that mitigate electron-hole recombination [167].

3: The specific surface areas of all the metal-containing photocatalysts were comparable (ranging from 37.08 to 51.62 m^2/g) and slightly higher than that of the TiO$_2$ support (33.36 m^2/g). Previous investigations have demonstrated that

catalytic reactions transpire at an accelerated pace with catalysts possessing elevated specific surface areas [168].

Further increase of Au level from 2 to 2.5% gave a slight decrease in the performance of photocatalytic degradation which can be related to the following reasons:

1: The reason for the reduced activity at high levels of Au can be explained by the fact that there is a limited number of sites on which both the metal and support are necessary for the reaction to take place [169].

2: When the Au content is increased to 2.5%, the absorbance decreases. This is likely because having Au loading higher than 2% causes the NPs to aggregate, resulting in a reduced SPR for the Au NPs catalytic reaction to occur [168,170].

A summary list of studies on the photodegradation of MB by different photocatalytic nano catalysts prepared by different physical and chemical methods is listed in Table (4.9).

Table **(4.9):** List of recently investigated photocatalytic activity of TiO_2 and Au/TiO_2 for MB degradation under UV-Vis irradiation studied by many researchers.

Catalyst	Rate of degradation (%)	Preparation method	Irradiation time(min)	Catalyst dose (mg)	MB Con. (ppm)	Ref.
TiO_2	68.62	Sol-gel	120	15	10	Present work
2% Au/TiO_2	79.88					
TiO_2	45	Sol-gel	80	25	10	[171]
Au/TiO_2	73					
TiO_2	50	Hydrothermal	120	-	10	[108]
Au/TiO_2	66					
TiO_2	40	Magnetron cos puttering	200	-	2	[172]
Au/TiO_2	50					
TiO_2	50	Flame spray pyrolysis (FSP)	200	6	20	[173]
Au/TiO_2	60					
Au/TiO_2	53	Deposition-precipitation	30	100	6.4	[174]
TiO_2	26.7	Electrospinning	60	-	10	[175]
Au/TiO_2	30.5					
TiO_2	92	Sol-gel	240	50	3	[176]
Au/TiO_2	96.48					
Au/TiO_2	93.9	Sol-gel	240	100	15	[177]

Conclusions

In the present work, pure TiO_2 and TiO_2 doped with Au nanoparticles as photocatalysts were successfully synthesized following the sol-gel method and annealed at 450 °C at selected doses for the photodegradation of organic pollutants methylene blue (MB). According to the previous dissection and analysis, the following conclusions can be summarized:

1- During XRD analysis, incorporating Au into the TiO_2 structure did not significantly change the lattice structure, but for X% Au/TiO_2 NPs samples, a polycrystalline plane (111) was observed at $2\theta = 38.2°$, confirming the presence of Au. The crystallite size decreased in X% Au/TiO_2 samples compared to pure TiO_2.

2- XPS analysis confirmed the presence of Ti and O elements in the pure TiO_2 sample, along with Au in the X% Au/TiO_2 samples. Carbon was also present in the structure. A shift in peak energy of other elements was compared to carbon. An additional peak at 80-90 eV confirmed the presence of Au in samples with Au doping. After Au doping, a negative shift occurred in the peaks related to Ti in all Au/TiO_2 samples.

3- The FTIR spectrum in the range of 4000- 400 nm showed the presence of OH, CH_2, and Ti-O-Ti groups in pure TiO_2 and X% Au/TiO_2 NPs samples. While in the X% Au/TiO_2 samples, a relatively weak additional peak at 2108.89 cm^{-1} indicated the presence of Au.

4- Using FESEM, Mapping, and EDX analysis. The samples exhibited a spherical shape, indicating that the loading of gold nanoparticles in TiO_2 did not significantly affect the structural shape. Mapping analysis revealed a uniform distribution of elements in all samples.

5- TEM analysis showed that the samples had a sphere-like morphology. The average particle size in X% Au/TiO_2 samples was smaller (28 nm) compared with pure TiO_2 (31 nm).

6- BET analysis recorded the specific surface area increased after Au loading in the pure TiO_2 structure, from 33.38 m^2/g for pure TiO_2 to 51.62 m^2/g for 2.5% Au/TiO_2.

7- Ultraviolet–visible (UV–Vis) spectroscopy of the samples was evaluated from 200 to 800 nm, revealing an absorption peak for TiO_2 in the range of 300-330 nm for all samples. In X% Au/TiO_2 samples, a wide peak in the range of 490-590 nm indicated the presence of Au NPs. The observed band gap energy of pure TiO_2 is 3.24 eV. However, as the amount of Au loading increases in X% Au/TiO_2 samples, there is a decreasing trend in the band gap energy.

8- The best catalytic dose was investigated by testing the photocatalytic degradation process for different amounts of TiO_2 catalyst (05, 10, 15, 20, and 25) mg, with an initial concentration of 10 ppm. It was assessed that under UV light irradiation, an amount of 15 mg of TiO_2 is the best catalytic dose with a degradation efficiency of 68.62%. After that the degradation of MB, for all catalysts, including 0.5% Au/TiO_2, 1% Au/TiO_2, 1.5% Au/TiO_2, 2% Au/TiO_2, and 2.5% Au/TiO_2 were measured under the same conditions (initial concentration of MB =10 ppm, catalysts dose = 15 mg, at 120 min UV light irradiation). The highest MB degradation percentage of 79.88% was observed with the 2% Au/TiO_2 catalyst.

Suggestions for Further Studies

The investigation revealed that the parameters that impact photocatalytic reactions are recommended for forthcoming research endeavors. On this basis, further research should examine these parameters, including:

1- The effect of other experimental parameters such as the concentration of precursor, the temperature of calcination, pH solution, light intensity, and selected wavelength, may be extensively studied.

2- The methylene blue (MB) degradation using the prepared nano-crystal structures was studied and a very promising finding was obtained under ultraviolet (UV) irradiation. Therefore, it is important to examine various kinds of dyes such as Rhodamine B dye, carmine dye, methyl red dye, and methyl orange, to study the photocatalytic activity of the prepared nano-catalysts.

3- Furthermore, the efficacy of the existing catalysts under visible light can be assessed.

References

References

[1] Dvorak BI. Drinking Water Treatment: Activated Carbon Filtration. University of Nebraska–Lincoln Extension, Institute of Agriculture and Natural Resources 2013:1–4.

[2] Dąbrowski A, Podkościelny P, Hubicki Z, Barczak M. Adsorption of phenolic compounds by activated carbon - A critical review. Chemosphere 2005; 58:1049–70. https://doi.org/10.1016/j.chemosphere.2004.09.067.

[3] MacWan DP, Dave PN, Chaturvedi S. A review on nano-TiO_2 sol-gel type syntheses and its applications. J Mater Sci 2011; 46:3669–86. https://doi.org/10.1007/s10853-011-5378-y.

[4] Jalawkhan RS, Ouda AA, Abdul-Lettif AM, Mohamad Alosfur FK. Effect of solvents on the morphology of TiO_2 nanoparticles prepared by microwave method. IOP Conf Ser Mater Sci Eng 2020;928. https://doi.org/10.1088/1757-899X/928/7/072159.

[5] Pfeifer V, Erhart P, Li S, Rachut K, Morasch J, Reckers P, Brötz J, Reckers P, Mayer Th, Rühle S, Zaban A, Mora I, Bisquert J, Jaegermann W, Klein A. Supporting Information: Energy Band Alignment Between Anatase and Rutile TiO_2. J Phys Chem 2013; 4:4182–7.

[6] Alamgir, Khan W, Ahmad S, Mehedi Hassan M, Naqvi AH. Structural phase analysis, band gap tuning and fluorescence properties of Co doped TiO_2 nanoparticles. Opt Mater (Amst) 2014; 38:278–85. https://doi.org/10.1016/j.optmat.2014.10.054.

[7] Kobayashi Y, Ishii Y, Yamane H, Watanabe K ichi, Koda H, Kunigami H, Kunigami H. Fabrication of TiO_2/Pt core-shell particles by electroless metal plating. Colloids Surf A Physicochem Eng Asp 2014; 448:88–92. https://doi.org/10.1016/j.colsurfa.2014.02.018.

[8] Lei XF, Xue XX, Yang H. Preparation and characterization of Ag-doped TiO_2 nanomaterials and their photocatalytic reduction of Cr (VI) under visible light. Appl Surf Sci 2014; 321:396–403. https://doi.org/10.1016/j.apsusc.2014.10.045.

[9] Liu Q, Ding D, Ning C, Wang X. Black Ni-doped TiO_2 photoanodes for high-efficiency photoelectrochemical water-splitting. Int J Hydrogen Energy 2015; 40:2107–14. https://doi.org/10.1016/j.ijhydene.2014.12.064.

[10] Park H, Park Y, Kim W, Choi W. Surface modification of TiO_2 photocatalyst for environmental applications. Journal of Photochemistry and Photobiology C: Photochemistry Reviews 2013; 15:1–20. https://doi.org/10.1016/j.jphotochemrev.2012.10.001.

[11] Cybula A, Nowaczyk G, Jarek M, Zaleska A. Preparation and characterization of Au/Pd Modified- TiO_2 photocatalysts for phenol and toluene degradation under visible light - The effect of calcination temperature. J Nanomater 2014;2014. https://doi.org/10.1155/2014/918607.

[12] Obregón S, Muñoz-Batista MJ, Fernández-García M, Kubacka A, Colón G. Cu- TiO_2 systems for the photocatalytic H_2 production: Influence of structural and surface support features. Appl Catal B 2015; 179:468–78. https://doi.org/10.1016/j.apcatb.2015.05.043.

[13] Sung-Suh HM, Choi JR, Hah HJ, Koo SM, Bae YC. Comparison of Ag deposition effects on the photocatalytic activity of nanoparticulate TiO_2 under visible and UV light irradiation. J Photochem Photobiol A Chem 2004; 163:37–44. https://doi.org/10.1016/S1010-6030(03)00428-3.

[14] Basavarajappa PS, Patil SB, Ganganagappa N, Reddy KR, Raghu A V, Reddy CV. Recent progress in metal-doped TiO_2, non-metal doped/codoped TiO_2 and TiO_2 nanostructured hybrids for enhanced photocatalysis. Int J Hydrogen Energy 2020; 45:7764–78.

[15] Akakuru OU, Iqbal ZM, Wu A. TiO_2 nanoparticles: properties and applications. TiO_2 Nanoparticles: Applications in Nanobiotechnology and Nanomedicine 2020:1–66.

[16] Hernández R, Hernández-Reséndiz JR, Martínez-Chávez A, Velázquez-Castillo R, Escobar-Alarcón L, Esquivel K. X-ray diffraction Rietveld structural analysis of Au– TiO_2 powders synthesized by sol–gel route coupled to microwave and sonochemistry. J Solgel Sci Technol 2020; 95:239–52. https://doi.org/10.1007/s10971-020-05264-5.

[17] Esposito S. "Traditional" sol-gel chemistry as a powerful tool for the preparation of supported metal and metal oxide catalysts. Materials 2019; 12:668.

[18] Forgacs E, Cserháti T, Oros G. Removal of synthetic dyes from wastewaters: A review. Environ Int 2004; 30:953–71. https://doi.org/10.1016/j.envint.2004.02.001.

[19] Sleiman M, Vildozo D, Ferronato C, Chovelon JM. Photocatalytic degradation of azo dye Metanil Yellow: Optimization and kinetic modeling using a chemometric approach. Appl Catal B 2007; 77:1–11. https://doi.org/10.1016/j.apcatb.2007.06.015.

[20] Chakrabarti S, Dutta BK. Photocatalytic degradation of model textile dyes in wastewater using ZnO as semiconductor catalyst. J Hazard Mater 2004; 112:269–78. https://doi.org/10.1016/j.jhazmat.2004.05.013.

[21] Asmathunisha N, Kathiresan K. Colloids and Surfaces B: Biointerfaces A review on biosynthesis of nanoparticles by marine organisms. Colloids Surf B Biointerfaces 2013; 103:283–7.

[22] Hornyak GL, Tibbals HF, Dutta J, Moore JJ. Introduction to nanoscience and nanotechnology. CRC press; 2008.

[23] Skocaj M, Filipic M, Petkovic J, Novak S. Titanium dioxide in our everyday life; is it safe? Radiol Oncol 2011; 45:227.

[24] Parrino F, Palmisano L. Titanium Dioxide (TiO_2) and Its Applications. elsevier; 2020.

[25] Akakuru OU, Iqbal ZM, Wu A. TiO_2 nanoparticles: properties and applications. TiO_2 Nanoparticles: Applications in Nanobiotechnology and Nanomedicine 2020:1–66.

[26] Tsuzuki T. Applications and market opportunities of nanoparticulate materials. Boca Raton, USA: CRC Press; 2013.

[27] Ahmad MZ, Sadek AZ, Latham K, Kita J, Moos R, Wlodarski W. Chemically synthesized one-dimensional zinc oxide nanorods for ethanol sensing. Sens Actuators B Chem 2013; 187:295–300. https://doi.org/10.1016/j.snb.2012.11.042.

[28] Giorgetti E, Alloisio M, Dellepiane G, Giusti A, Cuniberti C, Margheri G. I Nvestigation of N Anostructured M Etal / P Olymer 2006:7–11.

[29] Di Ventra M, Evoy S, Heflin Jr JR. Introduction to nanoscale science and technology. Springer; 2004.

[30] Siegel RW, Hu E. Nanostructure science and technology: R & D status and trends in nanoparticles, nanostructured materials and nanodevices. Springer Science & Business Media; 1999.

[31] Lee JH, Jang JT, Choi JS, Moon SH, Noh SH, Kim JW. Exchange-coupled magnetic nanoparticles for efficient heat induction. Nat Nanotechnol 2011; 6:418–22. https://doi.org/10.1038/nnano.2011.95.

[32] Muller O, Dengler S, Ritt G, Eberle B. Size and shape effects on the nonlinear optical behavior of silver nanoparticles for power limiters. Appl Opt 2013; 52:139–49.

[33] Zhou Z-Y, Tian N, Li J-T, Broadwell I, Sun S-G. Nanomaterials of high surface energy with exceptional properties in catalysis and energy storage. Chem Soc Rev 2011; 40:4167–85.

[34] Hodson L, Methner M, Zumwalde RD. Approaches to safe nanotechnology; managing the health and safety concerns associated with engineered nanomaterials 2009.

[35] Fouda MMG. Antibacterial modification of textiles using nanotechnology. InTech; 2012.

[36] Rawat RS. Dense Plasma Focus - From Alternative Fusion Source to Versatile High Energy Density Plasma Source for Plasma Nanotechnology. J Phys Conf Ser, vol. 591, Institute of Physics Publishing; 2015. https://doi.org/10.1088/1742-6596/591/1/012021.

[37] Nikalje AP. Nanotechnology and its applications in medicine. Med Chem 2015; 5:81–9.

[38] Joudeh N, Linke D. Nanoparticle classification, physicochemical properties, characterization, and applications: a comprehensive review for biologists. J Nanobiotechnology 2022; 20:1–29. https://doi.org/10.1186/s12951-022-01477-8.

[39] Pelaez M, Nolan NT, Pillai SC, Seery MK, Falaras P, Kontos AG, Dunlop P S M. A review on the visible light active titanium dioxide photocatalysts for environmental applications. Appl Catal B 2012; 125:331–49.

[40] Antić Ž, Krsmanović RM, Nikolić MG, Marinović-Cincović M, Mitrić M, Polizzi S, et al. Multisite luminescence of rare earth doped TiO_2 anatase nanoparticles. Mater Chem Phys 2012; 135:1064–9.

[41] Tio A/, Tio A/, Ghori MZ. Synthesis and Functional Applications of Highly Photocatalytic TiO_2 Based Surfaces. n.d.

[42] Landmann M, Rauls E, Schmidt WG. The electronic structure and optical response of rutile, anatase and brookite TiO_2. Journal of Physics: Condensed Matter 2012; 24:195503.

[43] Pookmanee P, Phanichphant S. Titanium dioxide powder prepared by a sol-gel method. Journal of Ceramic Processing Research 2009; 10:167–70.

[44] Bokov D, Turki Jalil A, Chupradit S, Suksatan W, Javed Ansari M, Shewael IH, Valiev GH. Nanomaterial by Sol-Gel Method: Synthesis and Application. Advances in Materials Science and Engineering 2021;2021. https://doi.org/10.1155/2021/5102014.

[45] Su C, Hong BY, Tseng CM. Sol-gel preparation and photocatalysis of titanium dioxide. Catal Today 2004; 96:119–26. https://doi.org/10.1016/j.cattod.2004.06.132.

[46] Haque FZ, Nandanwar R, Singh P. Evaluating photodegradation properties of anatase and rutile TiO_2 nanoparticles for organic compounds. Optik (Stuttg) 2017; 128:191–200. https://doi.org/10.1016/j.ijleo.2016.10.025.

[47] Barakat NAM, Hamza AM, Al-Deyab SS, Qurashi A, Kim HY. Titanium-based polymeric electrospun nanofiber mats as a novel organic semiconductor. Materials Science and Engineering: B 2012; 177:34–42.

[48] de Carvalho Tomás E. Characterisation of the ceria and yttria co-doped scandia zirconia; produced by an innovative sol-gel and combustion process 2010.

[49] Hamza MA, Saiof FN, Al-ithawi AS, Ameen MA, Yaseen HM. Prepared of Nd: TiO_2 Nano Particles Powder as IR Filter via Sol-Gel 2013.

[50] Sensor B-DGMI. Prepared of Olive Oil Doped SiO_2 via Sol-Gel Technique 2013.

[51] Hamzah MA, Ezzat AM, Ameen MA, Yaseen HM, Khalif MI. Preparations of Nd: TiO_2 as Laser active medium by Sol-Gel method. International Journal of Application or Innovation in Engineering & Management (IJAIEM) 2014;3.

[52] Sakka S. Handbook of sol-gel science and technology. 1. Sol-gel processing. vol. 1. Springer Science & Business Media; 2005.

[53] Segal D. Chemical synthesis of advanced ceramic materials. Cambridge University Press; 1991.

[54] Almeida RM, Gonçalves MC. Sol–gel process and products. Encyclopedia of Glass Science, Technology, History, and Culture 2021;2:969–79.

[55] Nishio K, Tsuchiya T. Sol-gel processing of thin films with metal salts. Handbook of Sol-Gel Science and Technology: Processing, Characterization and Applications 2018:133–54.

[56] Orwat K, Bernard P, Migdał-Mikuli A. Alternative conceptions of common salt hydrolysis among upper-secondary-school students. n.d.

[57] Chruściel J, Ślusarski L. Synthesis of nanosilica by the sol-gel method and its activity toward polymers. Materials Science 2003; 21:461–9.

[58] Kurtoglu M. Effect of doping on the photocatalytic, electronic and mechanical properties of sol-gel titanium dioxide films 2011.

[59] Colombo P. Polymer derived ceramics: from nano-structure to applications. DEStech Publications, Inc; 2010.

[60] Rechberger F, Tervoort E, Niederberger M. Nonaqueous sol- gel synthesis of $InTaO_4$ nanoparticles and their assembly into macroscopic aerogels. Journal of the American Ceramic Society 2017; 100:4483–90.

[61] ANDERSSON J. Evaluation of Capillary Flow in Gels 2016.

[62] German RM, Suri P, Park SJ. Liquid phase sintering. J Mater Sci 2009; 44:1–39.

[63] Bhatt N, Mishra A, Goswami R, Prasad B. Preparation of Silica Nano-Particles by Sol-Gel Method and Its Characterization. Journal of Graphic Era University 2021; 9:215–30. https://doi.org/10.13052/jgeu0975-1416.927.

[64] Milea CA, Bogatu C, Duta A. The influence of parameters in silica sol-gel process. Bulletin of TheTransilvania University of Brasov 2011; 4:53.

[65] Watson S, Beydoun D, Scott J, Amal R. Preparation of nanosized crystalline TiO_2 particles at low temperature for photocatalysis. Journal of Nanoparticle Research 2004; 6:193–207.

[66] Licciulli A, Lisi D. Self-cleaning glass. Universita Degli Studi Di Lecce 2002.

[67] Dreaden EC, Mac key MA, Huang X, Kang B, El-Sayed MA. Beating cancer in multiple ways using nanogold. Chem Soc Rev 2011; 40:3391–404. https://doi.org/10.1039/c0cs00180e.

[68] Tian Y, Tatsuma T. Mechanisms and applications of plasmon-induced charge separation at TiO_2 films loaded with gold nanoparticles. J Am Chem Soc 2005; 127:7632–7. https://doi.org/10.1021/ja042192u.

[69] Brus L. Noble Metal Nanocrystals: Plasmon Electron Transfer Photochemistry and Single Molecule Raman Spectroscopy. n.d.

[70] Kamat P V. Photoinduced transformations in semiconductor-metal nanocomposite assemblies*. vol. 74. 2002.

[71] Moores A, Goettmann F. The plasmon band in noble metal nanoparticles: An introduction to theory and applications. New Journal of Chemistry 2006; 30:1121–32. https://doi.org/10.1039/b604038c.

[72] Rstl.1857.0011 n.d.

[73] Tabor C, Murali R, Mahmoud, El-Sayed MA. On the use of plasmonic nanoparticle pairs as a plasmon ruler: The dependence of the near-field dipole plasmon coupling on nanoparticle size and shape. Journal of Physical Chemistry A 2009; 113:1946–53. https://doi.org/10.1021/jp807904s.

[74] Cheng CS, Chen YQ, Lu CJ. Organic vapour sensing using localized surface plasmon resonance spectrum of metallic nanoparticles self-assemble monolayer. Talanta 2007; 73:358–65. https://doi.org/10.1016/j.talanta.2007.03.058.

[75] Huang H, Huang S, Yuan S, Qu C, Chen Y, Xu Z, Liao B, Zeng Y, Chu P K. High-sensitivity biosensors fabricated by tailoring the localized surface plasmon resonance property of core-shell gold nanorods. Anal Chim Acta 2011; 683:242–7. https://doi.org/10.1016/j.aca.2010.10.033.

[76] Oldenburg SJ, Averitt RD, Westcott SL, Halas NJ. Nanoengineering of optical resonances. vol. 288. 1998.

[77] Oldenburg SJ, Jackson JB, Westcott SL, Halas NJ. Infrared extinction properties of gold nanoshells. 1999.

[78] Hirsch LR, Jackson JB, Lee A, Halas NJ, West JL. A whole blood immunoassay using gold nanoshells. Anal Chem 2003; 75:2377–81. https://doi.org/10.1021/ac0262210.

[79] Cao YC, Hua XF, Zhu XX, Wang Z, Huang ZL, Zhao Y Di, Chen H, Liu M X. Preparation of Au coated polystyrene beads and their application in an immunoassay. J Immunol Methods 2006; 317:163–70. https://doi.org/10.1016/j.jim.2006.10.004.

[80] Hurum DC, Agrios AG, Gray KA, Rajh T, Thurnauer MC. Explaining the enhanced photocatalytic activity of Degussa P25 mixed-phase TiO_2 using EPR. J Phys Chem B 2003; 107:4545–9.

[81] Zhang X, Lin Y, He D, Zhang J, Fan Z, Xie T. Interface junction at anatase/rutile in mixed-phase TiO_2: formation and photo-generated charge carriers properties. Chem Phys Lett 2011; 504:71–5.

[82] Freitas de Freitas L, Varca GHC, dos Santos Batista JG, Benévolo Lugão A. An overview of the synthesis of gold nanoparticles using radiation technologies. Nanomaterials 2018; 8:939.

[83] Tsukamoto D, Shiraishi Y, Sugano Y, Ichikawa S, Tanaka S, Hirai T. Gold nanoparticles located at the interface of anatase/rutile TiO_2 particles as active plasmonic photocatalysts for aerobic oxidation. J Am Chem Soc 2012; 134:6309–15.

[84] Wang H, You T, Shi W, Li J, Guo L. Au/ TiO$_2$/Au as a plasmonic coupling photocatalyst. The Journal of Physical Chemistry C 2012; 116:6490–4.

[85] Tsukamoto D, Shiraishi Y, Sugano Y, Ichikawa S, Tanaka S, Hirai T. Gold nanoparticles located at the interface of anatase/rutile TiO$_2$ particles as active plasmonic photocatalysts for aerobic oxidation. J Am Chem Soc 2012; 134:6309–15.

[86] Priebe JB, Radnik J, Lennox AJJ, Pohl M-M, Karnahl M, Hollmann D, et al. Solar hydrogen production by plasmonic Au– TiO$_2$ catalysts: impact of synthesis protocol and TiO$_2$ phase on charge transfer efficiency and H2 evolution rates. ACS Catal 2015; 5:2137–48.

[87] Augugliaro V, Litter M, Palmisano L, Soria J. The combination of heterogeneous photocatalysis with chemical and physical operations: A tool for improving the photoprocess performance. Journal of Photochemistry and Photobiology C: Photochemistry Reviews 2006; 7:127–44.

[88] Braslavsky SE. Glossary of terms used in photochemistry, (IUPAC Recommendations 2006). Pure and Applied Chemistry 2007; 79:293–465.

[89] Masel RI. Chemical kinetics and catalysis. vol. 10. Wiley-Interscience New York; 2001.

[90] JINKAI Z. Modified Titanium Dioxide (TiO$_2$) photocatalysts for the degradation of organic pollutants in wastewater 2007.

[91] Cheng H, Wang J, Zhao Y, Han X. Effect of phase composition, morphology, and specific surface area on the photocatalytic activity of TiO$_2$ nanomaterials. RSC Adv 2014; 4:47031–8.

[92] Pattnaik A, Sahu JN, Poonia AK, Ghosh P. Current perspective of nano-engineered metal oxide based photocatalysts in advanced oxidation processes for degradation of organic pollutants in wastewater. Chemical Engineering Research and Design 2023.

[93] Gaya UI, Abdullah AH. Heterogeneous photocatalytic degradation of organic contaminants over titanium dioxide: a review of fundamentals,

progress and problems. Journal of Photochemistry and Photobiology C: Photochemistry Reviews 2008; 9:1–12.

[94] Wang X, Caruso RA. Enhancing photocatalytic activity of titania materials by using porous structures and the addition of gold nanoparticles. J Mater Chem 2011; 21:20–8.

[95] Jose D, Sorensen CM, Rayalu SS, Shrestha KM, Klabunde KJ. Au- TiO_2 nanocomposites and efficient photocatalytic hydrogen production under UV-visible and visible light illuminations: a comparison of different crystalline forms of TiO_2. International Journal of Photoenergy 2013;2013.

[96] Kwon B-G, Yoon J-Y. Experimental evidence of the mobility of hydroperoxyl/superoxide anion radicals from the illuminated TiO_2 interface into the aqueous phase. Bull Korean Chem Soc 2009; 30:667–70.

[97] Kamat P V. Photophysical, photochemical and photocatalytic aspects of metal nanoparticles. J Phys Chem B 2002; 106:7729–44.

[98] Liu Y-C, Juang L-C. Electrochemical methods for the preparation of gold-coated TiO_2 nanoparticles with variable coverages. Langmuir 2004; 20:6951–5.

[99] Sridewi N, Tan L, Sudesh K. Solar photocatalytic decolorization and detoxification of industrial batik dye wastewater using P (3HB) - TiO_2 nanocomposite films. Clean–Soil, Air, Water 2011;39:265–73.

[100] Yu J, Dai G, Xiang Q, Jaroniec M. Fabrication and enhanced visible-light photocatalytic activity of carbon self-doped TiO_2 sheets with exposed {001} facets. J Mater Chem 2011; 21:1049–57.

[101] Xiang Q, Yu J, Wong PK. Quantitative characterization of hydroxyl radicals produced by various photocatalysts. J Colloid Interface Sci 2011; 357:163–7.

[102] Zhou X, Luo Z, Tao P, Jin B, Wu Z, Huang Y. Facile preparation and enhanced photocatalytic H_2-production activity of Cu $(OH)_2$ nanospheres modified porous g-C3N4. Mater Chem Phys 2014; 143:1462–8.

[103] Yu J, Dai G, Cheng B. Effect of crystallization methods on morphology and photocatalytic activity of anodized TiO_2 nanotube array films. The Journal of Physical Chemistry C 2010; 114:19378–85.

[104] Yu J, Yue L, Liu S, Huang B, Zhang X. Hydrothermal preparation and photocatalytic activity of mesoporous Au– TiO_2 nanocomposite microspheres. J Colloid Interface Sci 2009; 334:58–64.

[105] Xiang Q, Yu J, Cheng B, Ong HC. Microwave- hydrothermal preparation and visible- light photoactivity of plasmonic photocatalyst Ag- TiO_2 nanocomposite hollow spheres. Chemistry–An Asian Journal 2010; 5:1466–74.

[106] Padikkaparambil S, Narayanan B, Yaakob Z, Viswanathan S, Tasirin SM. Au/ TiO_2 reusable photocatalysts for dye degradation. International Journal of Photoenergy 2013;2013. https://doi.org/10.1155/2013/752605.

[107] Wen Y, Liu B, Zeng W, Wang Y. Plasmonic photocatalysis properties of Au nanoparticles precipitated anatase/rutile mixed TiO_2 nanotubes. Nanoscale 2013; 5:9739–46. https://doi.org/10.1039/c3nr03024e.

[108] Chen Y, Bian J, Qi L, Liu E, Fan J. Efficient degradation of methylene blue over two-dimensional Au/ TiO_2 nanosheet films with overlapped light harvesting nanostructures. J Nanomater 2015; 16:254.

[109] Salgado SYA, Zamora RMR, Zanella R, Peral J, Malato S, Maldonado MI. Photocatalytic hydrogen production in a solar pilot plant using a Au/ TiO_2 photo catalyst. Int J Hydrogen Energy 2016; 41:11933–40.

[110] Pérez Campos R, Contreras Cuevas A, Esparza Muñoz RA. Characterization of metals and alloys. Characterization of Metals and Alloys 2017.

[111] Mehta A, Sharma M, Kumar A, Basu S. Effect of Au content on the enhanced photocatalytic efficiency of mesoporous Au/ TiO_2 nanocomposites in UV and sunlight. Gold Bull 2017; 50:33–41. https://doi.org/10.1007/s13404-016-0191-7.

[112] Weng M, Yu X. Electrochemical oxidation of para-aminophenol with rare earth doped lead dioxide electrodes: Kinetics modeling and mechanism. Front Chem 2019; 7:382.

[113] Aswathy PM, Sarina P, Kavitha MK, Priya MJ, John H, Jayaraj MK. Development of Au doped TiO_2 nanofibers for photocatalytic applications. AIP Conf Proc, vol. 2082, American Institute of Physics Inc.; 2019. https://doi.org/10.1063/1.5093825.

[114] Truppi A, Petronella F, Placido T, Margiotta V, Lasorella G, Giotta L, Giannini C, Sibillano T, Murgolo S, Mascolo G, Agostiano A, Curri M.L, Comparelli R. Gram-scale synthesis of UV–vis light active plasmonic photocatalytic nanocomposite based on TiO_2/Au nanorods for degradation of pollutants in water. Appl Catal B 2019; 243:604–13.

[115] Kholikov B, Hussain J, Hayat S, Zeng H. Surface plasmon resonance improved photocatalytic activity of Au/ TiO_2 nanocomposite under visible light for degradation of pollutants. Journal of the Chinese Chemical Society 2021; 68:1908–15.

[116] Liu L, He A. Optical and Electrochemical Study on the Performance of Au@ TiO_2 core-shell Heterostructured Nanoparticles as Photocatalyst for Photodegradation of Methylene Blue under Solar-light Irradiation. Int J Electrochem Sci 2022; 17:2.

[117] Yu H, Li S, Peng S, Yu Z, Chen F, Liu X, Guo J, Zhu B, Huang W, Zhang S. Construction of rutile/anatase TiO_2 homojunction and metal-support interaction in Au/ TiO_2 for visible photocatalytic water splitting and degradation of methylene blue. Int J Hydrogen Energy 2023; 48:975–90.

[118] Nasr A.A .Infrared Radiation. InTech;2012. n.d.

[119] Scerri ER. The periodic table: A very short introduction. vol. 289. Oxford University Press, USA; 2011.

[120] Scerri E. The periodic table: its story and its significance. Oxford University Press; 2019.

[121] Inkson BJ. Scanning electron microscopy (SEM) and transmission electron microscopy (TEM) for materials characterization. Materials characterization using nondestructive evaluation (NDE) methods, Elsevier; 2016, p. 17–43.

[122] Peña-Rodríguez O, Pal U. Exploiting the tunable optical response of metallic nanoshells. UV-VIS and Photoluminescence Spectroscopy for Nanomaterials Characterization, Springer; 2013, p. 99–149.

[123] Chen Z, Dinh HN, Miller E. Photoelectrochemical water splitting. vol. 344. Springer; 2013.

[124] Makuła P, Pacia M, Macyk W. How to correctly determine the band gap energy of modified semiconductor photocatalysts based on UV–Vis spectra. J Phys Chem Lett 2018; 9:6814–7.

[125] Khalil M, Anggraeni ES, Ivandini TA, Budianto E. Exposing TiO_2 (001) crystal facet in nano Au-TiO_2 heterostructures for enhanced photodegradation of methylene blue. Appl Surf Sci 2019; 487:1376–84. https://doi.org/10.1016/j.apsusc.2019.05.232.

[126] Yu J, Yue L, Liu S, Huang B, Zhang X. Hydrothermal preparation and photocatalytic activity of mesoporous Au– TiO_2 nanocomposite microspheres. J Colloid Interface Sci 2009; 334:58–64.

[127] Ibrahim NS, Leaw WL, Mohamad D, Alias SH, Nur H. A critical review of metal-doped TiO_2 and its structure–physical properties–photocatalytic activity relationship in hydrogen production. Int J Hydrogen Energy 2020; 45:28553–65.

[128] Patel SKS, Jena P, Gajbhiye NS. Structural and room-temperature ferromagnetic properties of pure and Ni-doped TiO_2 nanotubes. Mater Today Proc 2019; 15:388–93.

[129] Tijani JO, Ndamitso MM, Abdulkareem AS. Facile synthesis and characterization of TiO_2 nanoparticles: X-ray peak profile analysis using Williamson–Hall and Debye–Scherrer methods 2021.

[130] Nkele AC, Chime UK, Asogwa L, Nwanya AC, Nwankwo U, Ukoba K, et al. A study on titanium dioxide nanoparticles synthesized from titanium isopropoxide under SILAR-induced gel method: Transition from anatase to rutile structure. Inorg Chem Commun 2020; 112:107705.

[131] Kim MG, Kang JM, Lee JE, Kim KS, Kim KH, Cho M, et al. Effects of calcination temperature on the phase composition, photocatalytic

degradation, and virucidal activities of TiO$_2$ nanoparticles. ACS Omega 2021; 6:10668–78.

[132] Almashhori K, Ali TT, Saeed A, Alwafi R, Aly M, Al-Hazmi FE. Antibacterial and photocatalytic activities of controllable (anatase/rutile) mixed phase TiO$_2$ nanophotocatalysts synthesized via a microwave-assisted sol–gel method. New Journal of Chemistry 2020; 44:562–70.

[133] Aji BB, Shih SJ, Pradita T. Controlled crystal phase of TiO$_2$ by spray pyrolysis method. J Phys Conf Ser, vol. 817, IOP Publishing; 2017, p. 012021.

[134] Fang D, He F, Xie J, Xue L. Calibration of binding energy positions with C1s for XPS results. Journal of Wuhan University of Technology-Mater Sci Ed 2020; 35:711–8.

[135] Baker LR, Hervier A, Seo H, Kennedy G, Komvopoulos K, Somorjai GA. Highly n-type titanium oxide as an electronically active support for platinum in the catalytic oxidation of carbon monoxide. The Journal of Physical Chemistry C 2011; 115:16006–11.

[136] Lu YH, Xu MM, Zhang CJ, Yuan YX, Yao JL. Surface Enhanced Raman Spectroscopic Studies on Surface Plasmon Resonance Catalytic Activity of TiO$_2$-Metal Nanocomposites. Nano Hybrids and Composites 2023; 38:1–14.

[137] Liu T, Chen W, Huang T, Duan G, Yang X, Liu X. Titania-on-gold nanoarchitectures for visible-light-driven hydrogen evolution from water splitting. J Mater Sci 2016; 51:6987–97. https://doi.org/10.1007/s10853-016-9987-3.

[138] Zhang K, Lu G, Chu F, Huang X. Au/ TiO$_2$ nanobelts: thermal enhancement vs. plasmon enhancement for visible-light-driven photocatalytic selective oxidation of amines into imines. Catal Sci Technol 2021; 11:7060–71.

[139] Waheed A, Shi Q, Maeda N, Meier DM, Qin Z, Li G, Baiker A. Strong activity enhancement of the photocatalytic degradation of an azo dye on Au/ TiO$_2$ doped with FeOx. Catalysts 2020; 10:933.

[140] Shooshtari M, Salehi A, Vollebregt S. Effect of temperature and humidity on the sensing performance of TiO_2 nanowire-based ethanol vapor sensors. Nanotechnology 2021; 32:325501.

[141] Hong T, Yin J-Y, Nie S-P, Xie M-Y. Applications of infrared spectroscopy in polysaccharide structural analysis: Progress, challenge and perspective. Food Chem X 2021; 12:100168.

[142] Manzoli M, Chiorino A, Vindigni F, Boccuzzi F. Hydrogen interaction with gold nanoparticles and clusters supported on different oxides: A FTIR study. Catal Today 2012; 181:62–7.

[143] Dorranian D, Solati E, Dejam L. Photoluminescence of ZnO nanoparticles generated by laser ablation in deionized water. Applied Physics A 2012; 109:307–14.

[144] Qutub N, Singh P, Sabir S, Sagadevan S, Oh W-C. Enhanced photocatalytic degradation of Acid Blue dye using CdS/ TiO_2 nanocomposite. Sci Rep 2022; 12:5759.

[145] Fathy M, Hamad H. Influence of calcination temperatures on the formation of anatase TiO_2 nano rods with a polyol-mediated solvothermal method. RSC Adv 2016; 6:7310–6.

[146] Huseynov EM, Huseynova EA. Infrared spectroscopy of nanocrystalline anatase (TiO_2) particles under the neutron irradiation. Opt Mater (Amst) 2023; 144:114351.

[147] Nasikhudin, Diantoro M, Kusumaatmaja A, Triyana K. Study on photocatalytic properties of TiO_2 nanoparticle in various pH condition. J Phys Conf Ser, vol. 1011, IOP Publishing; 2018, p. 012069.

[148] Gogoi D, Namdeo A, Golder AK, Peela NR. Ag-doped TiO_2 photocatalysts with effective charge transfer for highly efficient hydrogen production through water splitting. Int J Hydrogen Energy 2020; 45:2729–44.

[149] Wu MT, Chow TJ. TiO_2 particles prepared by size control self-assembly and their usage on dye-sensitized solar cell. Microporous and Mesoporous Materials 2014; 196:354–8.

[150] Lee DG, Kim M, Kim BJ, Kim DH, Lee SM, Choi M, Lee S, Jung H S. Effect of TiO_2 particle size and layer thickness on mesoscopic perovskite solar cells. Appl Surf Sci 2019; 477:131–6.

[151] Rouquerol J, Sing KS W, Llewellyn P. Adsorption by metal oxides. Adsorpt By Powders Porous Solids Princ Methodol Appl, 2013:393–465.

[152] Chattoraj D. Adsorption and the Gibbs surface excess. Springer Science & Business Media; 2012.

[153] Tahir B, Tahir M, Amin NAS. Photocatalytic CO_2 conversion over Au/ TiO_2 nanostructures for dynamic production of clean fuels in a monolith photoreactor. Clean Technol Environ Policy 2016; 18:2147–60.

[154] Wang H, Faria JL, Dong S, Chang Y. Mesoporous Au/ TiO_2 composites preparation, characterization, and photocatalytic properties. Materials Science and Engineering: B 2012; 177:913–9.

[155] Khorasaninejad M, Chen WT, Zhu AY, Oh J, Devlin RC, Roques-Carmes C, et al. Visible wavelength planar metalenses based on titanium dioxide. IEEE Journal of Selected Topics in Quantum Electronics 2016; 23:43–58.

[156] Saha S, Victorious A, Soleymani L. Modulating the photoelectrochemical response of titanium dioxide (TiO_2) photoelectrodes using gold (Au) nanoparticles excited at different wavelengths. Electrochim Acta 2021; 380:138154.

[157] Rao KG, Ashok CH, Rao KV, Chakra CS, Rajendar V. Green synthesis of tio$_2$ nanoparticles using hibiscus flower extract. Proceedings of the International Conference on Emerging Technologies in Mechanical Sciences, 2014, p. 79–82.

[158] Khan MM, Ansari SA, Lee J, Cho MH. Enhanced optical, visible light catalytic and electrochemical properties of Au@ TiO_2 nanocomposites. Journal of Industrial and Engineering Chemistry 2013; 19:1845–50.

[159] Celebi N, Aydin MY, Soysal F, Ciftci YO, Salimi K. Ligand-free fabrication of Au/TiO_2 nanostructures for plasmonic hot-electron-driven photocatalysis: Photoelectrochemical water splitting and organic-dye degredation. J Alloys Compd 2021; 860:157908.

[160] de Moraes NP, Silva FN, da Silva MLCP, Campos TMB, Thim GP, Rodrigues LA. Methylene blue photodegradation employing hexagonal prism-shaped niobium oxide as heterogeneous catalyst: Effect of catalyst dosage, dye concentration, and radiation source. Mater Chem Phys 2018; 214:95–106.

[161] Amalraj A, Pius A. Photocatalytic degradation of monocrotophos and chlorpyrifos in aqueous solution using TiO_2 under UV radiation. Journal of Water Process Engineering 2015; 7:94–101.

[162] Zhao C, Zhou Y, de Ridder DJ, Zhai J, Wei Y, Deng H. Advantages of TiO_2/5A composite catalyst for photocatalytic degradation of antibiotic oxytetracycline in aqueous solution: comparison between TiO_2 and TiO_2/5A composite system. Chemical Engineering Journal 2014; 248:280–9.

[163] Rizzo L, Sannino D, Vaiano V, Sacco O, Scarpa A, Pietrogiacomi D. Effect of solar simulated N-doped TiO_2 photocatalysis on the inactivation and antibiotic resistance of an E. coli strain in biologically treated urban wastewater. Appl Catal B 2014; 144:369–78.

[164] Kimura K, Naya S, Jin-nouchi Y, Tada H. TiO_2 crystal form-dependence of the Au/TiO_2 plasmon photocatalyst's activity. The Journal of Physical Chemistry C 2012; 116:7111–7.

[165] Tanaka A, Sakaguchi S, Hashimoto K, Kominami H. Preparation of Au/TiO_2 with metal cocatalysts exhibiting strong surface plasmon resonance effective for photoinduced hydrogen formation under irradiation of visible light. ACS Catal 2013; 3:79–85.

[166] Kowalska E, Mahaney OOP, Abe R, Ohtani B. Visible-light-induced photocatalysis through surface plasmon excitation of gold on titania surfaces. Physical Chemistry Chemical Physics 2010; 12:2344–55.

[167] Li H, Wang S, Hong F, Gao Y, Zeng B, Haider RS, Fan F, Huang J, Li C. Effects of the interfacial defects in Au/TiO_2 on plasmon-induced water oxidation. J Chem Phys 2020;152.

[168] Pang Q, Zhong X, Yan W, Ma H, Ren H, Song L, Lv Z, Li L, Chen C, Wang H, Lin X, Zhang Q. Role of percentage of {0 0 1} crystal facets in

TiO$_2$ supports toward the water–gas shift reaction over Au-TiO$_2$ catalysts. Chemical Engineering Journal 2022; 446:137010.

[169] Murdoch M, Waterhouse GIN, Nadeem MA, Metson JB, Keane MA, Howe RF, et al. The effect of gold loading and particle size on photocatalytic hydrogen production from ethanol over Au/TiO$_2$ nanoparticles. Nat Chem 2011; 3:489–92.

[170] Zhu H, Ke X, Yang X, Sarina S, Liu H. Reduction of nitroaromatic compounds on supported gold nanoparticles by visible and ultraviolet light. Angewandte Chemie International Edition 2010; 49:9657–61.

[171] Dong S, Tebbutt GT, Millar R, Grobert N, Maciejewska BM. Hierarchical porosity design enables highly recyclable and efficient Au/TiO$_2$ composite fibers for photodegradation of organic pollutants. Mater Des 2023; 234:112318.

[172] Sangpour P, Hashemi F, Moshfegh AZ. Photoenhanced degradation of methylene blue on cosputtered M: TiO$_2$ (M= Au, Ag, Cu) nanocomposite systems: a comparative study. The Journal of Physical Chemistry C 2010; 114:13955–61.

[173] Jansanthea P, Chomkitichai W. Enhanced photocatalytic degradation of methylene blue by using Au-TiO$_2$. Applied Mechanics and Materials 2019; 886:107–13.

[174] Luna M, Gonzalez-Hidalgo A, Diaz A, Goma D, Gatica JM, Mosquera MJ. Strong Metal-Support Interaction (SMSI) in Au/TiO$_2$ photocatalysts for environmental remediation applications: Effectiveness enhancement and side effects. J Environ Chem Eng 2023; 11:109947.

[175] Aswathy PM, Sarina P, Kavitha MK, Priya MJ, John H, Jayaraj MK. Development of Au doped TiO$_2$ nanofibers for photocatalytic applications. AIP Conf Proc, vol. 2082, AIP Publishing; 2019.

[176] Isaac RSR, Ashima B, Praseetha PK. Sonophotocatalytic degradation of Methylene Blue using synthesized M@ TiO$_2$ Nanocomposites (M= Ag, Pd, Au, Pt) n.d.

[177] Arias M-C, Aguilar C, Piza M, Zarazua E, Anguebes F, Anguebes F, Cordova V. Removal of the Methylene Blue Dye (MB) with Catalysts of

Au-TiO$_2$: Kinetic and Degradation Pathway. Modern Research in Catalysis 2021; 10:1.

الخلاصة

في هذا العمل، تم تحضير ثنائي أوكسيد التيتانيوم (TiO_2) و Au/TiO_2 بنسب مختلفة (0.5، 1.0، 1.5، 2.0، و 2.5) بطريقة سول جل وتلدينه عند 450 درجة مئوية.

تم تحديد التركيب البلوري، ونسبة طور الروتيل والأناتاز، والحجم البلوري للجسيمات النانوية المركبة باستخدام تحليل حيود الاشعة السينية (XRD). تم استخدام تحليل مطيافية الالكترون الاشعة السينية (XPS) لتحديد التركيب العنصري والنسبة المئوية في العينات بدقة. تم التعرف على مورفولوجية العينات من خلال تحليل المجهر الاللكترون النافذ (TEM)والمجهر الالكترون الماسح بأنبعاث المجال (FESEM). أكد تحليل الاشعة السينية لطاقة المتشتتة (EDX) وجود جسيمات الذهب النانوية في العينات المطعمة وكشف عن النسبة المئوية لتكوين العناصر الأخرى. أظهر تحليل الخرائط توزيعًا موحدًا للجسيمات النانوية داخل جميع العينات. تم تقييم مساحة السطح والمسامية المحددة باستخدام تحليل المساحة السطحية المحددة (BET). من خلال الطرائق التحليلية للأشعة فوق البنفسجية وتحليل الاشعة تحت الحمراء (FTIR) قمنا بدراسة الامتصاص البصري في مناطق الأشعة فوق البنفسجية والأشعة تحت الحمراء، على التوالي.

تم تحديد الجرعة المثلى من المحفزات في عملية التحلل الضوئي. تم اختبار كميات مختلفة من محفزات TiO_2 (05، 10، 15، 20، و25 ملغرام)، باستخدام تركيز أولي قدره 10 جزء في المليون من الميثيل الازرق. تم تقييم كفاءة التحلل تحت إشعاع الضوء فوق البنفسجي، وفي النهاية تم اختيار 15 ملغرام كجرعة تحفيزية أكثر فعالية، مما أدى إلى كفاءة تحلل قدرها 68.62%. بعد ذلك، تم تقييم تحلل الميثيل الازرق لمختلف المحفزات، بما في ذلك Au/TiO_2 0.5%، و1% Au/TiO_2، و1.5% Au/TiO_2، و2% Au/TiO_2، و2.5% Au/TiO_2. في ظل ظروف مماثلة (التركيز الأولي لـ MB = 10 ppm ، جرعة المحفز = 15 ملغرام، 120 دقيقة من الأشعة فوق البنفسجية)، أظهر المحفز 2% Au/TiO_2 أعلى نسبة تحلل لـ MB، بقياس 79.88%.

جامعة كربلاء

كلية العلوم

قسم الفيزياء

تحضير وتوصيف ثنائي أوكسيد التيتانيوم المطعم بجسيمات الذهب النانوية كمحفزات ضوئية

رسالة مقدمة الى

مجلس كلية العلوم – جامعة كربلاء

وهي جزء من استكمال متطلبات نيل درجة الماجستير

علوم في الفيزياء

من قبل

رشا جميل نعمة

بكالوريوس علوم فيزياء (2009)/ جامعة كربلاء

إشراف

أ. د. خولة جميل طاهر   **أ. د. فراس كامل محمد العصفور**

رمضان/ 1445 ه   **نيسان/ 2024 م**